Matériaux pour la Géologie de la Suisse

GEOPHYSIQUE
Nr. 31

Publiés par la commission Suisse de Géophysique
Organe de la Société Helvétique des Sciences Naturelles,
subventionnée par la confédération

THE AIRBORNE GRAVIMETRIC SURVEY OF SWITZERLAND

E. E. Klingelé
M. Cocard
M. Halliday
H.-G. Kahle

GEODESY AND GEODYNAMICS LAB

1996

Adresse des auteurs:

E. E. Klingelé, M. Cocard, H.-G. Kahle

Geodesy and Geodynamics Laboratory
Institute of Geodesy and Photogrammetry
ETH-Hönggerberg
CH-8093 Zürich
Switzerland

M. Halliday

LaCoste and Romberg Gravimeters Inc.
4807 Spicewood Springs Road
Austin 78759 Texas
USA

Editor's Preface

The present publication entitled "The Airborne Gravimetric Survey of Switzerland " is Report Nr. 31 of the "Contribution to the Geology of Switzerland - Geophysical Series", published by the Swiss Geophysical Commission.
It contains a complete description of the procedures used by the authors to develop a reliable airborne gravimetric survey system. The combination of the accelerations measured with a gravimeter in dynamic mode, and the accelerations derived from precise GPS coordinates of the aircraft, allows non-gravitational accelerations to be separated from gravity signal. The Swiss Geophysical Commission is very grateful to the authors for having realized this pioneering work.
Special thanks are due to the Swiss National Academy of Natural Sciences for its financial support of this publication.

Zurich, November 1996

In the name of the
Swiss Geophysical Commission
The President :

Prof. Emile Klingelé

PREFACE

The majority of GPS geodetic work has been done in the static mode although the satellite based navigation system was designed primarily for kinematic purposes. During the past few years differential GPS and the use of carrier phase measurements have enabled GPS to become established as a precise positioning system, also for airborne applications. As the GPS constellation has nearly reached completion, it has become an important component in the improvement of airborne gravimetry.

The combination of the accelerations measured with the gravimeter, and the accelerations derived from the precise GPS coordinates of the position vector of the aircraft, allows non-gravitational aircraft accelerations to be separated from gravity signals caused by mass inhomogeneities in the earth's interior, including topographic effects. The report presented here focuses on this problem by using airborne data acquired during an extensive airborne gravimetry flight campaign in Switzerland.

We are grateful to Dr. L. Bagnasci, now at Silicon Graphics, Zurich, and Dr. B. Martinelli, now at Observatorio Seismologico e Volcanologico, Pasto, Columbia, for introducing the extended Kalman filtering technique in the data processing. Dr. Ing. M. Cocard, Geodynamics Lab (GGL)/ETHZ, carried out the GPS analysis, based on software which he developed at our institute. Dipl. Ing. U. Theurer, Ingenieurgesellschaft für Geophysikalische Messtechnik, Ueberlingen, Germany, provided help in hardware matters and technological problems. We are particularly indebted to Dr. Ing. A. Geiger, GGL/ETHZ, for his participation and advice in all stages of the project. Mr. M. Halliday, Chief Scientist of LaCoste & Romberg Gravity Meters, Inc., provided the necessary instrumentation and participated in all of the flights. His knowledge and ability to solve practical problems during the night-flights were of great value. The gravimeter system and GPS receiver were also operated by Dr. Ing. F. Arnet and Dipl. Natw. ETH Th. Wyss.

The uncomplicated support of the "Bundesamt für Militärflugplätze" (BAMF), the "Bundesamt für Zivilluftfahrt" (BAZL) and of the "Eidgenössische Vermessungsdirektion (VD) were essential for the realization of this project. We are especially grateful to Mr. R. Hübscher, Mr. M. Baumberger , Mr. M. Escher, Mr. G. Gugger and Mr. M. Jost, who helped us before, during and after the flights. The Civil Air Traffic Control of the Federal Office of Aviation kindly gave us permission to take off and land during the night. Mr. D. Mosimann offered helpful suggestions and arranged for official permissions. Mr. K. Korodi organized the entire infrastructure for the aircraft at the airport of Kloten, Zurich, which is gratefully acknowledged.

We wish to express our special thanks to Prof. Dr. R. Hütter, Vice President of Research Affairs at the ETH Zürich, for his continued encouragement and support in all organizational and funding matters. This research project was funded by the ETH grant 0-20-532-91.

Mrs. C. Hasler helped in editing the English version. Dr. I. Hadley, University of Geneva, critically reviewed the manuscript and offered helpful suggestions for its improvement.

The documentation forms part of the IGP study groups No. 5.36 (Precise navigation with GPS) and No. 5.23 (Gravity, gradiometry and aerogravimetry).

Prof. E. E. Klingelé and Prof. H.-G. Kahle

August 1996

GGL-IGP- ETHZ

CONTENT

SUMMARY

The Geodynamics and Geodesy Laboratory (GGL) of the Institute of Geodesy and Photogrammetry (IGP) of the ETH Zurich has acquired airborne gravity data in a joint project with LaCoste and Romberg Gravity Meters, Inc.. The survey covering the whole of Switzerland was carried out using a Twin-Otter aircraft owned by the Swiss Federal Directorate of Cadastral Surveying. The aircraft was equipped with three GPS receivers, one for navigational purposes and the other two for positioning and for monitoring the aircraft accelerations. Four receivers were also installed on the ground as reference stations. A modified LaCoste and Romberg marine gravimeter recorded data at a sampling rate of one measurement per second. Modifications included anti-alias filters and an absolute encoder for the measuring screw. Flights were performed during November and December 1992 at barometric altitude of 5100 m above sea-level. An airborne Bouguer anomaly map, computed at the flight altitude with topographic corrections of up to 167 km with a density of 2670 kg/m^3, is presented and qualitatively compared with the existing ground Bouguer anomaly map. Computation of the Bouguer anomaly values at crossing points between lines flown at comparable altitudes shows differences varying from 1.1 mgal to 11.3 mgal (10^{-5} ms^{-2}). The differences between upward continued ground data (extracted from EGT data and the Bouguer gravity map of Switzerland) and the airborne Bouguer anomaly calculated from 61438 data points give a **mean value of 0.6 mgal with a standard deviation of 11.9 mgal.**

1 Introduction

Knowledge of the earth's gravity field is of great importance for both geodesy and geophysics. Typical applications are the determination of the geoid, the reduction of leveling data for the determination of orthometric heights, the determination of the density distribution inside the earth, and the detection of secular gravity changes coupled with geodynamic processes. In geodesy, the measurements are linked to geopotential surfaces and gravity lines. Measurements carried out on the surface of the earth are strongly perturbed by the effects of local inhomogeneities and have to be corrected accordingly. In spite of sophisticated interpolation and regularization methods, the errors introduced by local effects are not completely eliminated and affect the results of calculations.

In geophysics the gravity method is important for the study of the earth's interior. This method provides information complementary to seismic data, and enables a quasi continuous determination of the density distribution with depth.

In the classical terrestrial gravity method the costs and time necessary for measurements are extremely high. Because the measurements are not made on a horizontal surface, they are strongly influenced by local density anomalies and time-consuming algorithms have to be applied to the data reduction.

For geodesy as well as for geophysics, the ideal solution would be to make all measurements on a horizontal surface located above the topography. The interpretation can be performed directly on the measurement surface and all the potential field transformation methods, based on the Fourier transformation, can be applied without restriction.

In order to obtain data smoothly on a large scale one is tempted to determine gravity fields from space. By means of the measurement of satellite orbit perturbations it has become possible to determine the long wavelength components ($\lambda > 1000$ km) of the gravity field with sufficient accuracy. Unfortunately, however, these wavelengths are not suitable for the determination of the geoid on a local or regional scale, as would be necessary for the Alpine region. Recently, the European Space Agency (ESA) proposed a geodetically dedicated mission, called ARISTOTELES in which a satellite with a two-component gravity gradiometer would allow the determination of the earth's gravity field in the wavelength range between 100 and 1000 km.

Apart from the fact that for financial reasons this mission will not be pursued in the future, the expected results would suffer from the disadvantage that the minimum wavelength of the gravity field is too large. From such data Switzerland would be covered, in the most optimistic case, by only twenty values.

In order to fill the gap between the very short wavelength information ($\lambda < 10$ km) obtained from ground measurements and the actual (and possibly available in the future) long wavelength information ($\lambda > 1000$ km) the GGL of the ETH Zurich decided in 1990 to develop a strategy for performing airborne gravity surveys in Switzerland.

Up till this time, only a few experiments had been carried out in the field of airborne gravimetric measurements for geodetic and large-scale geophysical purposes, in particular, because of the problem of determining the position of the aircraft with very high accuracy. An accuracy in the mm range is necessary for the computation and the removal of the disturbing (non-gravitational) accelerations. Systems for measuring gravity in dynamic mode were

mostly used in marine applications with low-dynamic behavior and in few cases for airborne gravimetric tests (LaCoste, 1967; Bell et al., 1991; Brozena and Peters, 1984; LaCoste et al., 1982; Brozena et al., 1989; Bell et al., 1994; Valliant, 1991).

Discussions in 1991 led to the conclusion that this project would be a good opportunity for LaCoste and Romberg Gravity Meters Inc. (Austin, Texas) to modify and improve their Model S Marine gravimeter, in order to make it a working and commercial airborne system. The ETH and LaCoste and Romberg therefore decided to join forces to realize this project. At the same time the V+D (Swiss Federal Directorate of Cadastral Surveying) expressed an interest in participating in this project by placing its aircraft, together with pilots and navigators at free disposition of the survey.

2 The Aircraft

The survey was performed with a DeHavilland Twin Otter aircraft owned by the (V+D) Ministry of Justice, and operated by pilots of the "Bundesamt für Militärflugplätze". The aircraft is equipped with an automatic pilot, Collins type AP 106 and with a GPS/LORAN receiver Trimble 2000 for navigation purposes. (Figure 2.1)

The characteristics and performance of the aircraft are :

Engines	Two turbo-prop. GE/PT GA of 652 HP
Length	5.77 m
Wingspan	19.81 m
Height	5.67 m
Empty Weight	3350 kg
Max. load	2350 kg
Max. speed	335 km/h
Max. ascending speed	8 m/s
Full load max. altitude	8140 m
Take-off distance	366 m
Landing distance	320 m
Max. fuel load	1112 kg
Autonomy	5 hours

Figure 2.1: The DeHavilland Twin-Otter HB-LID of the (V+D) "Ministry of Justice".

3 The gravimeter and the stabilized platform

The LaCoste and Romberg Model S Marine gravity meter consists of a heavily damped zero length spring gravity meter element, mounted in a gyro-stabilized platform. Two horizontal accelerometers on the platform are used to keep the platform in a vertical position. Details of the marine gravity meter and stabilized platform have been described previously by LaCoste (1967); LaCoste et al. (1982); Bell et al. (1991); Brozena and Peters (1988); Brozena (1984).

In order to produce a prototype Model SA airborne gravity meter, the following requirements were considered:

- Due to the Eötvös effect influencing the moving aircraft platform, it is necessary to change the spring tension many hundreds or thousands of mgals when turning the aircraft at the end of the east-west oriented flight lines. An airborne gravity system therefore should be able to change the spring tension at rates of perhaps 1000 counter units per minute.

- In order to recover gravity information of the shortest possible wavelength, the considerable speed of the aircraft, requires that the data acquisition rate must be one second or shorter, instead of the normal 10 second rate used for marine surveys. As the data should be filtered as little as possible, care must be taken to remove noise in the system, in this higher frequency range.

- The airborne system should be as compact and low powered as possible, to fit it to a small aircraft. A graphical presentation of system outputs is desirable, to help the operator monitor the data in real time and make suggestions to the flight crew during the flight.

In order to fulfill these requirements the following modifications were carried out :

- The existing stepper motor was substituted by a servo motor to allow rapid adjustment of the spring tension.

- A 24-bit absolute shaft encoder (4096 turns by 4096 bits per turn) was attached to the spring tension counter, to ensure that correct information was recorded despite the high slewing rates.

- The standard marine gravity software was only used to control the stabilized platform and to compute and record cross coupling values. The platform period was set to 4 minutes.

- A LabView software control system was used to adjust the Spring Tension and record the absolute encoder.

- A signal conditioning module with 3 Hz anti-alias filters was added to prevent aliasing upon digitalization. The beam position and horizontal accelerometer signals were digitized at 10 Hz and then averaged to one second samples before recording on the computer hard disk.

- The three on-off heating circuits in the marine gravity meter (for the gravity meter heater and two gyros) were replaced by proportional heater systems which operate at a higher frequency. This eliminated transient voltages with a period of 10 to 20 seconds in the beam position signal.

- An attitude gyroscope was mounted on the stabilized platform frame for measuring pitch and roll of the aircraft.

- Three extra channels of analogue input were provided to digitalize and record these two signals, as well as barometric altitude.

- A timing signal was generated each minute and the event was recorded by one GPS receiver for synchronization between the gravity and positioning systems.

Figure 3.1 shows the system used for this survey and figure 3.2 an example of the information displayed by the system during the measurements.

Figure 3.1: View of the platform and gravimeter installed in the aircraft for the airborne survey of Switzerland.

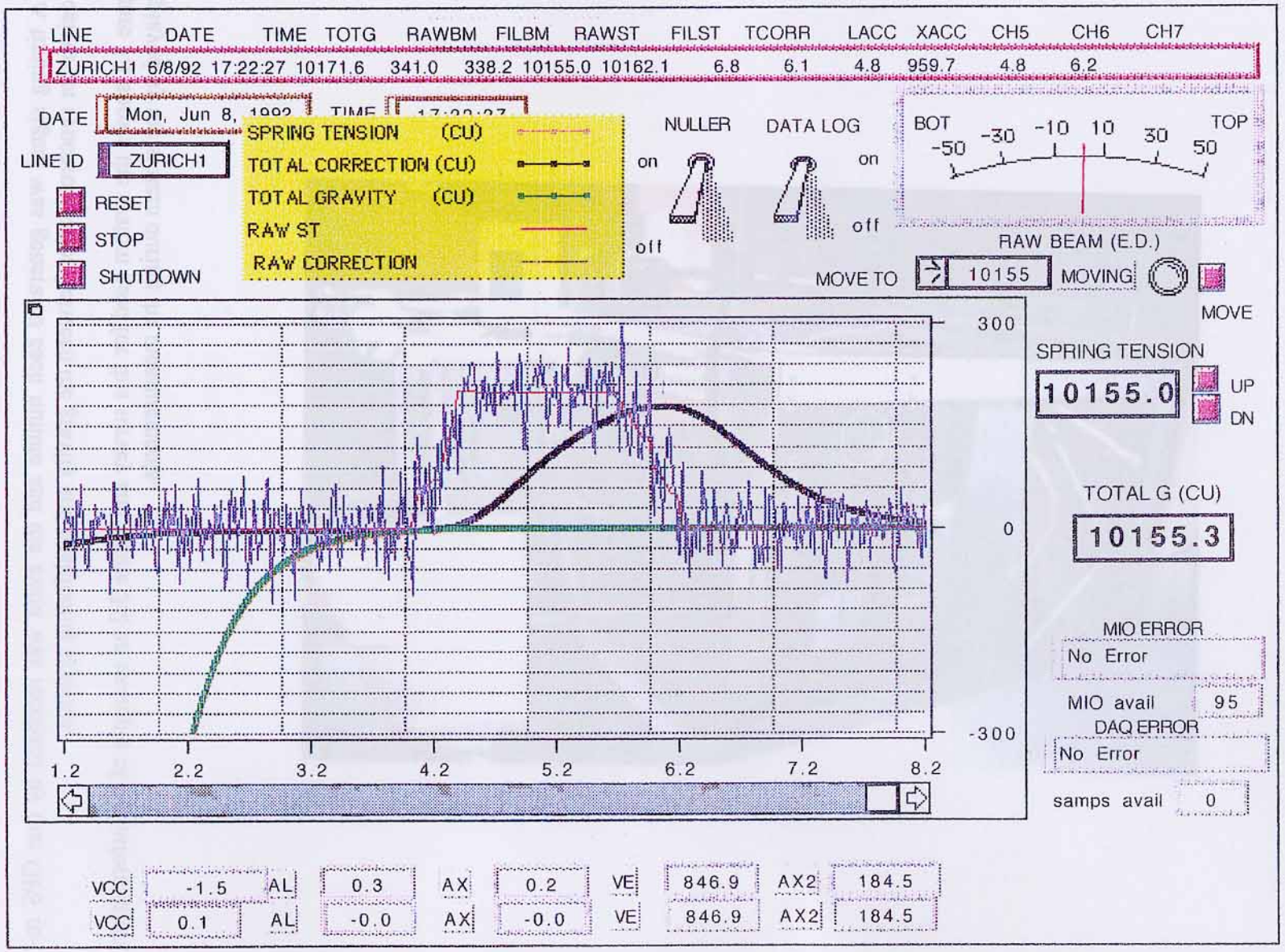

Figure 3.2 : Example of the information given by the display of the system.

4 The GPS receivers

4.1 Overview of the GPS related part of the project

6 GPS-receivers (TRIMBLE SST) were used for all the flights. 4 of these were located at different stations on the ground (see Figure 4.1). 2 receivers were on board of the aircraft which leads to the following configuration:

Stations	Rec. ID.	freq.	Owner
Zimmerwald	1934	dual	Swiss Federal Office of Topography (L+T)
Zurich	1355	dual	Swiss Federal Institute of Technology (ETHZ)
Lausanne	2105	dual	University of Braunschweig (Germany)
Engadin	1975	dual	University of Braunschweig (Germany)
Aircraft	1354	dual	Swiss Federal Institute of Technology (ETHZ)
	1567	single	Swiss Federal Institute of Technology (ETHZ)

Table 4.1: Overview of the GPS equipment used.

All receivers used were dual frequency receivers with the exception of one of the two receivers on board the aircraft. Table 4.2 summarizes the main characteristics of the GPS data sets.

GPS receivers :	6 Trimble SST
Measurements collected :	
by all the receivers:	
- C/A-code on L1	
- L1-phase	
additionally, only on the dual frequency receivers :	
with selective availability (S/A) OFF	with selective availability (S/A) ON
- P-code on L2	- No P-code
- L2-phase	- L2-phase squared
(S/A was active on 2 of the 8 measuring days.)	
Measurement rate :	2 Hz
(Data downloaded directly to the portable computer hard disk)	

Table 4.2: Parameters related to the GPS part.

The measurements were collected at a measuring frequency of 2 Hz (1 block of measurements every 0.5 sec). The duration of a flight was about 5 hours. Since the capacity of the internal

memory of the receivers was too small, the data was transferred directly to portable computers, using the commercial Trimble software. The whole data set was transferred to a mainframe computer later on and the binary data format converted to a receiver independent ASCII-format (RINEX = Receiver INdependent EXchange Format).

4.2 Reference network

Before processing the kinematic GPS data from the aircraft, all ground stations were first connected to Zimmerwald by means of static baselines. This task was performed using Bernese Software Version 3.4 (Rothacher et al. 1993) which is well suited for the processing of static GPS data and is commonly used at our institute for the processing of large geodynamic GPS campaigns (Mueller 1995, Straub 1994). The computation is based on a least square adjustment, using double difference phase measurements as basic observations.

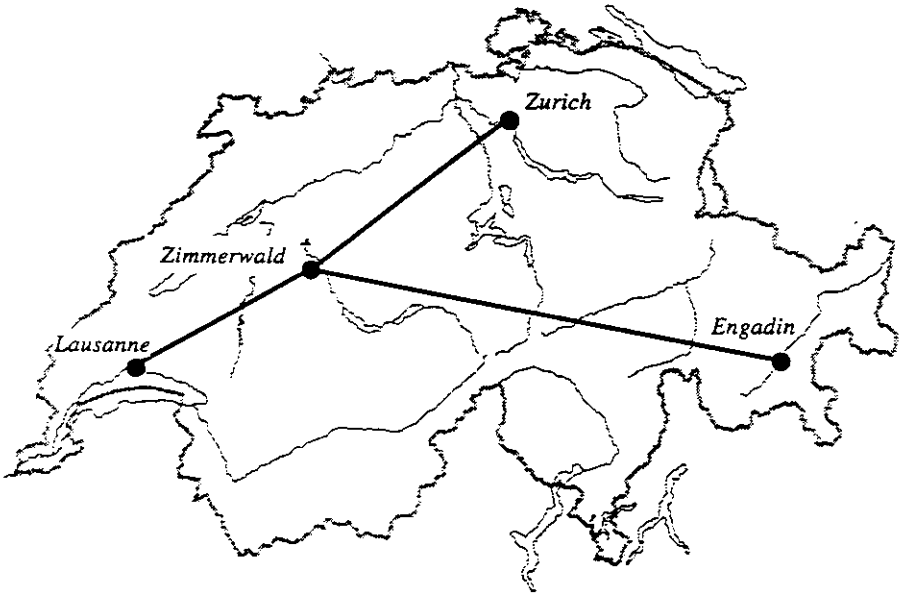

Figure 4.1: Connection of all reference stations to the Master station Zimmerwald

For this computation the high frequency data sets were reduced to 30 sec data sets. For every day and every station a separate solution was calculated. The measuring time was of the order of 5 hours per day and all stations were directly connected to the master station Zimmerwald, being an IGS-site. The ionosphere free combination of the basic L1- and L2-phase measurements was used without ambiguity fixing (floating point L3 solution). The results are given in Table 4.3.

Zimmerwald	**fixed**	**4331297.2880**	**567555.3830**	**4633133.9390**
Zurich	day 328	4277250.5282	640022.7757	4672956.6170
Zurich	day 329	4277250.5326	640022.8025	4672956.6227
Zurich	day 334	4277250.5390	640022.7699	4672956.6375
Zurich	day 335	4277250.5268	640022.8153	4672956.6354
Zurich	day 341	4277250.4862	640022.8248	4672956.6020
Zurich	day 344	4277250.5153	640022.7862	4672956.5852
Zurich	day 345	4277250.5553	640022.7939	4672956.6312
Zurich	**mean**	**4277250.526**	**640022.795**	**4672956.617**
	rms	**0.022**	**0.020**	**0.018**
Engadin	day 328			
Engadin	day 329	4331774.5972	754351.8661	4607266.3798
Engadin	day 334	4331774.5669	754351.8610	4607266.3650
Engadin	day 335	4331774.5975	754351.8807	4607266.3812
Engadin	day 341	4331774.5178	754351.8835	4607266.3288
Engadin	day 344	4331774.5676	754351.9018	4607266.3472
Engadin	day 345	4331774.6048	754351.8410	4607266.3278
Engadin	**mean**	**4331774.575**	**754351.872**	**4607266.355**
	rms	**0.032**	**0.021**	**0.024**
Lausanne	day 328	4367945.5140	502877.6538	4605616.4650
Lausanne	day 329	4367945.5279	502877.6467	4605616.4758
Lausanne	day 334	4367945.5244	502877.6558	4605616.4632
Lausanne	day 335	4367945.5372	502877.6391	4605616.4802
Lausanne	day 341	4367945.5049	502877.6525	4605616.4541
Lausanne	day 344	4367945.4922	502877.6395	4605616.4325
Lausanne	day 345	4367945.4950	502877.6533	4605616.4478
Lausanne	**mean**	**4367945.514**	**502877.649**	**4605616.460**
	rms	**0.017**	**0.007**	**0.016**

Table 4.3: Daily results and mean values of the reference network given in geocentric coordinates.

The geocentric Cartesian coordinates of Zimmerwald which were held fixed originate from a GPS campaign of the Swiss Federal Office of Topography and are designated by L+T 88. Nowadays (1996) they are not the best available set but differ from the best set (ITRF-93) by less than 30 cm.

The corresponding rms of the mean values deduced from all daily solutions, is about 2 cm. In the following computation of the kinematic data, these mean values for the coordinates of the reference stations were used.

5 Operations

5.1 First Test

One week of test flights for the prototype airborne gravity system was scheduled for May 1992. LaCoste and Romberg Gravity Meters mobilized meter S-114 to Zurich, Switzerland after making the previously described modifications

After the preliminary test flights, plans were finalized to survey all of Switzerland, starting in November 1992. The planned lines are shown in figure 5.1. The chosen flight and measurement parameters were :

Distance between W-E lines	12	km
Flight altitude	5200	m
Flight azimuth	76	degree
Aircraft speed	240	km/h
GPS sampling rate	0.5	sec
Gravimeter sampling rate	1	sec
Cross-coupling sampling rate	10	sec.

The line spacing was chosen taking into account the number of available flight hours and the best possible coverage. In order to minimize the number of turns at the end of the lines, their orientation was chosen so that they fit the longest distances of the country. In addition only four cross lines were planned because of the limited number of flight hours available.

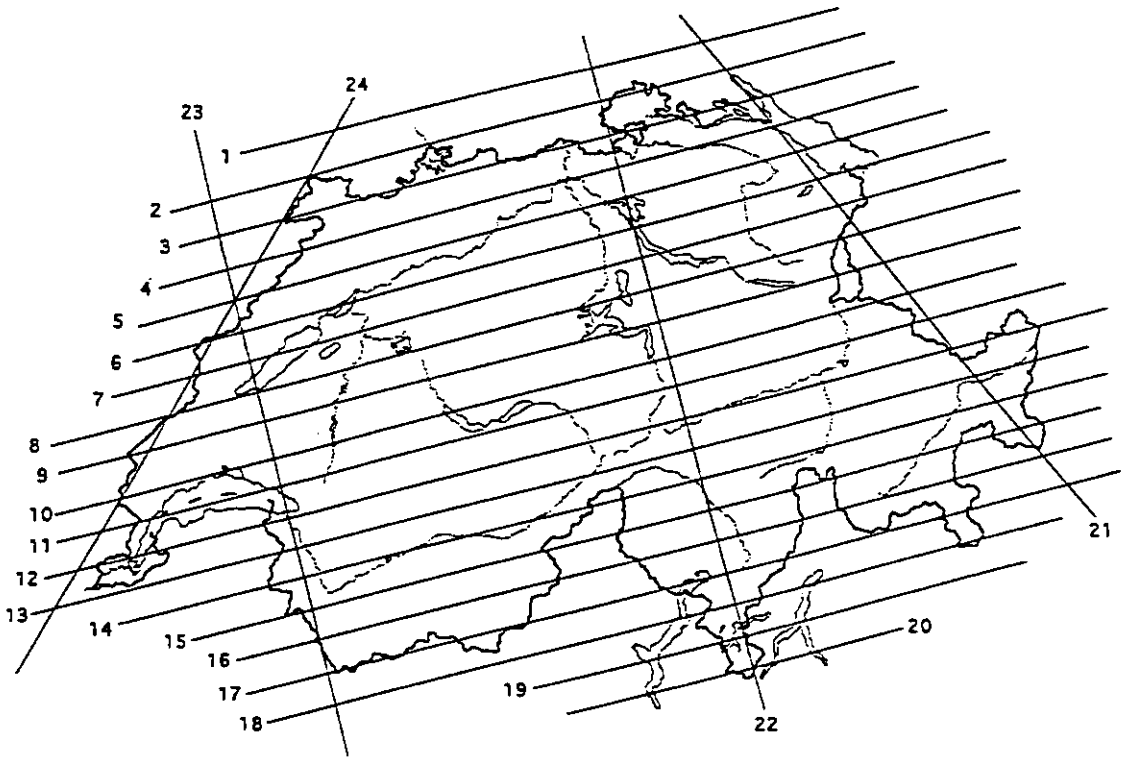

Figure 5.1: Planned flight lines with their number

Additional modifications were also made to the measurement system:

- The 2-rack prototype was reduced to a single-rack system to save space and power requirements in the aircraft. This was done by installing a new compact 200 Hz gyro power supply, redesigning the motor amplifiers, and removing the printer. An electroluminescent panel display was installed to provide the operator with real time graphical display of spring tension, gravity, beam position, and accelerometer outputs, to help judge the data quality while in flight.

- Significant amounts of noise (at 60 Hz and 200 Hz and their harmonics) were observed in the beam signal input to the A/D converter. A signal conditioning module with 3-Hz low-pass filters was placed in line with the beam position output and both horizontal accelerometers, in order to prevent aliasing upon digitalization.

5.2 Production survey

Eight night flights were flown between November 24 and December 11, 1992, at a barometric altitude of 5200 m. A total of 24 lines of data were acquired, including 4 cross-lines. Flight operations were generally limited to the period between midnight and 5 am on weekdays due to a combination of air traffic restrictions, GPS satellite geometry and selective availability.

A table of expected gravity values was computed for a grid of points covering the survey area, with heading and aircraft speed as variables. The operator adjusted the spring tension to the expected value for the starting point on the next line. Once the aircraft was on line and level for about five minutes, the operator unclamped the meter and began recording.

After each line, the operator would clamp the beam and then the pilot would begin the turn. The lines flown on every day are shown in figure 5.3 and the aircraft tracks for all days are plotted in figure 5.2.

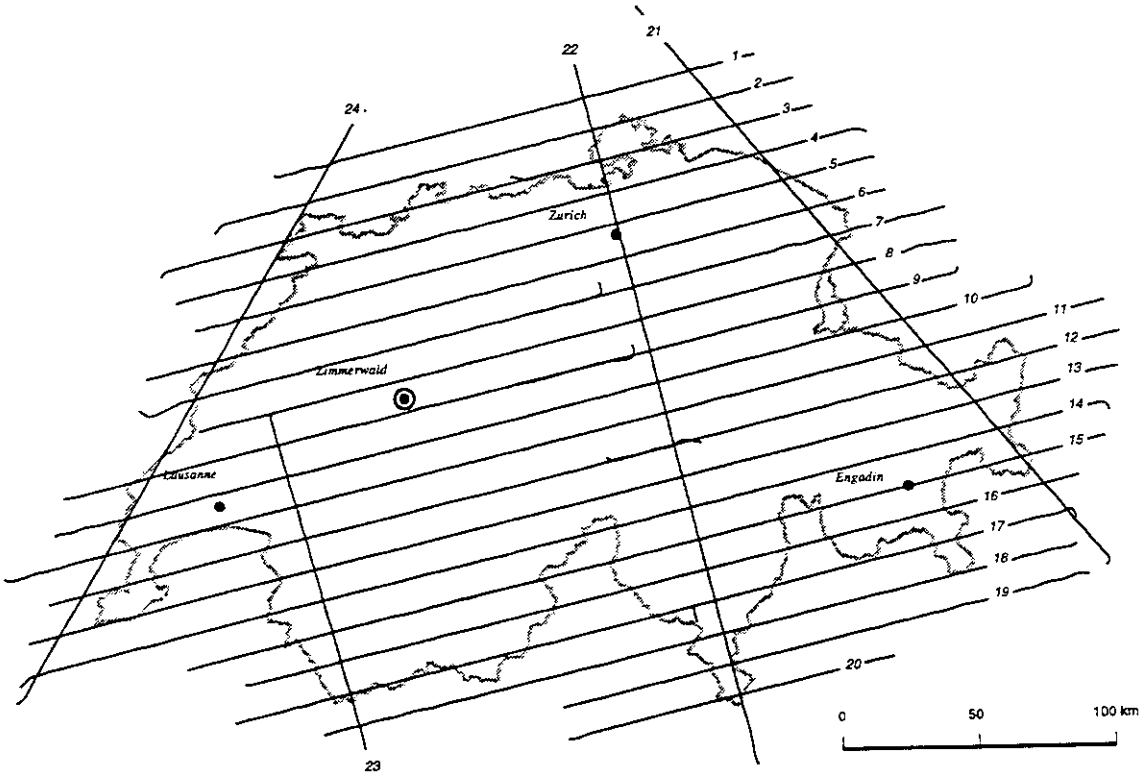

Figure 5.2: GPS tracks for all days

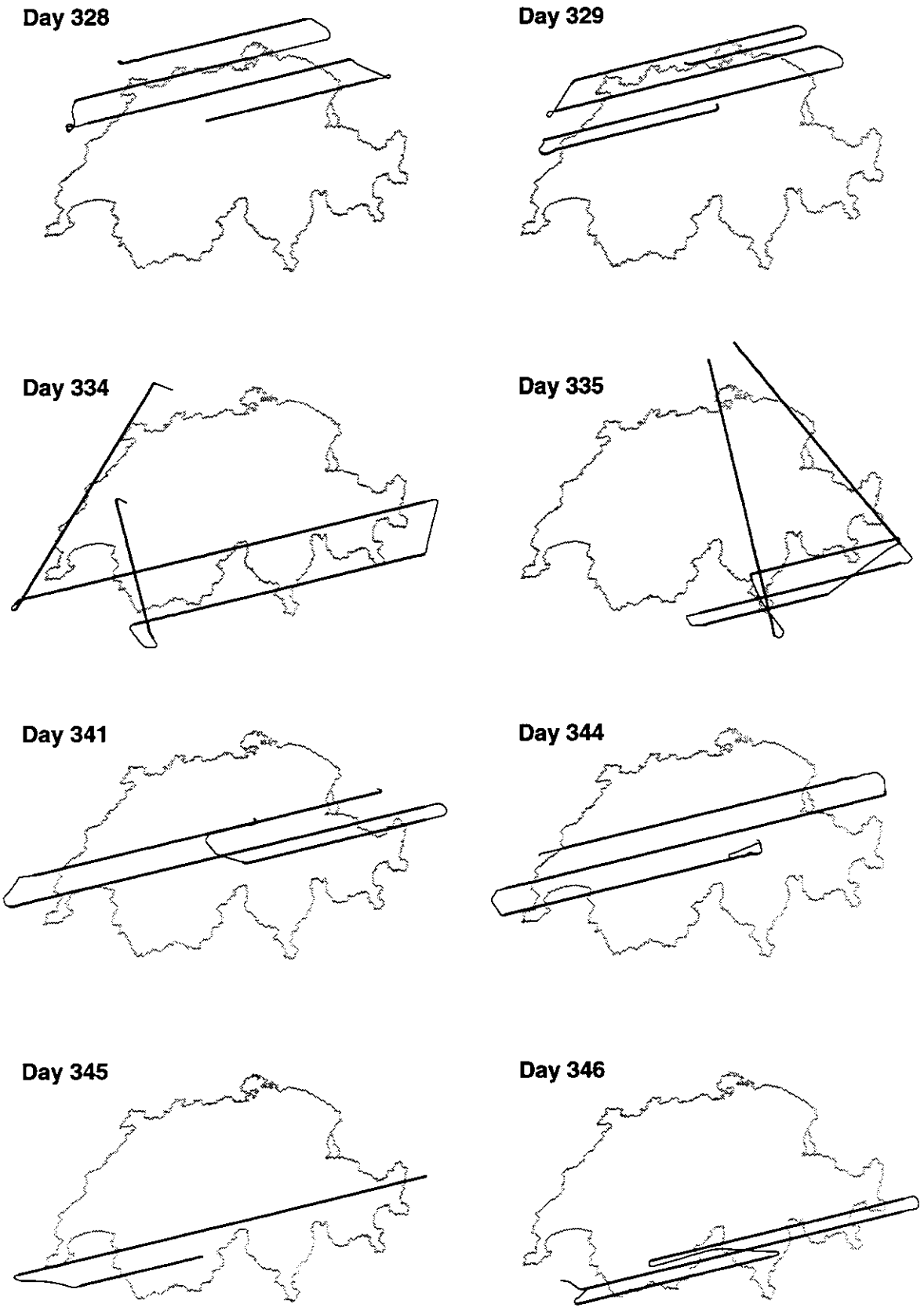

Figure 5.3: Flight path deduced from GPS for each day shown separately

6 Overview of coordinates and gravity systems

Gravity is the resultant of the gravitational and centrifugal forces acting on a body. In airborne gravimetry, the gravity field is measured from an aircraft, and therefore the measurements are influenced by other forces due to the motion of the gravimeter. In this study the computation of the full Bouguer gravity anomalies is presented. This involves the presentation of reference systems used for the description of all the forces on the meter and of the formula for the computation of normal gravity. For a survey of the different coordinates and gravity systems see Heiskanen and Moritz (1987) and Hehl (1992).

6.1 The Coordinate Systems

Different reference frames are used for the description of the motion on the earth's surface. In Figure 6.1, three different systems are depicted. The Cartesian coordinates system $({}_IX, {}_IY, {}_IZ)$ is an inertial system with its origin in the neighborhood of the earth's orbit. $({}_ix, {}_iy, {}_iz)$ is a quasi-inertial Cartesian system which moves with the earth around the sun by keeping all three axes parallel to those of the inertial system. The z-axis is parallel to the earth's rotation axis and the origin is the earth's center of gravity. The last coordinate system $({}_ex, {}_ey, {}_ez)$ rotates with the earth with angular velocity ω. The z-axis is parallel to the direction of the earth's rotation, the x-axis is the intersection of the Greenwich meridian plane with the equatorial plane, and the y-axis completes a right-handed earth-fixed orthogonal coordinate system.

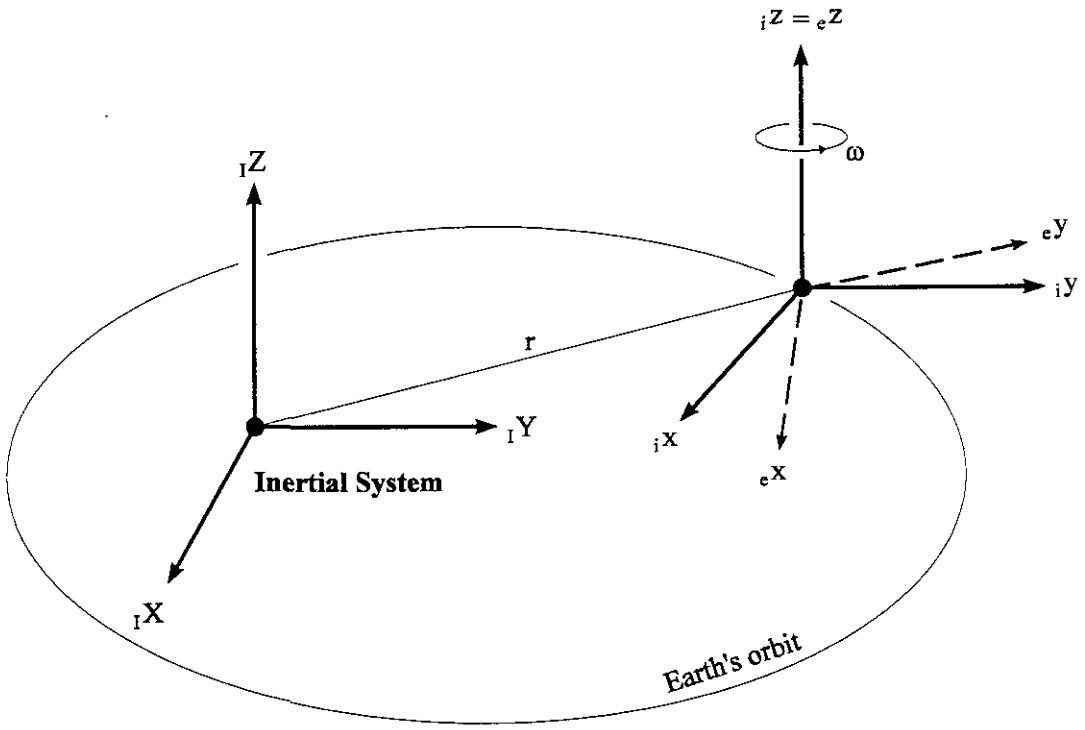

Figure 6.1: Accelerations at the gravimeter system

6.2 Acceleration at the gravity meter

Newton's law relates all the forces acting on a body to its acceleration in the inertial system *(I)*

$$m_I \ddot{X} = \sum_{j=1}^{n} {}_I F_j$$

In this analysis tidal forces are ignored because their order of magnitude is very small (ca. 0.2 mgal).

This leads to:

$$m_I \ddot{X} = {}_I F_{earth} + {}_I F_{other}$$

where the forces denoted by *earth* are forces due to the gravity field of the earth on the meter, and the forces denoted by *other* represent all the remaining forces acting on the meter. In the quasi inertial system *(i)* we have:

$$m_i \ddot{x} = {}_i F_{earth} + {}_i F_{other}$$

and the relation between *(I)* and *(i)* is:

$${}_I X = {}_i x + r$$

The measurements are carried out in the system *(e)* which rotates with the earth. The resulting accelerations are:

$${}_e a_{grav.meter} = {}_e a + 2\omega \wedge {}_e v + \ddot{r} - {}_e g$$

where ${}_e a_{grav.meter}$ is the acceleration measured by the gravimeter, ${}_e a$ is the acceleration of the gravimeter in the system *(e)*, $2\omega \wedge {}_e v$ is the Coriolis acceleration, $\ddot{r}$ is the acceleration due to the rotation of the earth around the sun (which is neglected in the calculations) and ${}_e g$ is the gravity that is of interest here.

6.3 The normal gravity

The formula for the normal gravity on the ellipsoid is given by the formula of Somigliana (1929):

$$g = \frac{a\gamma_a \cos^2\Phi + b\gamma_b \sin^2\Phi}{\sqrt{a^2 \cos^2\Phi + b^2 \sin^2\Phi}} = \frac{\gamma_a (1 + k \sin^2\Phi)}{\sqrt{1 - e^2 \sin^2\Phi}}$$

γ_a, γ_b are the theoretical values of gravity at the equator and at the poles, respectively. *a, b* are the semi-major and semi-minor axes respectively, *e* is the first eccentricity, *k* is the theoretical gravity formula constant and Φ is the geographical latitude.

The normal gravity above the ellipsoid is computed here by a second order approximation:

$$\gamma_h = \gamma - \frac{2\gamma_a}{a}\left[1 + f + m + (\tfrac{5}{2}m - 3f)\sin^2\Phi\right]h + \frac{3\gamma_a}{a^2}h^2$$

where f is the ellipticity and $m = \dfrac{\omega^2 a^2 b}{GM}$

where GM is the earth's gravitational constant (mass of earth's atmosphere included). A detailed presentation of these formulas is found in Heiskanen and Moritz (1987). In this work, all the constants used refer to the World Geodetic System 1984 (WGS84) see DMA Technical Report 8350.2.

Free-air anomalies are computed by subtracting the normal gravity at the measurement altitude from ${}_e g$:

$$FA = {}_e g - \gamma_h$$

7 GPS data processing

7.1 General Approach

Two different types of observation are carried out by GPS receivers: phase measurements, which correspond to the difference between the carrier signal generated by the internal oscillator of the receiver, the carrier signal coming in from the satellite and code measurements. The code measurements (pseudo-range measurements) are obtained by correlation technique using known pseudo-random sequences which are modulated on the carrier wave. Basically, both types of observations can be thought of as range measurements corrupted by some biases.

For all high precision applications, in the static as well as in the kinematic mode, only a differential approach involving two receivers may be applied.

7.1.1 Single-difference observations

The so called 'single difference' measurements are obtained by forming the difference between two simultaneous observations from two different receivers (ground station and airplane) to the same satellite. This differentiation technique may be applied to code as well as to phase measurements. The simultaneity is in fact defined by the readings of the two receivers. This means that the true GPS times of the two zero difference measurements are not equal, due to the different receiver clock biases. Even in the absence of any receiver clock error, transmission times would slightly vary because the distances to the satellites are different. In the following equations the indices (f) will be used for the fixed station, (m) for the moving receiver and (s) for the satellite.

The observation equation for the single difference code measurements are:

$$\Delta\rho^{s}_{mf}(t_{Nom}) = \rho^{s}_{m}(t_{Nom\ m}) - \rho^{s}_{f}(t_{Nom\ f})$$

and for single difference phase measurement :

$$\Delta\varphi^{s}_{mf}(t_{Nom}) = \varphi^{s}_{m}(t_{Nom\ m}) - \varphi^{s}_{f}(t_{Nom\ f})$$

They may be formally expressed as :

$$\textit{code:} \qquad \Delta\rho^{s}_{mf} = \Delta d^{s}_{mf} + \Delta clBias_{mf} - \Delta clBias^{s}_{mf} + \Delta Ion^{s}_{mf} + \Delta Trp^{s}_{mf}$$

$$\textit{phase:} \qquad \Delta\varphi^{s}_{mf} = \Delta d^{s}_{mf} + \Delta clBias_{mf} - \Delta clBias^{s}_{mf} - \lambda\cdot\Delta A^{s}_{mf} - \Delta Ion^{s}_{mf} + \Delta Trp^{s}_{mf}$$

with:

$$\Delta d^{s}_{mf} = \left|\vec{X}^{s}(t_{Tm}) - \vec{x}_{m}(t_{Rm})\right| - \left|\vec{X}^{s}(t_{Tf}) - \vec{x}_{f}(t_{Rf})\right|$$

$$\Delta clBias_{mf} = clBias_{m}(t_{Rm}) - clBias_{f}(t_{Rf}) = c\cdot(cl_{m}(t_{Rm}) - cl_{f}(t_{Rf}))$$

$$\begin{aligned}\Delta clBias^s_{mf} &= clBias^s_m(t_{Rm}) - clBias^s_f(t_{Rf}) \\ &= c\cdot(cl^s_m(t_{Rm}) - cl^s_f(t_{Rf})) \\ &\approx c\cdot(\tfrac{d}{dt}cl^s\cdot(t_{Rm}-t_{Rf})) \qquad \approx 0\end{aligned}$$

From the point of view of system performance, this term may be neglected, since typical values for $\frac{d}{dt}cl^s$ are in the order of 10^{-10} or better. A differential synchronization error $(t_{Rm} - t_{Rf})$ of 1 second would provoke an error of 3 mm in $\Delta clBias^s_{mf}$. This assumption, however, is no longer correct under Selective Availability (SA) where an artificial degradation of the satellite clocks is introduced.

$\Delta Ion^s_{mf} = Ion^s_m - Ion^s_f$ differential ionospheric delay.

$\Delta Trp^s_{mf} = Trp^s_m - Trp^s_f$ differential tropospheric delay.

ΔA^s_{mf} single-difference ambiguity of the phase measurements.

If we assume that the positions $\vec{X}^s$ of the satellites are calculated using broadcast or precise ephemerides and that the coordinates of the reference station $\vec{x}_f$ are known, the unknown parameters to be determined are :

- *the geocentric coordinates of the roving receiver* x_j, y_j, z_j
- *the differential clock bias of the roving receiver* $\Delta clBias_{mf}$
- *the 'single-difference' ambiguities of the carrier-phase* ΔA^s_{mf}

The coefficients of the linearisation for the code and the phase measurements are then:

$a_m =$	x_m	y_m	z_m	$\Delta clBias_{mf}$	ΔA^s
code	e_x	e_y	e_z	1	0
phase	e_x	e_y	e_z	1	λ

with

$$e_x = \frac{X^i(t_{Tm}) - x_m(t_{Rm})}{\left|\vec{X}^i(t_{Tm}) - \vec{x}_m(t_{Rm})\right|} \quad e_y = \frac{Y^i(t_{Tm}) - y_m(t_{Rm})}{\left|\vec{X}^i(t_{Tm}) - \vec{x}_m(t_{Rm})\right|} \quad e_z = \frac{Z^i(t_{Tm}) - z_m(t_{Rm})}{\left|\vec{X}^i(t_{Tm}) - \vec{x}_m(t_{Rm})\right|}$$

where $e_{x,y,z}$ are the Cartesian coordinates of the unit vector between the receiver (at reception time) and the satellite (at transmission time).

7.1.2 Computational approach

The strategy used here to deal with kinematic GPS data is to process code and phase measurements simultaneously. The unknown parameters are subdivided into two groups : the time dependent and the time independent parameters.

The time dependent parameters refer to one epoch only

- *clock biases*
- *coordinates of the moving receiver*

The time independent parameters are common to two or more epochs

- *coordinates of the moving receiver if at rest*
- *ambiguities of the phase measurements*

The basic idea is to perform a least square estimation in two steps.

In the first step the time independent parameters are estimated. For each epoch all time dependent parameters are eliminated from the normal equation system (NEQ). The reduced NEQ systems are then accumulated over the total time span. The time independent parameters are obtained by inversion.

An important characteristic of the difference between two single difference ambiguities, the so- called double difference ambiguities, is their integer nature. The inversion of the NEQ system leads directly to the floating point solution of the ambiguities. This NEQ system also contains all the information necessary to fix the ambiguities to their appropriate integer values, using a conventional sigma dependent rounding or searching for combinations. However, a secure fixing of the ambiguities is not always possible, i.e. depending on the quality of the measurements and the distance between reference and roving receivers.

In the second step the values of the ambiguities obtained from the first step are used to determine the time dependent parameters, i.e. the coordinates of the moving receiver. The advantage of this procedure, is that it allows for the implementation of the total amount of measurements in estimating the ambiguities, and is therefore best suited for the off-line mode.

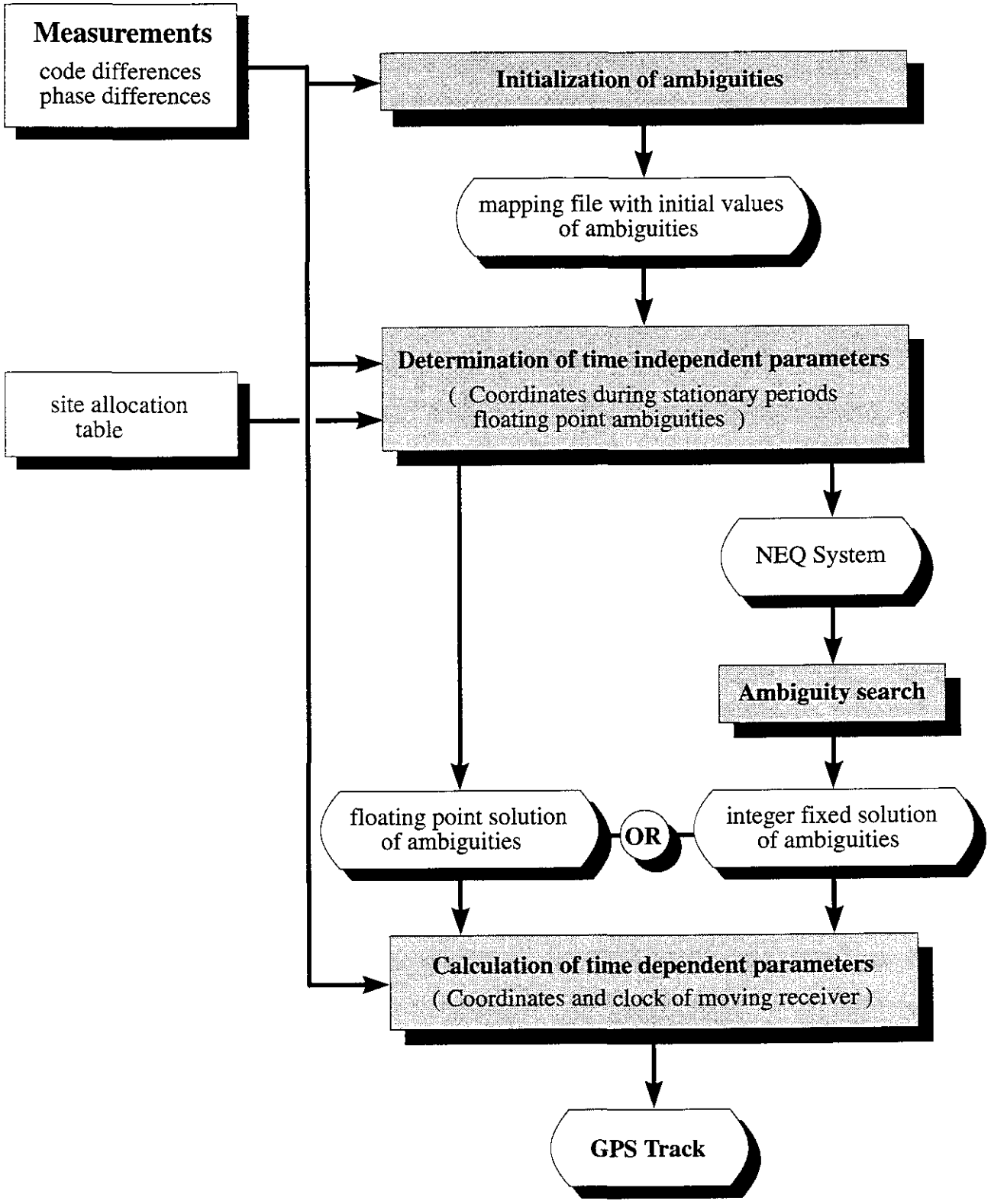

Figure 7.1: Flow-chart of the computational approach.

7.2 Detection of cycle slips

Before processing the data using the above mentioned approach, all data sets have to first be checked for possible cycle slips.

A well known problem in the processing of GPS phase measurements are the jumps of a full number of cycles in the phase measurements, so called cycle slips. The presence and the frequency of cycle slips are good indicators of the quality of GPS receivers. In the new generation of receivers cycle slips are becoming less and less frequent. Nevertheless their presence can never be totally excluded.

The most common procedure for screening GPS data is to look for outliers in the triple differences using L1, L2 measurements or some linear combination of the two basic frequencies. This method works very well in the case of static data, but cannot easily be applied to kinematic data. However, when dual frequency measurements are being used, the following geometry-free linear combination L4 may be applied to detect cycle slips in kinematic data sets.

$$\begin{aligned}\varphi_4[m] &= \varphi_1[m] - \varphi_2[m] \\ &= \lambda_1 \cdot \varphi_1[cy] - \lambda_2 \cdot \varphi_2[cy] \\ &= (d + \Delta cl + \lambda_1 \cdot A_1 + \Delta Ion_1) - (d + \Delta cl + \lambda_2 \cdot A_2 + \Delta Ion_2) \\ &= (\lambda_1 \cdot A_1 - \lambda_2 \cdot A_2) + (\Delta Ion_1 - \Delta Ion_2)\end{aligned}$$

So

$$\varphi_4[m] = const + \alpha \cdot \Delta Ion_1 .$$

By looking at the time differences of subsequent φ_4 measurements, one obtains the following cycle slip indicator :

$$\begin{aligned}\Delta\varphi_4 &= \varphi_4(t_{i+1}) - \varphi_4(t_i) \\ &= \alpha(\Delta Ion(t_{i+1}) - \Delta Ion(t_i)) \\ &\qquad + \lambda_1 \cdot (A_1(t_{i+1}) - A_1(t_i)) - \lambda_2 \cdot (A_2(t_{i+1}) - A_2(t_i)) \\ &\approx \alpha \cdot \tfrac{d}{dt}\Delta Ion \cdot \Delta t + \lambda_1 \cdot \Delta A_1 - \lambda_2 \cdot \Delta A_2\end{aligned}$$

Kinematic data are usually collected at a high frequency, typically from 0.2 to 10 Hz. For such small values of Δt the term $\alpha \cdot \frac{d}{dt}\Delta Ion_1$ may often be neglected. The expectation value for $\Delta\phi_4$ may be written as :

$$\Delta\phi_4 \approx \lambda_1 \cdot \Delta A_1 - \lambda_2 \cdot \Delta A_2$$

where

$\Delta A_1 = A_1(t_{i+1}) - A_1(t_i)$ is a cycle slip in the L1 phase measurement.

$\Delta A_2 = A_2(t_{i+1}) - A_2(t_i)$ is a cycle slip in the L2 phase measurement.

So the indicator allows the determination of a combination of cycle slips in L1 and L2. Theoretically it is possible to have cycle slips in the L1 and L2 which almost compensate for each other. If we assume, however, that the cycle slips in the L2 measurements are independent of the cycle slips in the L1 measurements and that cycle slips are rare events, the probability of a 'double'-cycle slip (simultaneously in L1 and L2) is very small.

7.3 GPS Results

The GPS receivers were permanently tracking during the flight (duration 3-5) hours. Therefore every flight and not every line, as in the case of the gravimetric data, was treated as an entity in the processing. A chronological overview of all lines is given in Figure 7.2. Note that several lines have been flown in two parts on different days. After computation the daily coordinate files were separated in line specific files (1 file per line).

Since the capacity of the internal memory of the receivers operating at 2 Hz was too small, the data was transferred directly to laptop computers using the commercial Trimble software. Unfortunately, a certain percentage of epochs were lost during this transfer. (5% to 15%). At the stationary ground stations it was possible to linearly interpolate the measurements without loss of accuracy. However, because of the dynamics of the aircraft, we renounced this interpolation for the roving receivers.

In the processing of GPS data, especially in the static mode, it is often the case that only measurements to satellites rising over a minimal elevation angle are included. Measurements at low elevation are noisier, because the signal strength is lower and the path delay through the atmosphere larger. However, discarding measurements may weaken the geometry of the solution, especially in the kinematic mode with a poor satellite constellation. Because the constellation was quite poor in 1992, no cut-off angle was introduced. Therefore, by combining the same roving data set with different reference stations, the resulting constellation of the simultaneously observed satellites differs slightly. Not all satellites at low elevation were tracked by every reference station.

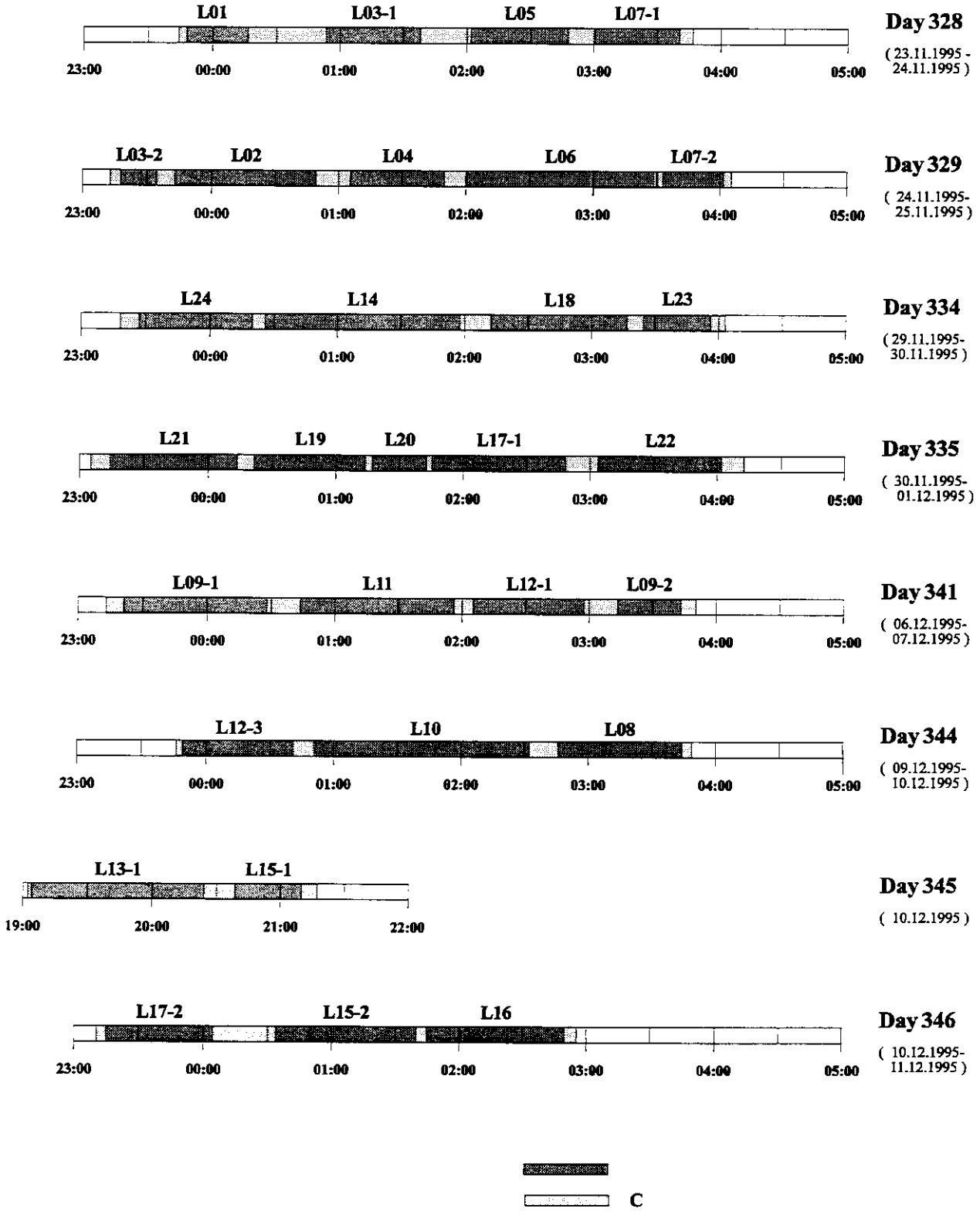

Figure 7.2 : Chronological overview of all lines. (All times are related to GPS time)

For the computation of the data set, the following strategy was applied :

During the whole campaign, two receivers were installed on board the airplane, one single and one dual frequency receiver. The dual frequency receiver was operated on the rear antenna on days 328 and 329, then on the front antenna on days 334, 335, 341, 344, 345, 346.

The data from the dual frequency receiver was combined with those of all the reference stations (Zimmerwald, Zurich, Lausanne, Engadin) separately, leading to 4 different combinations (Rover-Reference). For every combination two different solutions were calculated. The relevant parameters of the two solutions denoted by A and B are summarized in Table 7.1.

Solution A (single frequency solution)	Solution B (quasi ionosphere free solution)
L1 code measurements	L1 code measurements
L1 phase measurements	L1 & L2 measurements
a prior RMS :	a priori RMS :
σ_{phase} = 1 cm	σ_{phase} (L1/L2) = 1 cm
σ_{code} = 1 m	σ_{code} = 1 m
No stochastic ionosphere biases	stochastic absolute ionosphere biases with a priori RMS of 2 m
No Ambiguity fixing.	No Ambiguity fixing.

Table 7.1: Relevant processing parameters used

For both solutions a secure fixing of the ambiguities was not possible. This was due to the poor satellite constellation, the long distances (up to 300 km) from the rover to the reference station and the quality of the code measurements from the Trimble SST which were rather poor when compared to the newer SSE or SSI models, that are now available. The estimated real valued ambiguities were therefore used for the computation of the coordinates.

Solution A is based on single frequency code and phase measurements only, whereas solution B integrates phase measurements on both frequencies, allowing for the elimination of systematic errors introduced by the ionosphere. Solution B is therefore less biased. However, by combining the basic L1 and L2 measurements to obtain the ionosphere free combination, the measurement noise is increased. Solution B also requires the presence of L2 measurements.

For comparison and integration of GPS coordinates in the computation of gravity anomalies, one solution was chosen. The results showed an overall better agreement of solution type B (ionosphere free combination) compared to solution type A (single frequency solution). Therefore we only took solutions from type B and chose the reference station for every line separately. This choice is based on the following criteria, given in order of their priority.

1. *Completeness of the track.*
2. *Best resulting differential satellite constellation.*
3. *Minimization of the distance to the reference station.*

Once the reference had been selected, all remaining solutions were compared to this reference solution.

As an illustration, Figures 7.3a-b show the obtained results for Lines 9-1 and 11. Since the height is the most critical component of the 3D-coordinates, only height and height differences are included in the figures. Note that in general the quality of the horizontal components is a factor of 2-3 better. The quality of the constellation for every combination, with the different reference stations, is given by the number of differentially available satellites and the PDOP value, both as a function of time. The PDOP (Positioning Dilution Of Precision) only depends on the geometry. In absence of systematic errors, the standard deviation of the position would correspond to the standard deviation of the measurement (single difference phase measurements in this case) multiplied by the PDOP value.

The selected examples illustrate the different quality of the satellite constellation.

Line 9.1 is a typical result. The number of observed satellites varies from 5 to 6 and small differences in the differential constellation, using Zimmerwald, Zurich, Lausanne or Engadin as reference stations, can be noticed. As expected, there was more agreement for the case of the ionosphere free solutions (Figure 7.3a) than for the case of the single frequency solutions (Figure 7.3b).

Figures 7.3c-d show a worst case. Again better agreement is obtained by using the ionosphere free solution, especially for the second part of the line 11, where the constellation is more stable. It may happen that the receiver is able to track on the L1 and not on the L2-band. However, for the computation of the ionosphere free combination both measurements (on L1 and L2) are required. This led, in the case of line 11, to an additional weakening of the solution during the first part (Figure 7.3d), where a solution using Zurich or Engadin as reference station was partially not possible. The number of available satellites dropped under the minimum level of 4 satellites.

A systematic comparison of all solutions for all lines is summarized in Table 7.2. Again only the most critical component, the height is analyzed.

For the computation of the different solutions presented in Table 7.2, the same kinematic GPS data is used. Only the data from the reference station differ. The discrepancies are mainly introduced by systematic errors and not by measurement noise. The systematic errors, however, depend on the relative placement of the airplane with respect to the reference station. Therefore a comparison obtained by using different reference stations gives a realistic impression of the absolute accuracy of the computed coordinates. There are, in fact, no other possibilities for quality assessment.

The overall quality of the coordinates is in the order of 50 cm or better.

LINE	REFERENCE	ZIMM (L3)	ZURI (L3)	LAUS (L3)	ENGA (L3)	ZIMM (L1)	ZURI (L1)	LAUS (L1)	ENGA (L1)
				DAY 328					
LINE 01.1	ZIMM (L3)	o	0.079 m	0.321 m	-	0.317 m	0.124 m	0.419 m	-
LINE 03.1	LAUS (L3)	0.733 m	1.088 m	o	-	1.223 m	0.894 m	0.624 m	-
LINE 05.1	ZURI (L3)	0.719 m	o	0.561 m	-	3.988 m	0.251 m	0.810 m	-
LINE 07.1	LAUS (L3)	0.785 m	0.184 m	o	-	3.101 m	0.338 m	0.902 m	-
				DAY 329					
LINE 03.2	ZIMM (L3)	o	0.579 m	0.667 m	0.328 m	0.500 m	1.035 m	0.502 m	0.594 m
LINE 02.1	ZIMM (L3)	o	0.293 m	0.819 m	0.205 m	0.826 m	0.697 m	0.395 m	0.682 m
LINE 04.1	ZIMM (L3)	o	0.087 m	1.032 m	0.307 m	0.964 m	0.508 m	0.362 m	0.172 m
LINE 06.1	ZIMM (L3)	o	0.231 m	0.555 m	0.453 m	0.166 m	0.209 m	0.266 m	0.509 m
LINE 07.2	ZIMM (L3)	o	0.260 m	0.454 m	-	0.121 m	0.254 m	0.218 m	0.704 m
				DAY 334					
LINE 24.1	LAUS (L3)	0.098 m	0.140 m	o	0.055 m	0.170 m	0.105 m	0.120 m	0.405 m
LINE 14.1	ENGA (L3)	0.249 m	0.107 m	0.093 m	o	0.463 m	0.243 m	0.162 m	0.190 m
LINE 18.1	ENGA (L3)	0.293 m	0.094 m	0.041 m	o	0.486 m	0.078 m	0.043 m	0.145 m
LINE 23.1	LAUS (L3)	0.066 m	0.938 m	o	0.120 m	0.708 m	0.744 m	0.066 m	0.287 m
				DAY 335					
LINE 21.1	ENGA (L3)	0.379 m	0.198 m	0.062 m	o	0.329 m	0.176 m	0.497 m	0.087 m
LINE 19.1	ENGA (L3)	0.292 m	0.204 m	0.246 m	o	0.176 m	0.232 m	0.173 m	0.024 m
LINE 20.1	ZIMM (L3)	o	0.496 m	0.749 m	0.422 m	0.146 m	0.409 m	0.378 m	0.293 m
LINE 17.1	ZIMM (L3)	o	0.139 m	0.361 m	0.074 m	0.077 m	0.584 m	0.476 m	0.210 m
LINE 22.1	ZIMM (L3)	o	0.168 m	0.129 m	0.124 m	0.211 m	0.600 m	0.455 m	0.242 m
				DAY 341					
LINE 09.1	ZIMM (L3)	o	0.163 m	0.168 m	0.133 m	0.084 m	0.372 m	0.149 m	0.606 m
LINE 11.1	ZIMM (L3)	o	0.206 m	1.697 m	0.408 m	0.077 m	0.442 m	1.851 m	1.382 m
LINE 12.1	ZIMM (L3)	o	0.116 m	0.048 m	0.044 m	0.062 m	0.140 m	0.307 m	0.262 m
LINE 09.2	ZIMM (L3)	o	0.104 m	0.143 m	0.192 m	0.123 m	0.396 m	0.032 m	0.667 m
				DAY 344					
LINE 12.3	ZIMM (L3)	o	0.243 m	0.236 m	0.056 m	0.132 m	0.313 m	0.190 m	0.518 m
LINE 10.1	ZIMM (L3)	o	0.060 m	0.172 m	0.172 m	0.060 m	0.371 m	0.154 m	0.178 m
LINE 08.1	ZIMM (L3)	o	0.179 m	0.088 m	0.217 m	0.075 m	0.715 m	0.261 m	0.137 m
				DAY 345					
LINE 13.1	ZIMM (L3)	o	0.170 m	0.173 m	0.143 m	0.540 m	0.549 m	0.413 m	0.539 m
LINE 15.1	ZIMM (L3)	o	1.752 m	4.351 m	-	2.802 m	2.935 m	4.224 m	-
				DAY 346					
LINE 17.2	ENGA (L3)	0.448 m	1.072 m	0.588 m	o	0.619 m	0.098 m	0.089 m	0.518 m
LINE 15.2	ZIMM (L3)	o	2.032 m	2.485 m	0.613 m	0.512 m	1.224 m	2.137 m	1.612 m
LINE 16.1	ZIMM (L3)	o	0.403 m	0.175 m	0.064 m	0.411 m	0.462 m	0.397 m	0.258 m

Table 7.2: RMS of the height differences of all computed solutions with respect to a reference solution.

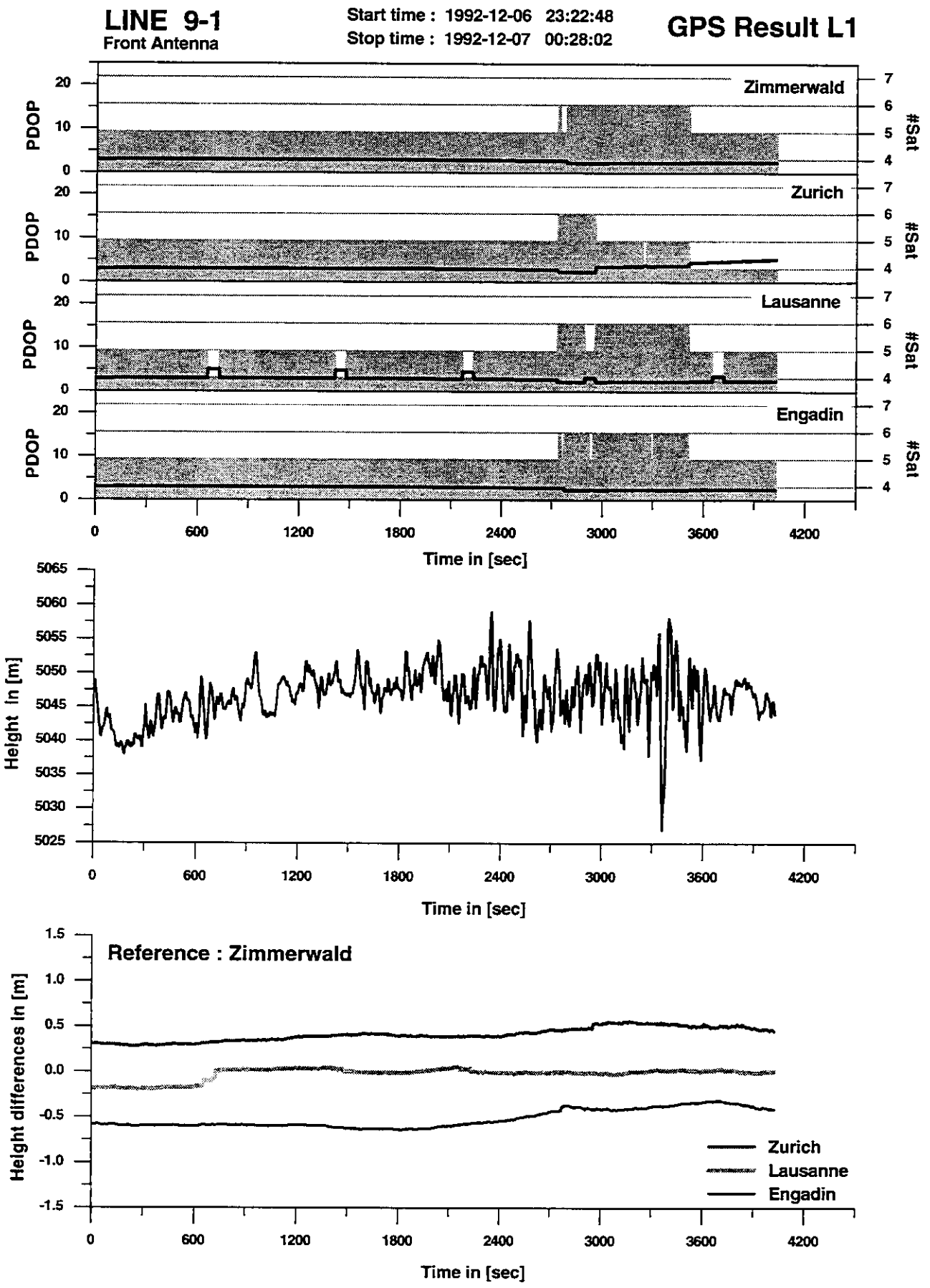

Figure 7.3a: Comparison of the height component using different reference stations.
(Line 9.1 single-frequency result)

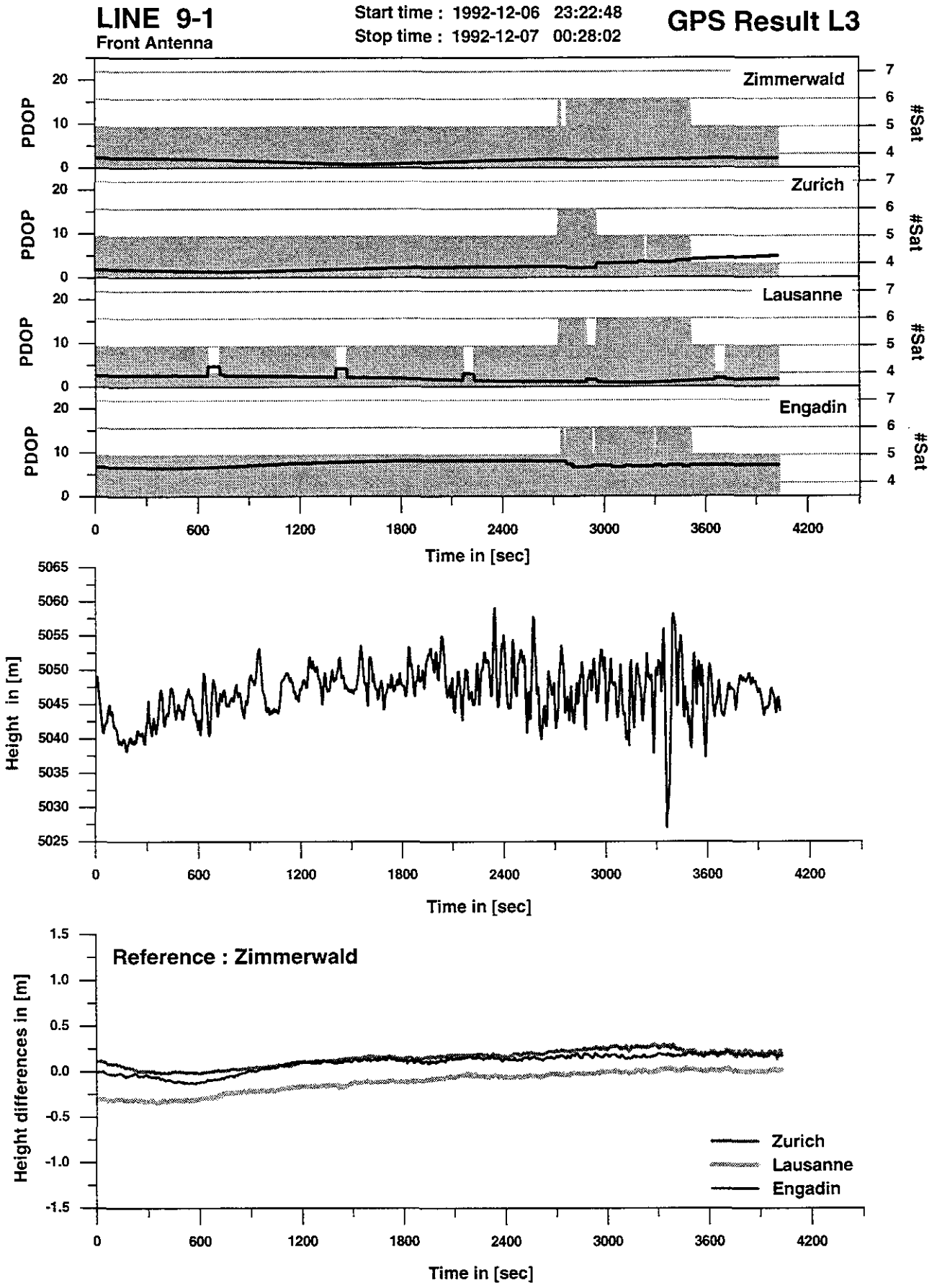

Figure 7.3b: Comparison of the height component using different reference stations.
(Line 9.1 ionosphere free combination from dual frequency measurements)

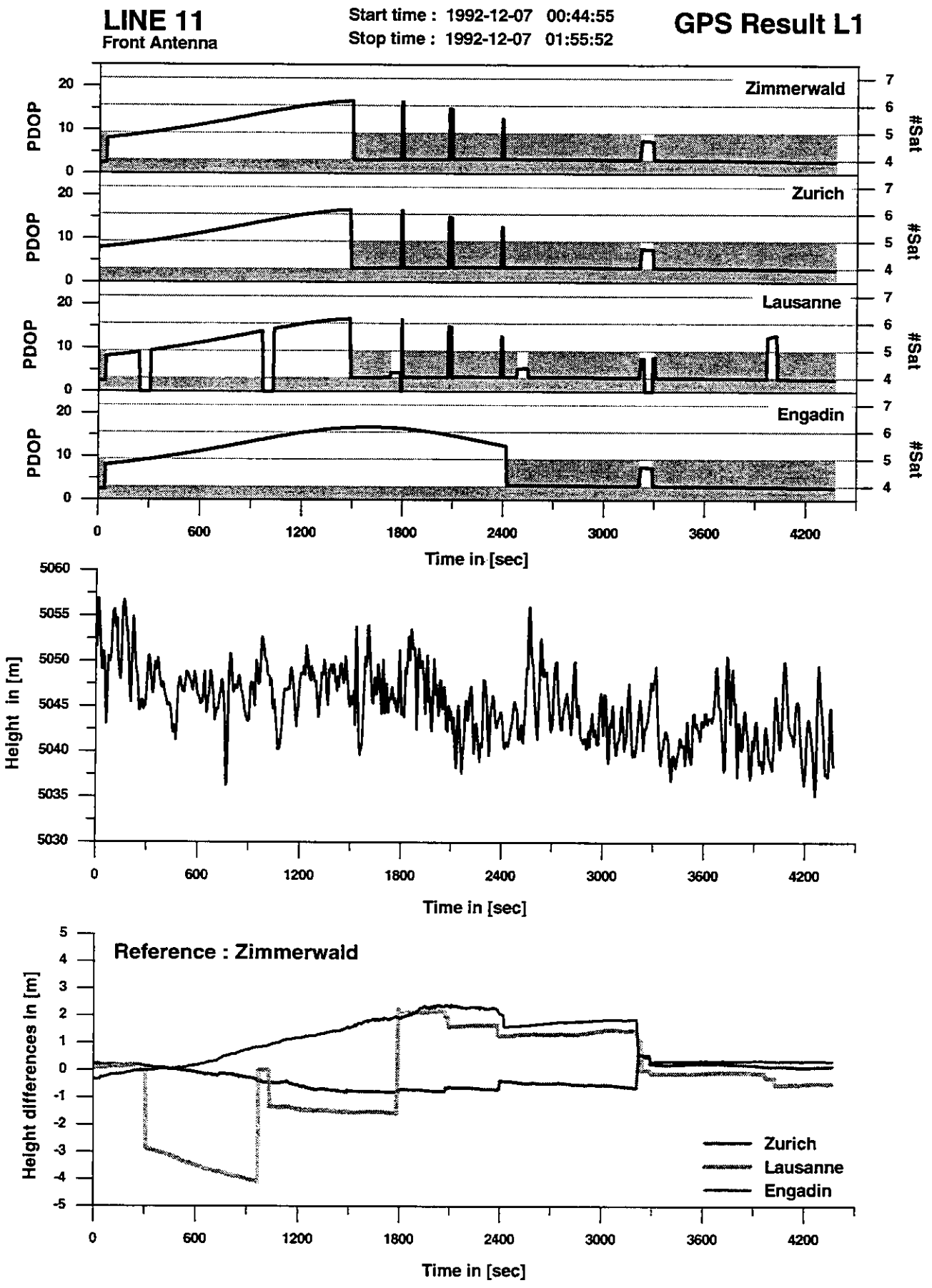

Figure 7.3c: Comparison of the height component using different reference stations.
(Line 11 single-frequency result)

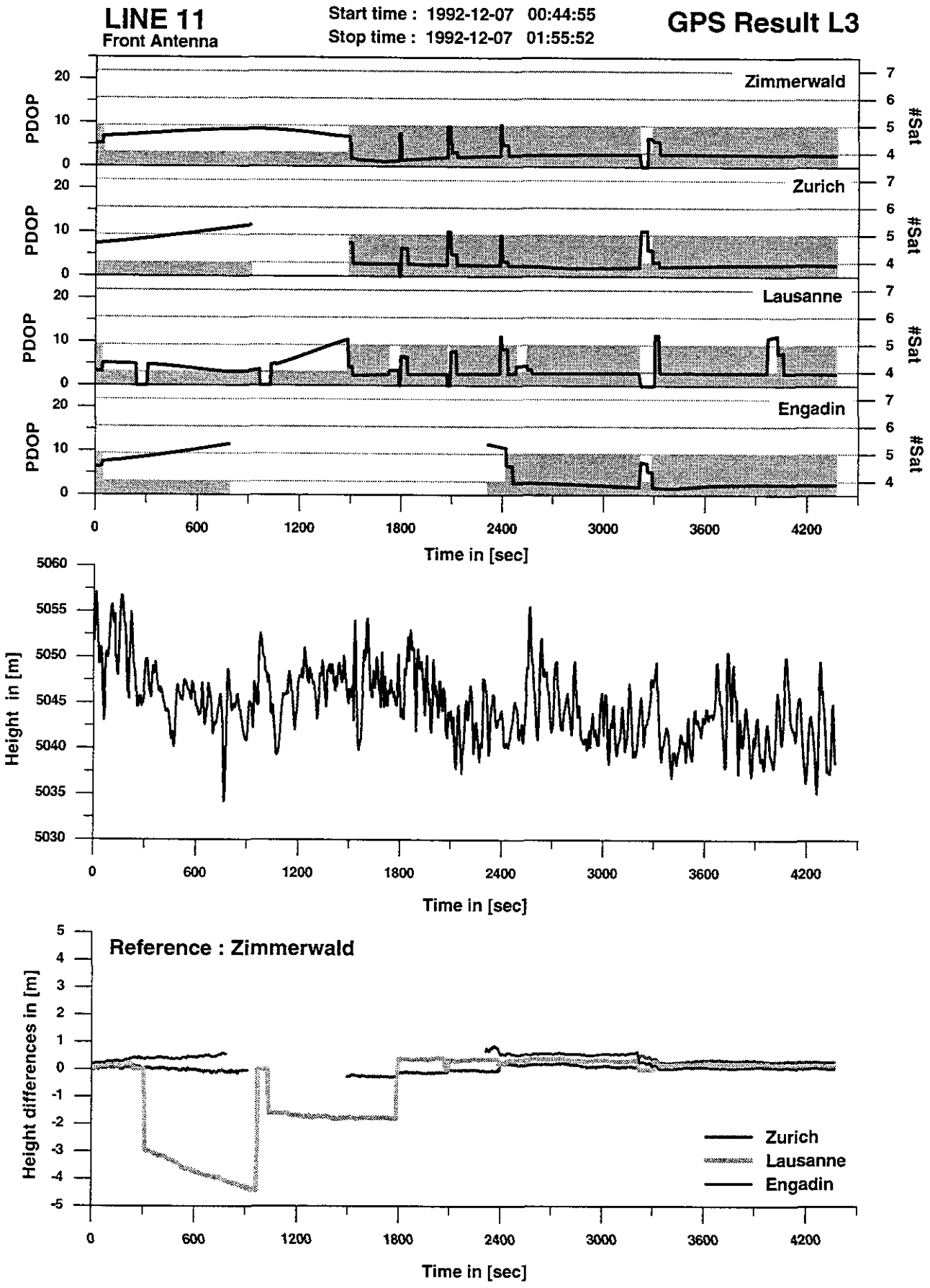

Figure 7.3d: Comparison of the height component using different reference stations.
(Line 11 ionosphere free combination from dual frequency measurements)

7.4 Error budget

The main problem, when processing GPS data is the elimination of systematic errors. In the static mode the daily repeatability is often used as a quality indicator. Here, the quality assessment is based on the comparison of solutions, using different reference stations. The measurement noise itself is in the order of 2-5 mm for the phase measurements. By error propagation a standard deviation of some millimeters (up to 2 cm), depending on the actual PDOP value, may be expected for the coordinates.

Unfortunately, there are systematic errors that stem from different sources :

Orbit errors : Actually orbit errors are no longer a serious problem in post processing, due to the availability of precise orbits. Since 1992, the International GPS Service for Geodynamics (IGS) provides the user with high quality GPS Ephemerides. A simple formula, to estimate the effect of orbit biases on the coordinate determination, is given by (Bauersima, 1983) :

$$\frac{|\delta b|}{|b|} = \frac{|\delta r|}{|r|}$$

where :

$|\delta r|$ represents the orbit error of the satellite and $|r|$ the distance to the satellite (about 25000 km in the mean).

$|\delta b|$ is the resulting error in the coordinates and $|b|$ the distance between reference station and moving receiver (in the kinematic case).

IGS claims a quality of about 10 cm for their final result, the so called IGS Official Orbit (Combined). By putting $|b|$ = 250 km, for example, the resulting error of the coordinates is 1 mm and can be neglected. For all computations of the present data sets, only IGS orbits have been used.

Ionospheric path delay : The ionosphere is a part of the atmosphere, situated above the troposphere and the stratosphere. It is characterized by the presence of ionized particles, provoking a frequency dependent path delay of the GPS signal.

The path delay is dependent on the activity of the ionosphere, showing a strong daily variation. During the night the influence is about 3-4 times lower. Most of our data stem from night flights. If only L1 measurements as in the case of solution type A are used, the resulting distortion in the coordinates due to the ionospheric path delay may be estimated by the following formula (Beutler et al. 1987) :

$$Relative\ Iono.\ Error[ppm] = 0.7 \cdot 10^{-17} TEC$$

where *TEC* denotes the Total Electron Content given in [electrons / m^2].

At night a typical value $TEC = 10^{17}$ may be assumed. For a distance of 250 km this leads to an error of about 20 cm.

Due to the frequency dependency, the ionospheric biases in the L1 and L2 measurements are different and it is possible to eliminate them by using the appropriate linear combination (solution type B). This ionosphere free combination is often referred to as L3 combination. A small disadvantage, however, in using the L3 combination is an increase of the measurement noise by a factor of 3.1, compared to the noise of the basic L1 and L2 measurements.

Tropospheric path delay : The troposphere introduces a path delay which is independent of the frequencies (in the L-band). To account for the tropospheric path delay, the model given by (Saastamoinen, 1973) was implemented, and surface meteorological data derived from a standard model of the troposphere were used. In many static applications over small distances and height differences, the errors of the model are nearly compensated in the differential mode. This is not true in our case. All lines were flown at a height of about 5100 m, whereas the reference stations were on ground at heights varying from 400 m (Lausanne) to 1720 m (Engadin).

The differential error may therefore be assumed to be similar to the absolute error of the Saastamoinen model. Deviations of 5 to 10 cm for the zenith path delay are realistic. In the case of a homogenous satellite distribution this systematic error affects mainly the height component, leading to an error which is 2-3 times larger than the error of the zenith path delay (Geiger, 1987). Maximal errors of 40 cm may therefore corrupt the calculated coordinates.

Multipath : Multipath errors result from interference between the direct signal and signals which have first been reflected before reaching the antenna. They are periodical and may reach amplitudes of several centimeters.

Floating point ambiguities : One of the main error sources is induced by the error in the estimates of the real valued ambiguities. This error is dependent on the quality of the constellation, the time span of uninterrupted phase measurements and the quality of the code measurements. Even if this error cannot be considered as a systematic error, stemming from some external source such as i.e. the tropospheric path delay, its influence on the resulting coordinates, however, is similar. In a first approximation, it leads to an offset and a linear drift of the coordinates over smaller time spans as can be seen in the results of line 11 presented in Figures 7.3c-d. In the case of a bad constellation, there can be many interruptions in the phase measurements and offsets of several meters are possible.

Common to many systematic errors, where floating point ambiguities and tropospheric path delay play the most important role, is a smooth variation with time. Therefore, they do not strongly affect the determination of velocity and acceleration. However, jumps may occur between epochs with changes in constellation.

7.5 Combining front and rear antennas

The vector from the rear to the front antenna was computed directly without including data from ground based reference stations. The big advantage here is the small distance (about 4 m) between the two antennas. Since one of the receivers was a single frequency receiver, only a L1 solution was possible. Over such small baselines, most of the systematic errors were canceled and the fixing of the ambiguities didn't cause any problems.

Figure 7.4 illustrates the result obtained for the vector rear-front antenna for line 9-1.

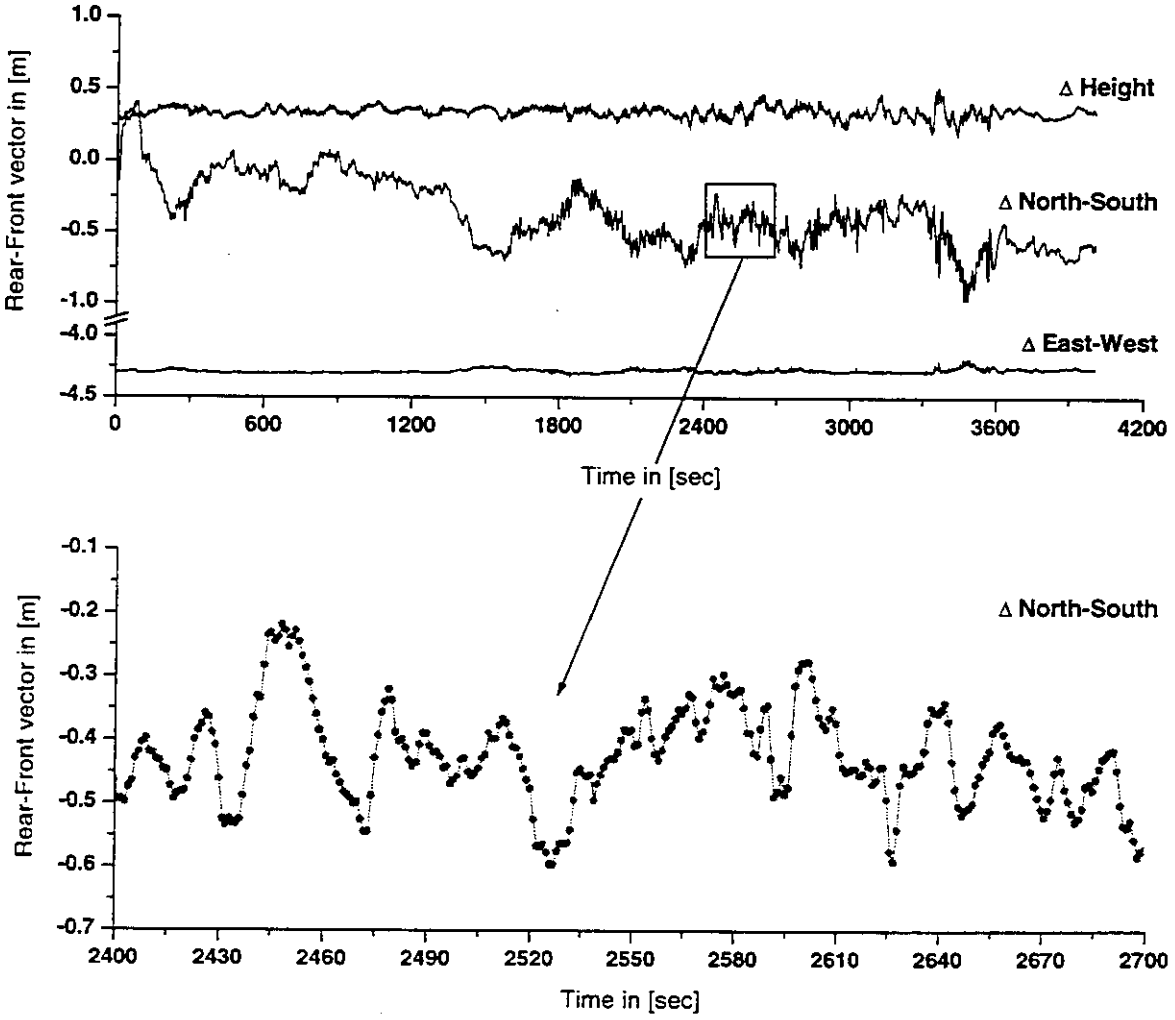

Figure 7.4 : Components (NS, EW, H) of the vector rear-front antenna as a function of time obtained from an ambiguity fixed L1 solution. **(Line 9-1)**

7.6 Interface with gravimetric processing

The primary result of all GPS computation are geocentric Cartesian coordinates.

As already mentioned, precise IGS ephemerides for the satellite positions were introduced. They are given in the International Terrestrial Reference Frame (ITRF). Additionally, the ITRF coordinates of the Swiss fundamental station Zimmerwald were used.

- All reference stations are connected by means of static baselines to Zimmerwald.
- The final solution for the dual frequency receiver is connected to one of these reference stations.
- The antenna coordinates of the additional single frequency receiver are related to those of the dual frequency one, both on board the airplane.

Hence, all coordinates are related to ITRF (see Figure 7.5). The ellipsoidal parameters of ITRF are identical to those of WGS84 (World Geodetic System 84).

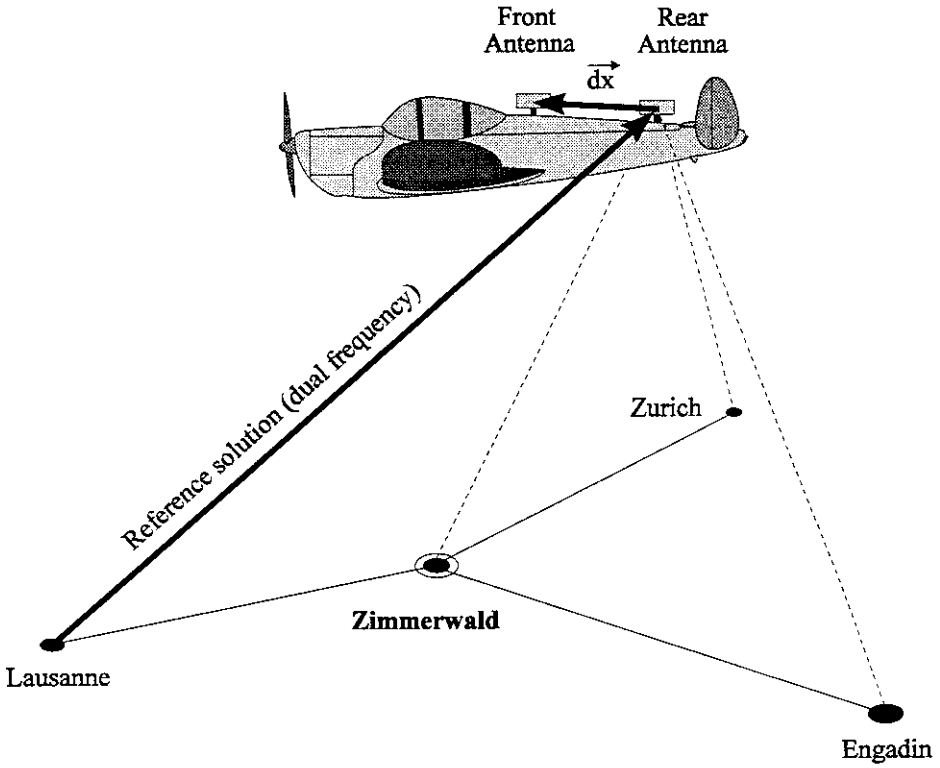

Figure 7.5: From all ground stations, previously connected to Zimmerwald, the best station was used to compute an ionosphere free reference solution based an dual frequency measurements. The remaining stations allowed a comparison of the obtained trajectories. Additionally a single-frequency solution for the differential vector rear-front antenna was directly computed.

For integration of the GPS result in the gravimetric processing, the following additional preparation step became necessary :

As already mentioned, missing epochs on the ground stations were filled by interpolation of the raw measurements. Because of the dynamics of the airplane, this interpolation was not suited for the kinematic data sets. Hence, several epochs were still missing from the resulting 2 Hz coordinate files. However, for the integration of the GPS result into the gravimetric processing a complete and equally spaced data set was mandatory. Furthermore, velocity information had to be derived from the coordinates.

A spacing of 1 sec, corresponding to the gravimetric data frequency was adopted. A running window of 5 data points (Δt = 2 sec) around the central epoch was used. The coordinates of the central epoch were then represented by a polynomial fit of degree 2.

From this polynomial representation, the coordinates and velocity of the rear antenna were obtained with respect to the ITRF. The difference vector from the rear to the front antenna was calculated by a similar procedure.

In a next step, Cartesian coordinates were transformed into ellipsoidal (latitude, longitude, height) using the associated ellipsoidal parameters (mean axis, eccentricity) of the ITRF system. Velocity and difference vectors were rotated in the local system, defined by the ellipsoidal latitude and longitude. This decomposition of the velocity vector allowed a deduction of a horizontal velocity and the azimuth, which was used for the computation of the Eötvös effect.

Table 7.3 gives an example of the GPS file, containing the necessary information for the integration of the GPS result in the gravimetric processing.

```
| AeroGrav92 |              GPS Results  (L3  Floating Point Solution)              | 1995-JUN-29   16:57: 6 |
| Line Nr.              > 09.1
| Start Time  (GPS)     > 1992-DEC- 6   23:22: 1.0
| Stop Time   (GPS)     > 1992-DEC- 7    0:28:50.0
| Reference Station     > ZIMMERWALD
| GDOP min/mean/max     >     2.30    5.18    7.00
|  1 = GPS Time [Sec of Day]
|  2 = Latitude [deg]      3 = Longitude [deg]    4 = Height [m]         (ITRF coordinates of rear antenna)
|  5 = Delta-NS [m]        6 = Delta-EW  [m]      7 = Delta-Height [m]   (from rear to front antenna)
|  8 = Dist. to EarthCenter [m]
|  9 = Horz. Speed [m/sec]                       10 = Azimuth [deg]
| 11 = GDOP   12 = #sat.  13 = Constellation Change     14 = Delta-Time of Interpolation [sec]
 84121.0 46.99031272  8.52988099 5048.3769 -0.0486 -4.3031  0.3023 6371795.436  54.483 261.57051  7.0 5 1  0.0
 84122.0 46.99023934  8.52917278 5048.0098 -0.0787 -4.3033  0.3009 6371795.097  54.580 261.21292  7.0 5 0  0.0
 84123.0 46.99016285  8.52846394 5047.6294 -0.0990 -4.3038  0.3006 6371794.745  54.677 260.90568  7.0 5 0  0.0
 84124.0 46.99008402  8.52775441 5047.2214 -0.1188 -4.3046  0.2878 6371794.366  54.773 260.68473  7.0 5 0  0.0
 84125.0 46.99000351  8.52704398 5046.8363 -0.1391 -4.3046  0.2792 6371794.011  54.871 260.53559  7.0 5 0  0.0
 84126.0 46.98992184  8.52633252 5046.5136 -0.1488 -4.3039  0.2815 6371793.719  54.966 260.44175  7.0 5 0  0.0
 84127.0 46.98983946  8.52562003 5046.2431 -0.1472 -4.3038  0.2820 6371793.479  55.048 260.41401  7.0 5 0  0.0
 84128.0 46.98975711  8.52490659 5046.0484 -0.1431 -4.3016  0.2950 6371793.315  55.103 260.47950  7.0 5 0  0.0
 84129.0 46.98967569  8.52419238 5045.9212 -0.1331 -4.2990  0.2989 6371793.218  55.135 260.65599  7.0 5 0  0.0
 84130.0 46.98959623  8.52347736 5045.8068 -0.1098 -4.2996  0.2951 6371793.133  55.154 260.93704  7.0 5 0  0.0
 84131.0 46.98951956  8.52276154 5045.6636 -0.0817 -4.2988  0.2937 6371793.019  55.161 261.32262  7.0 5 0  0.0
 84132.0 46.98944667  8.52204482 5045.5058 -0.0530 -4.2996  0.2836 6371792.888  55.165 261.81568  7.0 5 0  0.0
 84133.0 46.98937843  8.52132708 5045.3163 -0.0147 -4.3017  0.2783 6371792.724  55.165 262.39535  7.0 5 0  0.0
```

Table 7.3: Example of a GPS result file for the integration in the gravimetric processing (line 9-1).

8 The synchronization of GPS and gravimeter data

An analysis of the measurements recorded by the gravimeter has shown that some problems affected the time tagging of the gravimeter data. In the series, records were found with the same time tag as records with time differences larger than the meter's sampling rate of one second. It seems that there were different types of errors occurring by time tagging e.g. rounding off the exact time. This caused an occasional isolated higher or lower time of one second. Also, disk cache problems caused errors by giving the same time tag for two different records. Figure 8.1 show, as an example, the time shift between GPS and meter data for line 22.

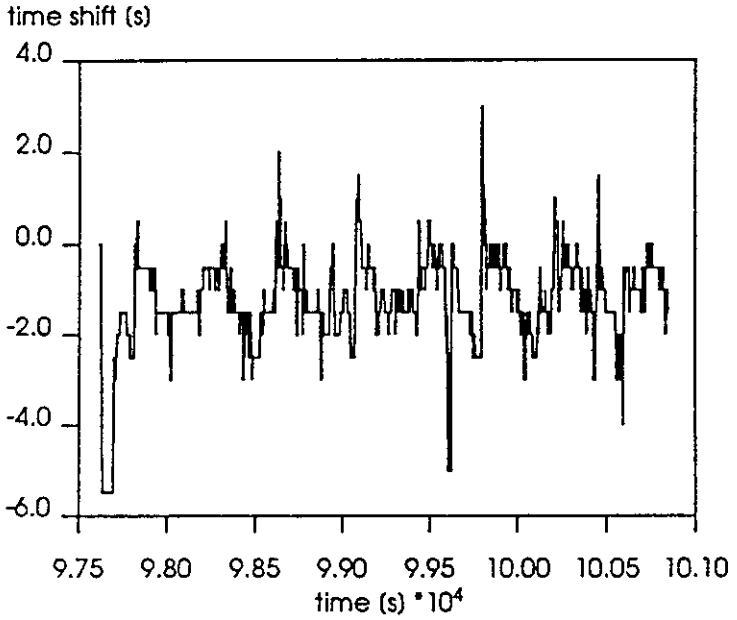

Figure 8.1: Time shift between GPS and gravimeter data for line 22, before correction.

Therefore, in order to synchronize the gravimeter data to the GPS data it was not enough to compute a constant time shift for the whole series. To solve this problem a moving cross correlation procedure was used in combination with Kalman filtering (Klingelé et al. 1993).

The cross correlation procedure was computed over a moving window of 100 seconds between the vertical acceleration computed by the estimator of the motion of the aircraft through GPS measurements and the estimated acceleration from the meter data. In order to do this, a Kalman filter was run on the meter data without compensation of the vertical acceleration of the gravimeter case. In this case, the filter estimates the total acceleration registered by the meter, i.e. the sum of the aircraft's acceleration and of the gravity acceleration. It is easy to see in Figure 8.1 that the time shift is time dependent with a periodical component. The peaks are due to numerical effects of computing the cross correlation.

In order to correct the data, the meter records were first ordered by incrementing the time tag by one second, starting by the first sample, and the cross correlation procedure was run again. In Figure 8.2 the resulting time shift is presented. The shift increases regularly by 0.5 second steps. The jump at second 99554 is due to the absence of measurements for 8 seconds on the gravimeter data file. The time tags of the incremental data file are now corrected using these time differences. Again, the Kalman filter is run on the corrected data and a new cross correlation is performed. Figure 8.3 shows the effect of the last correction. The two series are now synchronized with an accuracy of approximately 0.5 second.

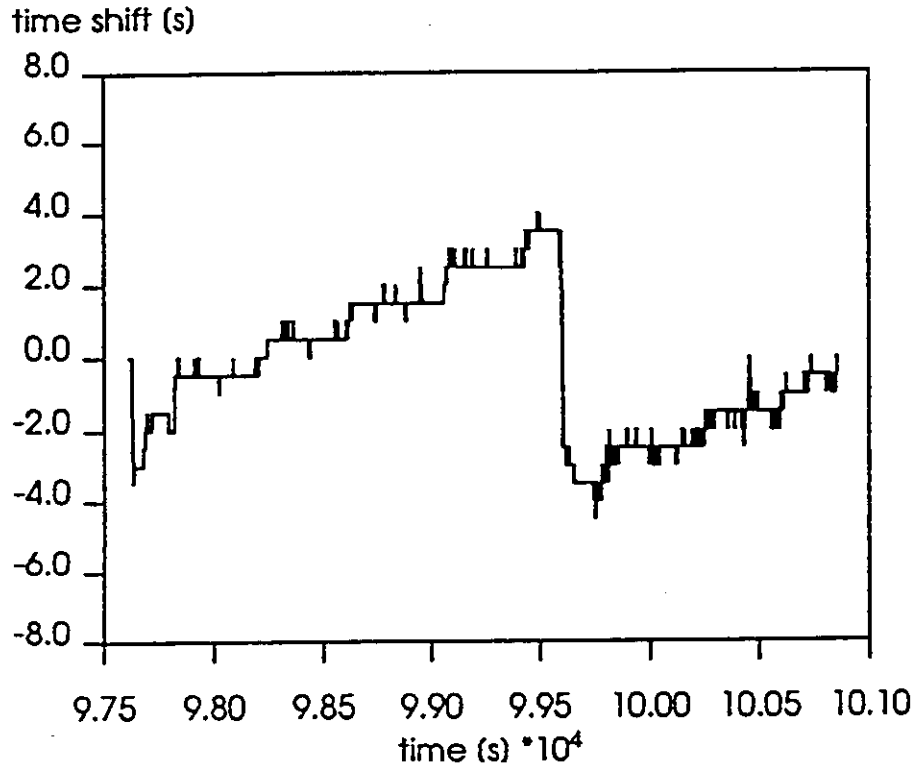

Figure 8.2: Uncorrected time shift between GPS and incremental gravimeter data for line 22, before corrections.

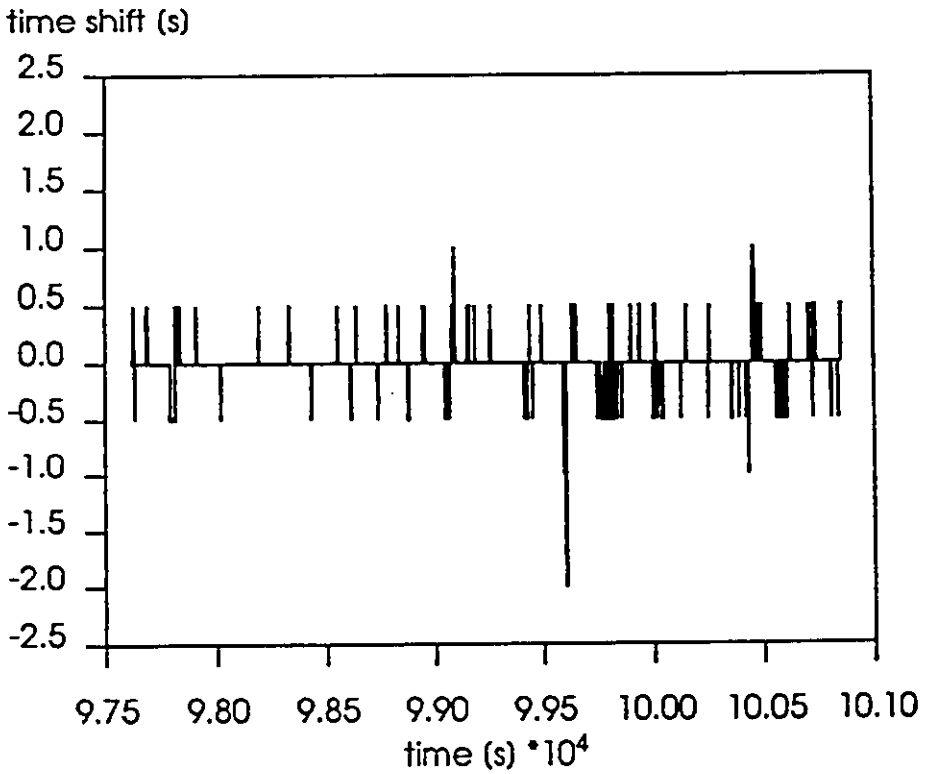

Figure 8.3: Time shift between GPS and gravimeter data for line 22, after corrections.

9 Data Processing

9.1 Introduction

For the computation of *g*, only three types of information are needed from the gravimeter-platform system: The cross-coupling corrections, the raw beam positions and the raw spring tensions. Within the framework of this project two approaches were tried for the computation of *g* and the anomalies. The classical one, using recursive and transverse filters and a more modern one, using adaptive extended Kalman filters. The second method was not adopted for producing final results because it showed that the computed anomalies presented some discontinuities which are not compatible with potential field data (discontinuous derivatives). Also this method is very time-consuming computer wise and the criteria needed for modeling the noise system are quite subjective.

9.2 Reformatization

The data recorded by the system contain the following data (for each sample) : The line number, date (y,m,d), the time (h,m,s), raw and filtered beam positions, raw and filtered spring tensions, a value of *g* computed from the filtered two preceding values, the output voltage of the two horizontal accelerometers placed on the top of the stabilized platform (cross and long accelerometers) and finally three voltages produced by three analogue channels. These three channels contain the pitch and roll voltages and the barometric altitude.

It is clear that some information is redundant, e.g. date and line number, and some is not used for the computation e.g. : the filtered values, the accelerometers voltages and the computed *g* value.

In order to reduce the size of the information all the redundant and not used data were eliminated. During the same procedure the badly recorded samples were also eliminated and replaced by interpolated ones. When only one bad "record" was found between two good ones, it was only replaced by the mean value of the samples situated before and after. When more than one bad record were consecutively found, the missing data were replaced by spline interpolated values. For this, one hundred values before and after the "hole" were used for the interpolation. Table 9.1 shows a typical example of a sequence containing a bad record.

```
LINE14E 11/30/92 1:23:00 10097.1 119.242   128.8 9561.836 10066.311
LINE14E 11/30/92 1:23:01 10088.9 121.512   128.5 9552.810 10058.731
LINE14E 11/30/92 1:23:02 10080.8 120.695   128.3 9538.940 10051.080
LINE14E 11/30/92 1:23:03 10072.6 118.986   128.0 9531.128 10043.361
LINE14E 11/30/92 1:23:04 10064.4 117.325   127.8 9521.914 10035.574
LINE14E 11/30/92 1LINE14E 11/30/92 1:26:32  9291.4 113.639   114.5
LINE14E 11/30/92 1:26:33  9291.4 113.211   114.5 9274.985 9275.982
LINE14E 11/30/92 1:26:34  9291.4 114.835   114.5 9274.985 9275.941
LINE14E 11/30/92 1:26:35  9291.4 115.470   114.5 9274.985 9275.901
LINE14E 11/30/92 1:26:36  9291.3 115.409   114.5 9274.985 9275.863
LINE14E 11/30/92 1:26:37  9291.3 115.543   114.5 9274.985 9275.827
LINE14E 11/30/92 1:26:38  9291.2 114.481   114.5 9274.985 9275.791
LINE14E 11/30/92 1:26:39  9291.1 114.969   114.5 9274.985 9275.758
LINE14E 11/30/92 1:26:40  9291.1 114.469   114.5 9274.985 9275.726
LINE14E 11/30/92 1:26:41  9291.0 114.420   114.4 9274.985 9275.695
LINE14E 11/30/92 1:26:42  9291.0 113.822   114.4 9274.985 9275.665
LINE14E 11/30/92 1:26:43  9290.9 113.956   114.4 9274.985 9275.636
LINE14E 11/30/92 1:26:44  9290.9 114.029   114.4 9274.985 9275.609
LINE14E 11/30/92 1:26:45  9290.8 114.212   114.4 9274.985 9275.583
LINE14E 11/30/92 1:26:46  9290.8 114.115   114.4 9274.985 9275.558
LINE14E 11/30/92 1:26:47  9290.8 114.432   114.4 9274.985 9275.534
LINE14E 11/30/92 1:26:48  9290.7 114.518   114.4 9274.985 9275.511
```

Table 9.1: Example of a series of recorded data containing a bad record in the 6th row

A summary of the flight altitudes, coordinates of the beginning and end of each line, the date of flight and the number of bad records is given in Table 9.2.

Nr	Date	Begin	End	H_{min}	H_{max}	N
01.1	24.11.92	587'551 / 282'249	719'956 / 313'689	5192	5184	4
02.1	25.11.92	733'987 / 304'778	547'531 / 260'205	5150	5130	43
03.1	24.11.92	659'335 / 275'047	527'437 / 243'583	5190	5184	15
03.2	25.11.92	671'391 / 277'853	735'850 / 293'193	5151	5139	11
04.1	25.11.92	539'287 / 233'528	749'006 / 283'926	5146	5132	14
05.1	24.11.92	559'746 /226'443	759'731 / 274'476	5195	5183	15
06.1	25.11.92	771'097 / 264'197	517'144 / 203'047	5148	5114	60
07.1	24.11.92	787'127 / 256'146	650'508 / 223'049	5188	5182	39
07.2	25.11.92	529'278 / 193'868	651'732 / 223'390	5131	5119	13
08.1	10.12.92	781'620 / 241'880	541'832 / 184'571	5050	5032	14
09.1	07.12.92	670'219 / 203'031	490'436 / 459'837	5059	5027	19
09.2	07.12.92	663'804 / 201'384	787'667 / 230'858	5036	5024	43
10.1	10.12.92	486'301 / 146'362	822'570 / 227'001	5043	5027	42
11.1	07.12.92	478'247 / 132'580	825'470 / 215'548	5056	5036	24
12.1	10.12.92	849'124 / 171'278	694'162 / 171'278	5051	5033	23
12.3	10.12.92	697'648 / 171'894	484'319 / 120'948	5035	5000	42
13.1	10.12.92	844'673 / 194'660	474'404 / 106'040	5033	4996	23
14.1	30.11.92	481'982 / 95'657	846'120 / 182'850	5142	5110	62
15.1	10.12.92	538'332 / 96'458	621'729 / 116'418	4979	4966	8
15.2	11.12.92	624'096 / 117'124	836'540 / 167'843	5033	5006	18
16.1	11.12.92	844'670 / 157'833	560'983 / 90'035	5036	4999	36
17.1	01.12.92	------- / -------	------- / -------	----	----	--
17.2	11.12.92	555'001 / 75'947	717'497 / 114'988	5032	5012	13
18.1	30.11.92	825'832 / 127'919	582'024 / 69'674	5144	5117	22
19.1	01.12.92	834'572 / 117'972	668'614 / 78'214	5166	5150	35
20.1	01.12.92	------- / -------	------- / -------	----	----	--
21.1	01.12.92	770'857 / 237'209	849'481 / 141'280	5168	5116	15
22.1	01.12.92	724'517 / 72'033	669'398 / 304'698	5138	5093	24
23.1	30.11.92	583'444 / 65'040	556'740 / 169'869	5145	5126	8
24.1	30.11.92	580'315 / 284'847	465'138 / 94'468	5140	5108	38

Table 9.2: Summary of flight altitudes (columns 5 and 6), dates of flights (column 2), coordinates of the beginning and end of the lines (columns 3 and 4) and number of bad records found after the reformatization procedure (column 7).

9.3 The computation of $\ddot{z}$

The first step of the gravity computation consists of filtering the raw beam and raw spring tension by means of a cascade of filters of different kinds. These filters are optionally running median, running mean, transverse and RC recursive filters. For the data presented here only RC filters were used.

The basic principle of a digital filter, developed by L. LaCoste (1967), for application in marine and airborne gravity computation, is given by the following differential equation :

$$\frac{dy}{dt}+\frac{1}{T}y=\frac{1}{T}x$$

where $y(t)$ is the filtered value, $x(t)$ is the unfiltered value and T is the time constant of the filter.

In digital form this equation can be written:

$$\frac{y_n-y_{n-1}}{t_n-t_{n-1}}+\frac{1}{T}y_n=\frac{1}{T}x_n$$

For $t_n-t_{n-1}=1$ sec , which was the sampling rate of our survey, this equation becomes:

$$y_n=\frac{T}{T+1}y_{n-1}+\frac{1}{T+1}x_n$$

Applying the filter with a time-constant, $T = 0.05$ sec, for example, will cause a time lag of 20 sec to occur. This kind of filter is known as one stage, one way, 20-sec filter (1,1,20). Applying the same filter over the already filtered data again, but in the opposite direction, will reverse the time lag, resulting in a total time lag of zero. In such a case one will speak about a one stage, two-way, 20-sec filter (1,2,20).

The filtered beam positions are then used for the computation of the beam velocities, by means of a seven point Lagrange differential operator. These values are multiplied by the so-called "K-factor", and then added to the filtered spring tension. The K-factor multiplication serves to transform the beam velocity into counter units which are the units of the spring tension. This sum is finally multiplied by the gravimeter factor to obtain a "g" value in mgal which, compared to the known gravity value at the airport, gives an instantaneous absolute raw g value at the measurement point (Figure 9.1).

In the second step the cross-coupling effects have to be removed from the measured vertical acceleration $\ddot{z}$. These values are directly computed by the system, taking into account the horizontal accelerations, and recorded once every ten seconds. Because the sampling rate of the gravimeter was set at one second it was necessary to re-sample the cross-coupling values. For this we chose to assign the value of the ten second window to the middle of it (e.g. for t = 5 sec the value of x was that of the window t = 1 sec to t = 10 sec, for t = 15 sec the value of x was that of the window t = 11 sec to t = 20 sec) and to interpolate the seconds in between, by means of a spline function. This procedure has the advantage avoiding steps introduced by the constant value, assigned to all the time windows.

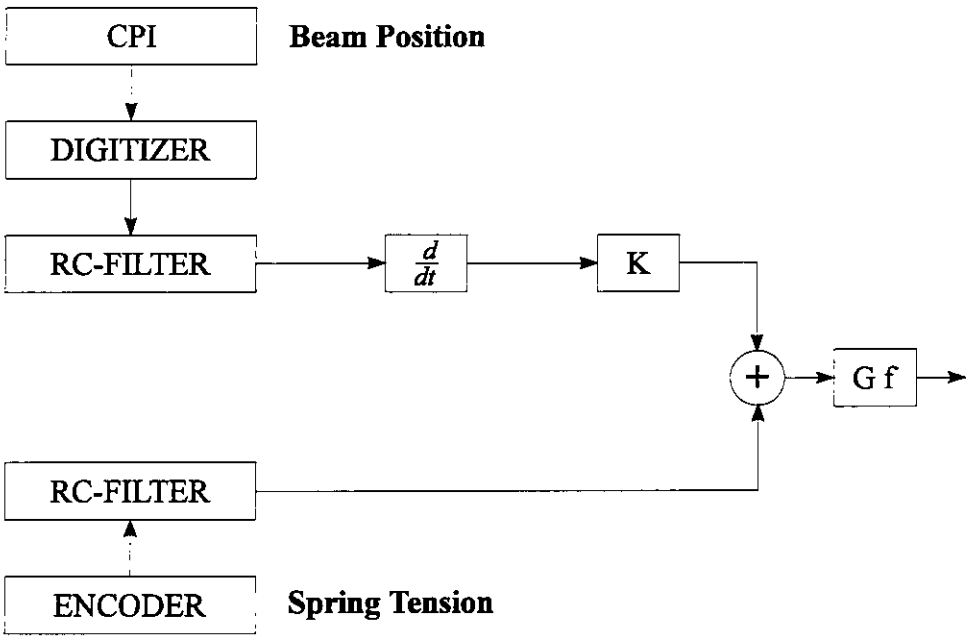

Figure 9.1: Flow chart showing the procedure used for the computation of g.

The third step consists of computing the Eötvös accelerations (vertical component of the Coriolis acceleration) and removing it from the measured value z. For this computation the horizontal position of the aircraft, flight altitude and distance to Earth center are used. The Eötvös effect was computed by means of the formula given by Harlan (1962) which is the best adapted one for airborne gravimetry. In that case the correction is given by the expression:

$$\delta g_{\text{Eötvös}} = (1+\frac{h}{a})\,(2\omega\, v \cos\Phi \sin\alpha + \frac{v^2}{r}) - f\frac{v^2}{a}(1-\cos^2\Phi)\,(3-2\sin^2\alpha)$$

with

h : Altitude above the ellipsoid
a : Earth semi-major axis
f : Earth flattening
ω : Earth angular velocity
v : Ground velocity of the aircraft
Φ : Latitude
α : Flight azimuth
r : Radial distance to geocenter

The horizontal velocity was calculated by means of the same differentiation operator as that used for gravity computations. Here also, some filtering procedures were necessary. The filter's parameters were similar to those used in other procedures.

Parallel to this procedure, the GPS data containing the time of measurement, the three coordinates of the aircraft for both the rear and front antennae, the flight azimuth and the distance to the Earth center were used together with pitch and roll angles to compute the vertical accel-

erations of the aircraft. During this procedure the same kinds of filters and the same filtering parameters as those employed for the raw spring tension and the raw beam position were used.

9.4 Computation of the true vertical position of the gravimeter

In order to be able to correct the measured vertical accelerations for those produced by the movements of the aircraft, it is necessary to have very precise information about the three-dimensional movements of the aircraft.

For this purpose, the aircraft was equipped with two GPS antennae and receivers. Both antennae were placed on the roof of the cabin, one in front of the gravimeter and the second behind it. Because two points are not enough to compute a three- dimensional movement an attitude gyroscope was mounted on the frame of the platform. This instrument produced two analogue voltages, proportional to the pitch and roll angles of the aircraft. The accuracy of these last data are in the order of one half of a degree. Combining the information of the two antennae and of the attitude gyroscope it was possible to compute the true vertical position of the gravimeter's sensor according to the procedure described in Appendix A.

The vertical accelerations of the aircraft were then computed by double differentiation of the true vertical positions of the gravimeter. Some filtering procedures (on positions and velocities) were also necessary before and between these two differentiations. It is worth noting that this filtering must be used with great care because the choice of the parameters is not obvious and the criterion for their choice often subjective.

9.5 Comparison between results obtained with one and two antennae

For these comparisons, vertical accelerations were first computed along lines 14.1 and 22.1, by means of the true vertical positions of the gravimeter and then with the positions of the rear and front antennae alone.

Each set of data was filtered with a three stage, RC, back filter of 5 sec., 10 sec., 20 sec. and 30 seconds time constant.

Finally, the differences between accelerations computed at the meter position and rear antenna, respectively front antenna, were made and the RMS of the differences calculated.

The results of these differences are graphically presented in figures 9.2 to 9.5 for line 14.1 and figures 9.6 to 9.9 for line 22.1.

Table 9.3 summarizes the RMS results.

	5 sec.	10 sec.	20 sec.	30 sec.	Line
RMS Front- Grav.	2.32	0.75	0.18	0.08	14.1
RMS Rear - Grav.	10.12	3.28	0.71	0.30	14.1
RMS Front- Grav.	2.02	0.65	0.19	0.10	22.1
RMS Rear - Grav.	8.16	2.57	0.79	0.34	22.1

Table 9.3: Summary of the RMS of the differences between vertical accelerations obtained with one and two antennae and computed with different RC filter's time constants. The values are in [mgal].

It is clear from this analysis that the use of two antennae and pitch and roll information improves the results, especially in the high frequencies (short wave-length). However, for filtering of around 20 seconds RC time-constant, which is the industrial standard, the use of the front antenna alone (even if slightly shifted with regard to the gravimeter sensor) seems to produce results with the quality required by an airborne survey.

9.6 The final choice of the filter's parameters

For practical reasons we chose to use only three stage, two-way, RC filters because this kind of recursive filters minimize the quantity of data to be eliminated at the end of the lines. The only parameter which we had to chose was the time-constant of the filter. For this we filtered the GPS derived vertical accelerations and the raw beam and raw spring tension with the same parameters. Then we corrected the z values for Eötvös accelerations and finally, graphically compared the two sets of data for the same lines as those analyzed in chapter 9.5. The results of these comparisons are presented in figures 9.10 to 9.12 for line 14.1, and figures 9.13 to 9.15 for line 22.1.

It is immediately clear that the 10 second time-constant is too short for both lines. On line 22.1 $T = 20$ sec. seems to be good enough but a quick look at line 14.1 shows clearly that a longer T is necessary for eliminating the remaining very short oscillations.

On the other hand longer time-constants than 30 sec. would reduce the number of data available for further processing too much. Therefore, **we decided to process and produce the final results with three stage, two-way, RC filters with a time constant of 30 seconds.**

A last check concerning the synchronization of the GPS and gravimeter data was also performed at this stage of processing. It was done by introducing the two vertical accelerations computed from the gravimeter and GPS into a cross-correlation procedure. Where necessary both times were re-synchronized by adding a time dependent shift into the gravimeter time. This computation was also employed for determining the best possible kind of filters and their parameters.

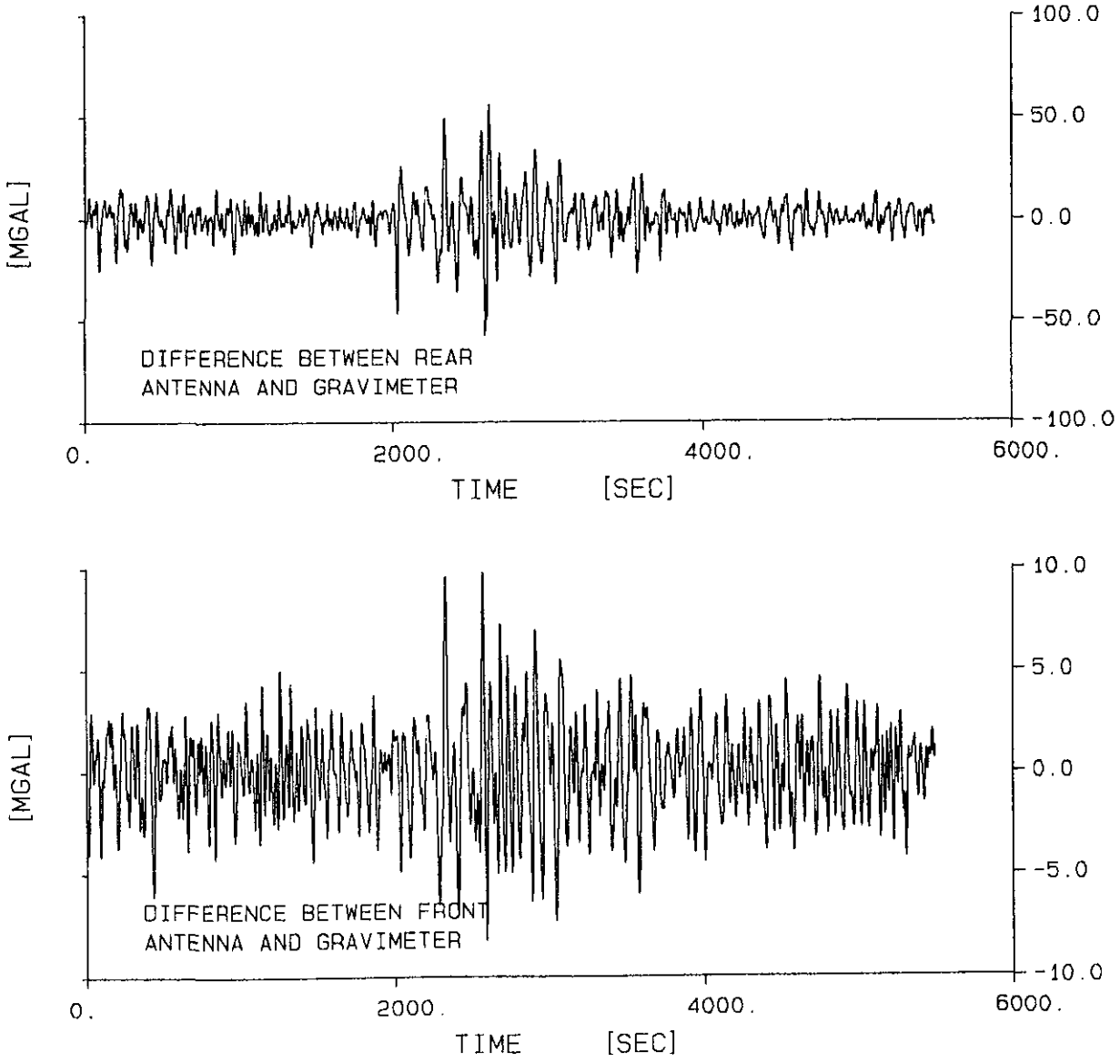

LINE NUMBER 14.1

FILTER PARAMETERS

ALT	VV	VAM	
0	0	0	MEDIAN
0	0	0	MEAN
0	0	-3	N R-C
0	0	5	T R-C

RMS OF VERT. ACC. DIFFERENCES

FRONT ANTENNA-GRAVIMETER 2.318
REAR ANTENNA-GRAVIMETER 10.121

Figure 9.2 : Differences between vertical accelerations computed with one antenna and with two antennae at the sensor location for line 14.1.
RC-filter time-constant = 5 seconds
Lower diagram : Front antenna differences.
Upper diagram : Rear antenna differences.

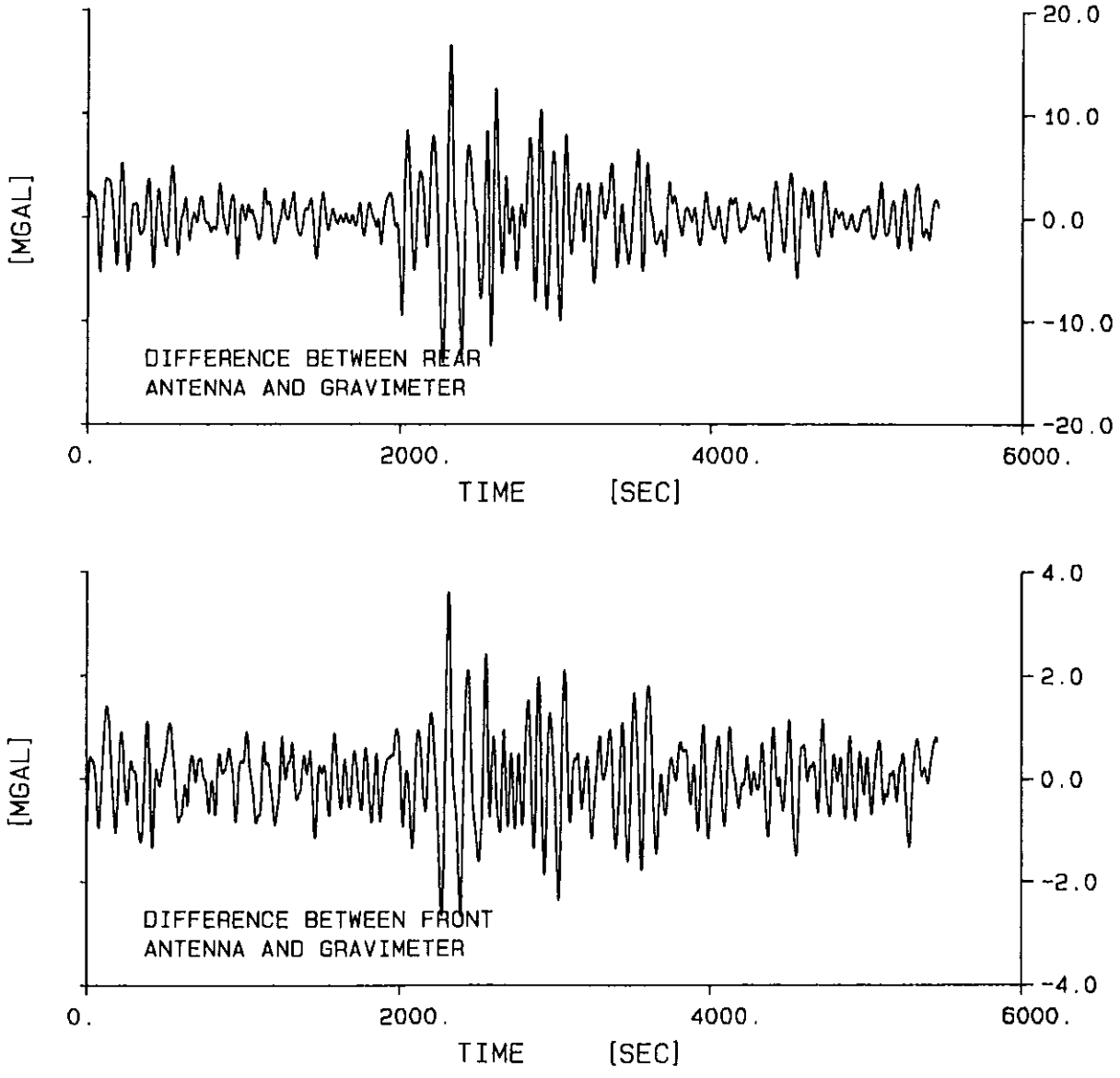

LINE NUMBER 14.1

FILTER PARAMETERS

ALT	VV	VAM	
0	0	0	MEDIAN
0	0	0	MEAN
0	0	-3	N R-C
0	0	10	T R-C

RMS OF VERT. ACC. DIFFERENCES

FRONT ANTENNA-GRAVIMETER 0.752
REAR ANTENNA-GRAVIMETER 3.275

Figure 9.3 : Differences between vertical accelerations computed with one antenna and with two antennas at the sensor location for line 14.1.
RC-filter time-constant = 10 seconds
Lower diagram : Differences for front antenna.
Upper diagram : Differences for rear antenna.

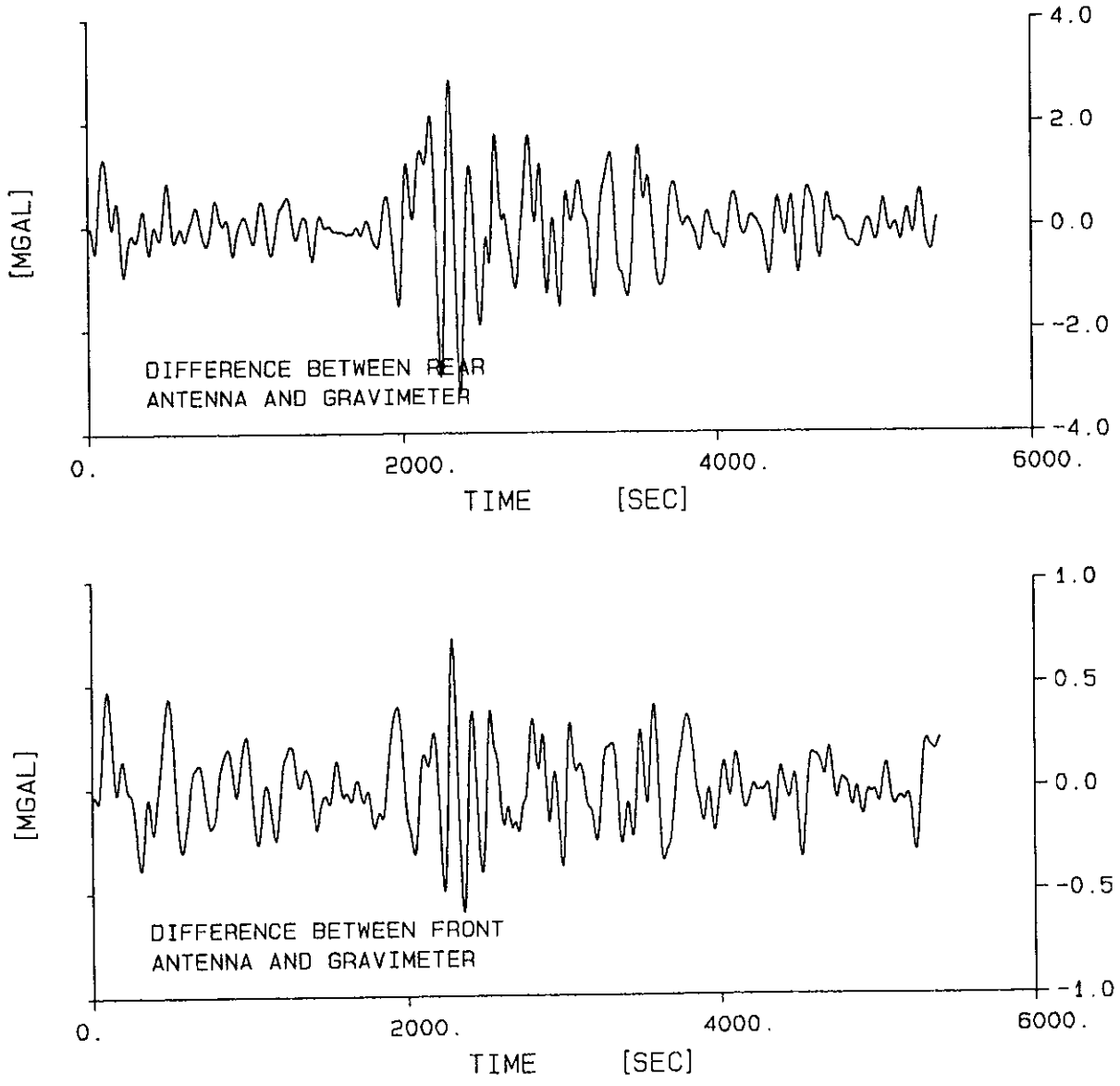

LINE NUMBER 14.1

FILTER PARAMETERS

ALT	VV	VAM	
0	0	0	MEDIAN
0	0	0	MEAN
0	0	-3	N R-C
0	0	20	T R-C

RMS OF VERT. ACC. DIFFERENCES

FRONT ANTENNA-GRAVIMETER 0.183
REAR ANTENNA-GRAVIMETER 0.711

Figure 9.4 : Differences between vertical accelerations computed with one antenna and with two antennae at the sensor location for line 14.1.
RC-filter time-constant = 20 seconds
Lower diagram : Differences for front antenna.
Upper diagram : Differences for rear antenna.

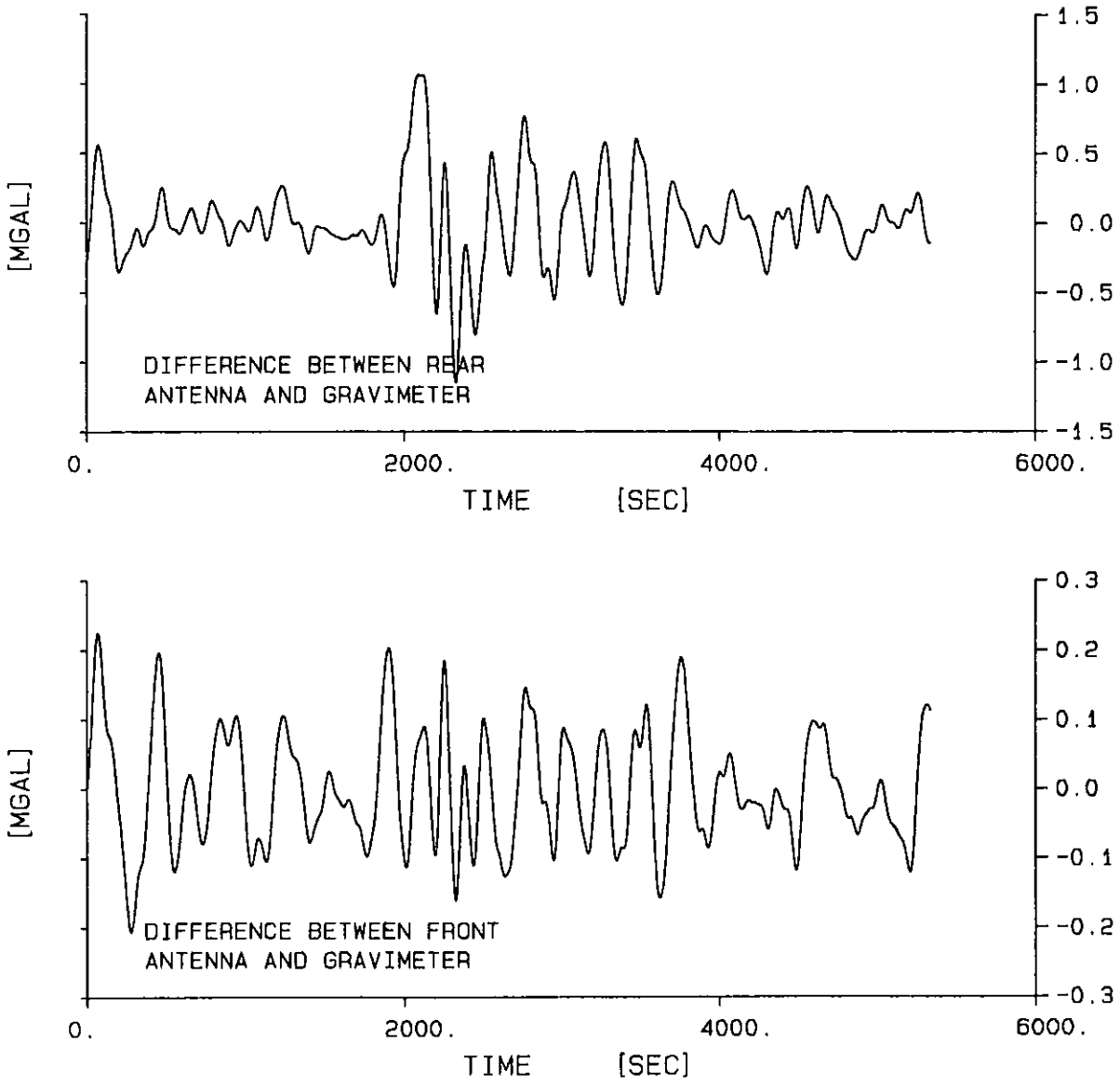

LINE NUMBER 14.1

FILTER PARAMETERS

ALT	VV	VAM	
0	0	0	MEDIAN
0	0	0	MEAN
0	0	-3	N R-C
0	0	30	T R-C

RMS OF VERT. ACC. DIFFERENCES

FRONT ANTENNA-GRAVIMETER 0.083
REAR ANTENNA-GRAVIMETER 0.303

Figure 9.5 : Differences between vertical accelerations computed with one antenna and with two antennae at the sensor location for line 14.1.
RC-filter time-constant = 30 seconds
Lower diagram : Differences for front antenna.
Upper diagram : Differences for rear antenna.

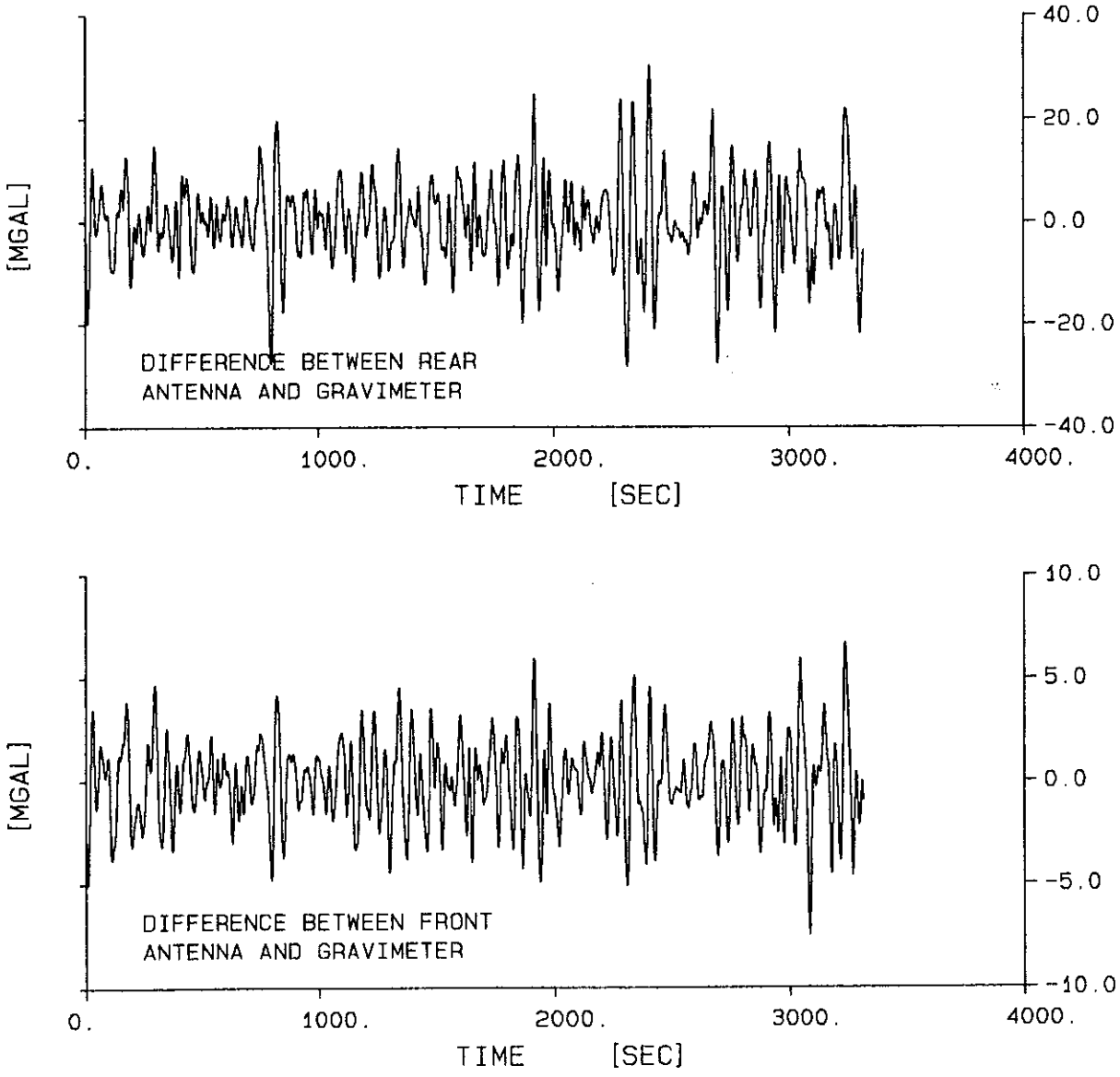

LINE NUMBER 22.1

FILTER PARAMETERS

ALT	VV	VAM	
0	0	0	MEDIAN
0	0	0	MEAN
0	0	-3	N R-C
0	0	5	T R-C

RMS OF VERT. ACC. DIFFERENCES

FRONT ANTENNA-GRAVIMETER 2.019
REAR ANTENNA-GRAVIMETER 8.157

Figure 9.6 : Differences between vertical accelerations computed with one antenna and with two antennae at the sensor location for line 22.1.
RC-filter time-constant = 5 seconds
Lower diagram : Differences for front antenna.
Upper diagram : Differences for rear antenna.

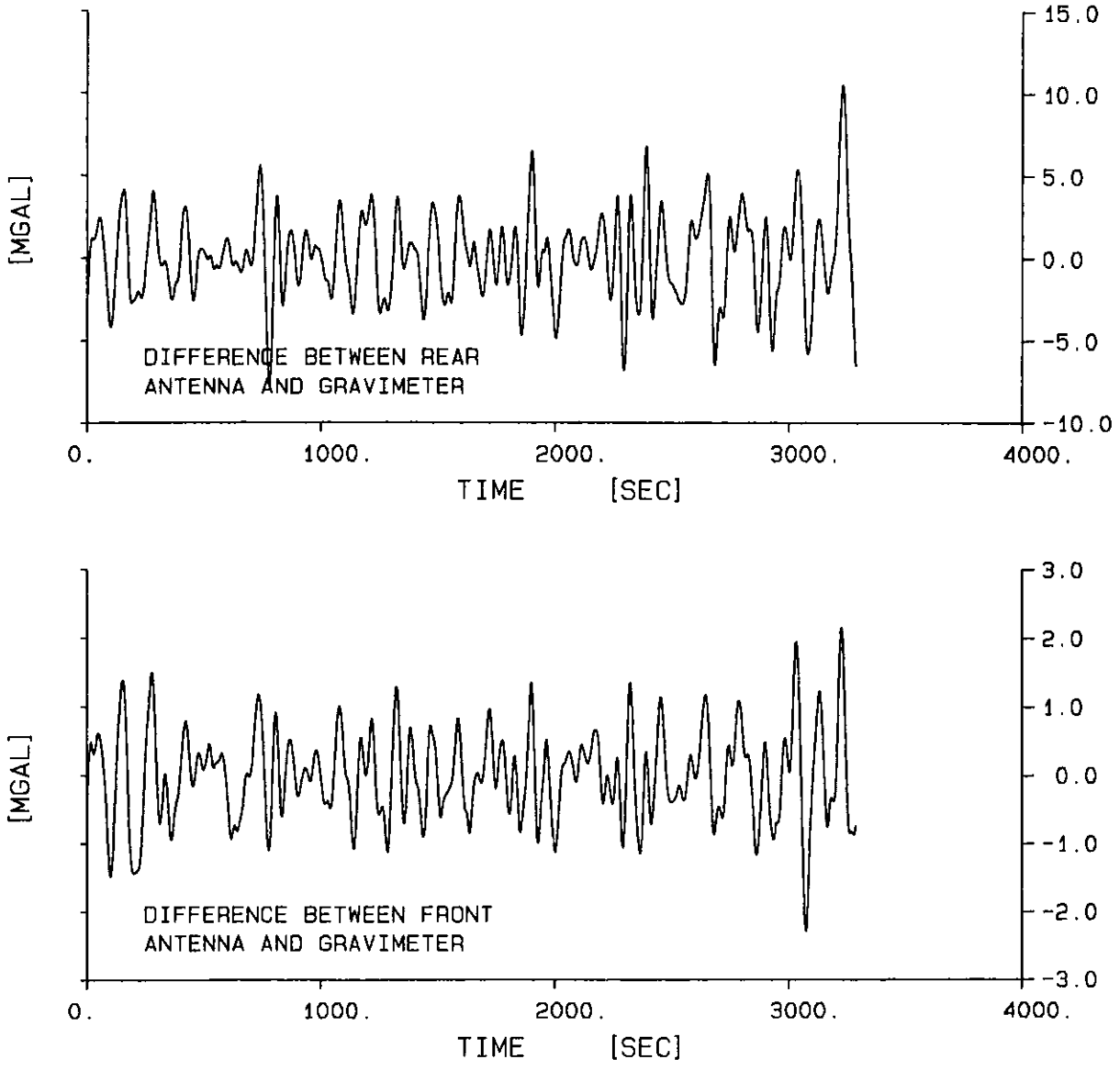

LINE NUMBER 22.1

FILTER PARAMETERS

ALT	VV	VAM	
0	0	0	MEDIAN
0	0	0	MEAN
0	0	-3	N R-C
0	0	10	T R-C

RMS OF VERT. ACC. DIFFERENCES

FRONT ANTENNA-GRAVIMETER 0.654
REAR ANTENNA-GRAVIMETER 2.568

Figure 9.7 : Differences between vertical accelerations computed with one antenna and with two antennae at the sensor location for line 22.1.
RC-filter time-constant = 10 seconds
Lower diagram : Differences for front antenna.
Upper diagram : Differences for rear antenna.

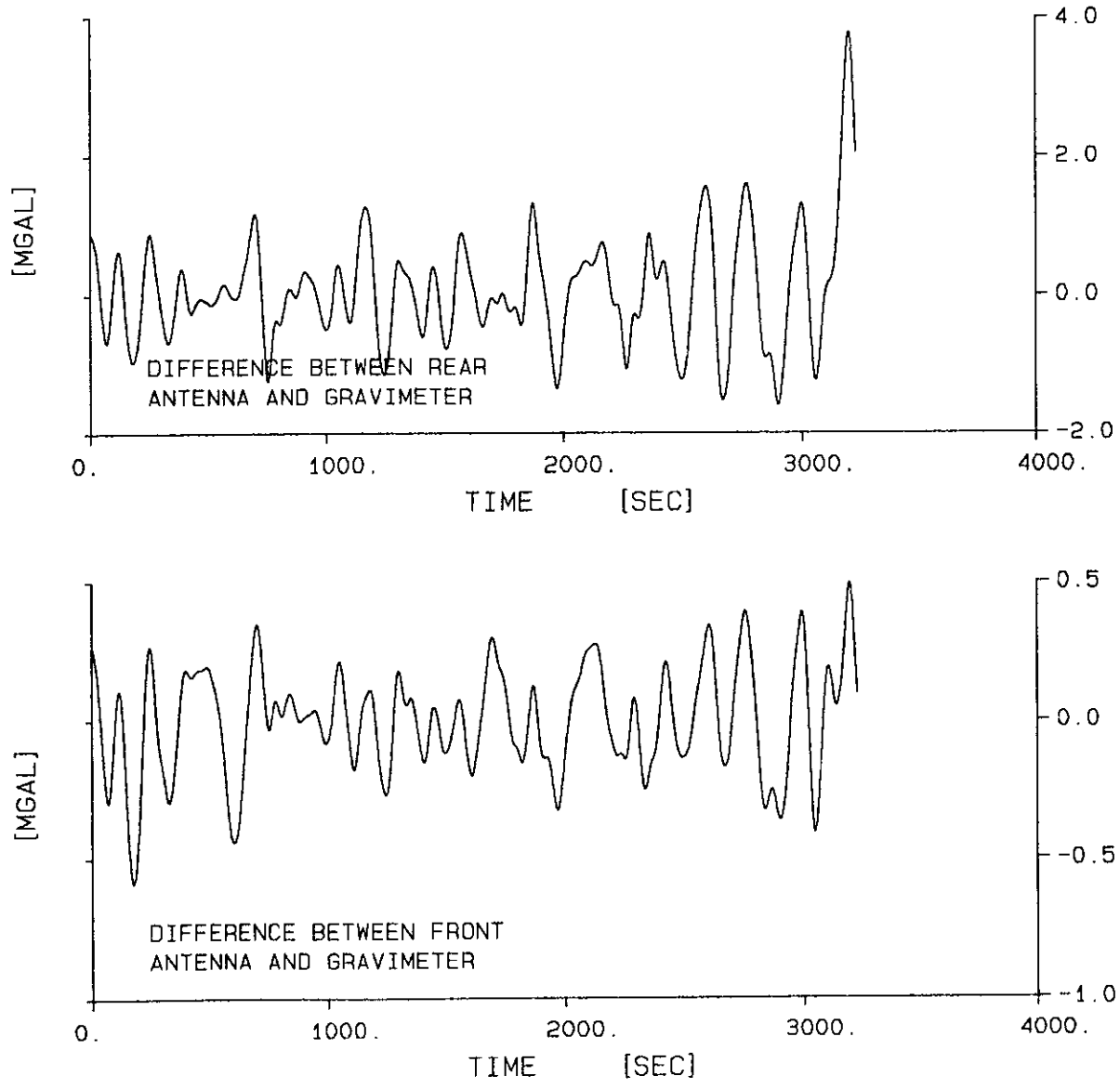

LINE NUMBER 22.1

FILTER PARAMETERS

ALT	VV	VAM	
0	0	0	MEDIAN
0	0	0	MEAN
0	0	-3	N R-C
0	0	20	T R-C

RMS OF VERT. ACC. DIFFERENCES

FRONT ANTENNA-GRAVIMETER 0.193
REAR ANTENNA-GRAVIMETER 0.789

Figure 9.8 : Differences between vertical accelerations computed with one antenna and with two antennae at the sensor location for line 22.1.
RC-filter time-constant = 20 seconds
Lower diagram : Differences for front antenna.
Upper diagram : Differences for rear antenna.

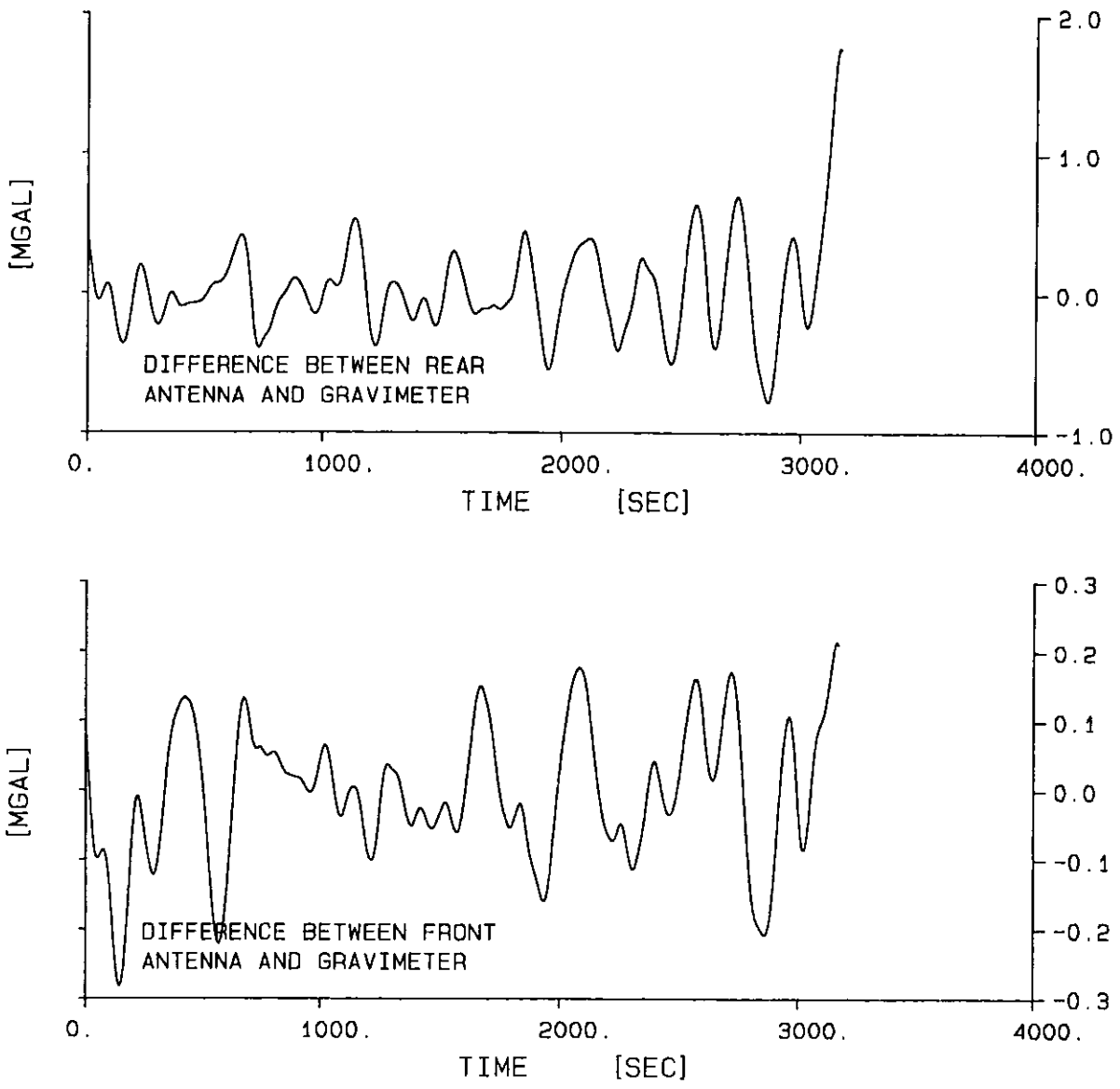

LINE NUMBER 22.1

FILTER PARAMETERS

ALT	VV	VAM	
0	0	0	MEDIAN
0	0	0	MEAN
0	0	-3	N R-C
0	0	30	T R-C

RMS OF VERT. ACC. DIFFERENCES

FRONT ANTENNA-GRAVIMETER 0.097
REAR ANTENNA-GRAVIMETER 0.335

Figure 9.9 : Differences between vertical accelerations computed with one antenna and with two antennae at the sensor location for line 22.1.
RC-filter time-constant = 30 seconds
Lower diagram : Differences for front antenna.
Upper diagram : Differences for rear antenna.

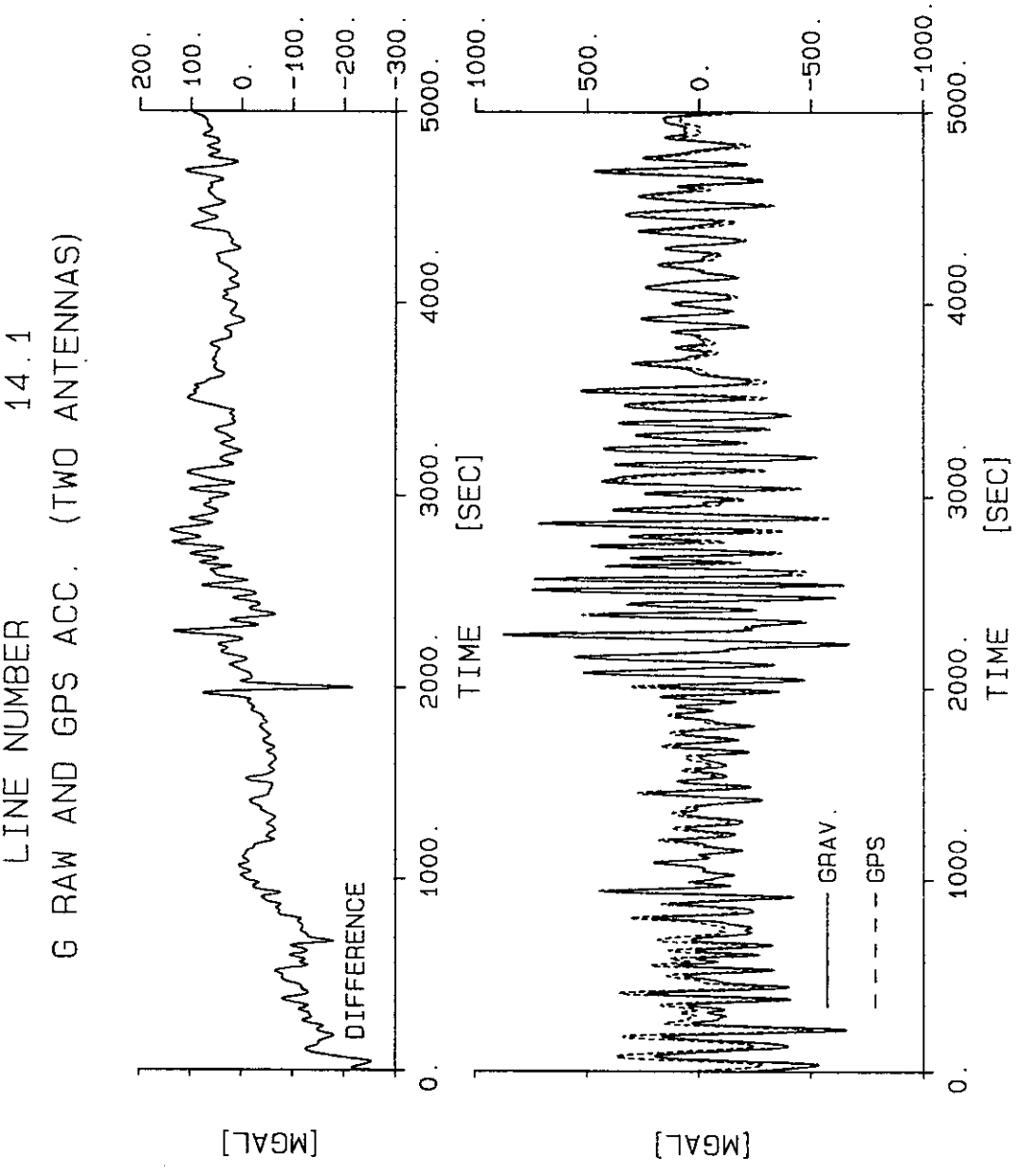

Figure 9.10: Lower diagram : Vertical accelerations deduced from gravimeter data (dotted line) and two-antenna GPS data (continuous line) computed with a RC-filter time-constant of 10 seconds along line 14.1
Upper diagram : differences of the two sets of accelerations.

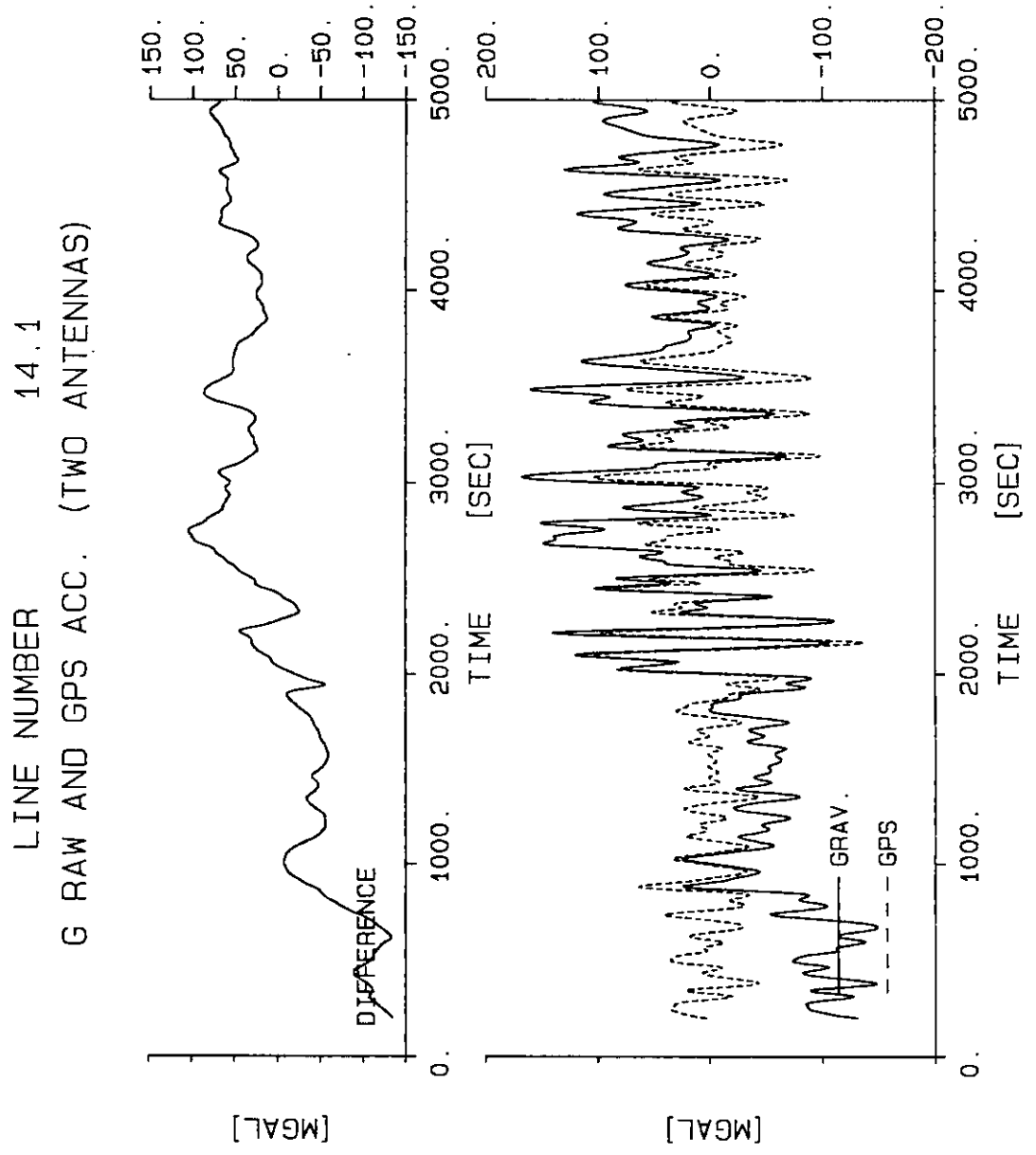

Figure 9.11: Lower diagram : Vertical accelerations deduced from gravimeter data (dotted line) and two-antenna GPS data (continuous line) computed with a RC-filter time-constant of 20 seconds along line 14.1
Upper diagram : differences of the two sets of accelerations.

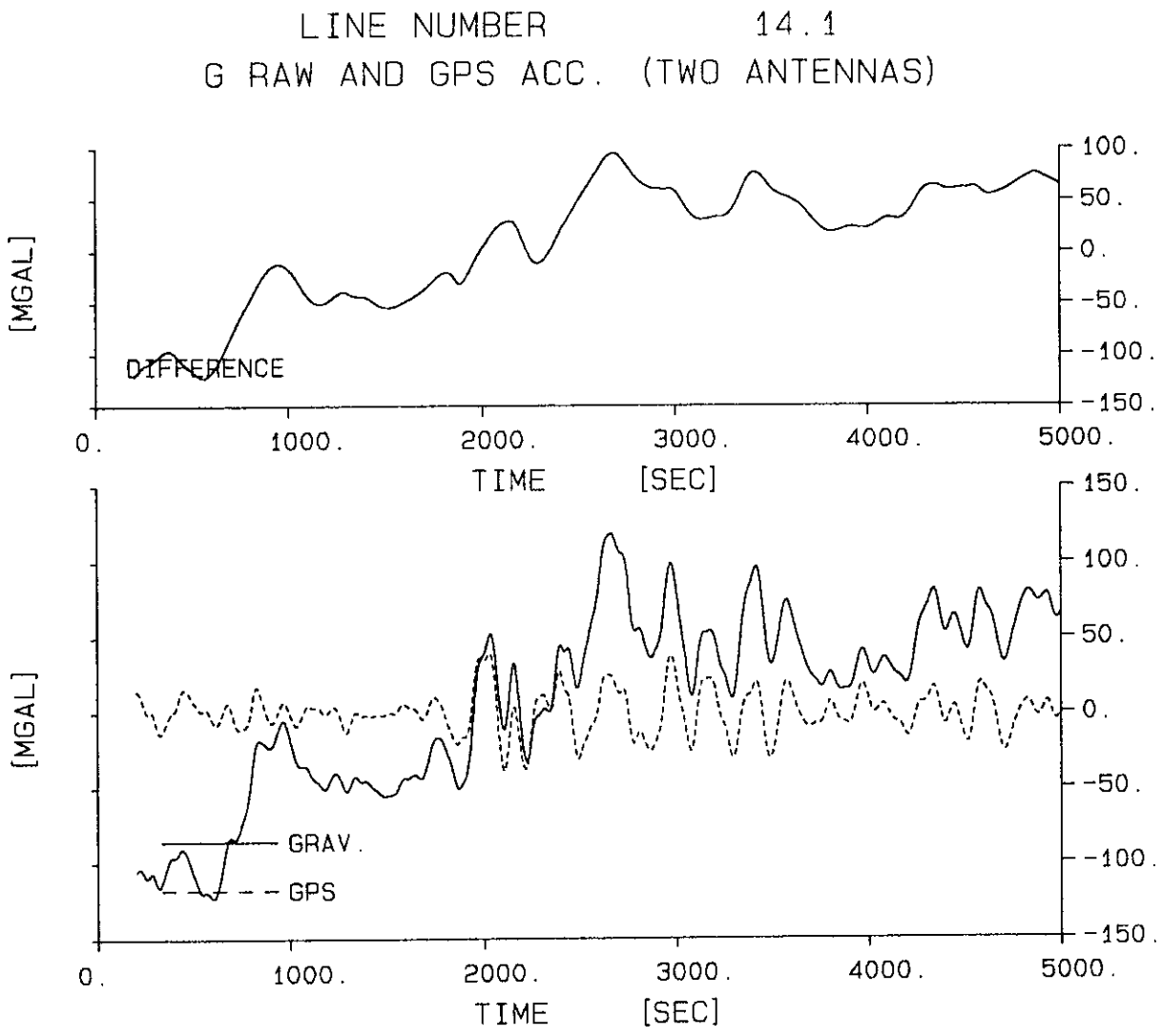

RB	RS	ALT	VV	VA
0	0	0	0	0
0	0	0	0	0
-3	-3	0	0	-3
30	30	0	0	30
0	0	0	0	0

GPS TIME SHIFT : 0 [SEC]
ISENS = 1

Figure 9.12: Lower diagram : Vertical accelerations deduced from gravimeter data (dotted line) and two-antenna GPS data (continuous line) computed with a RC-filter time-constant of 30 seconds along line 14.1
Upper diagram : differences of the two sets of accelerations.

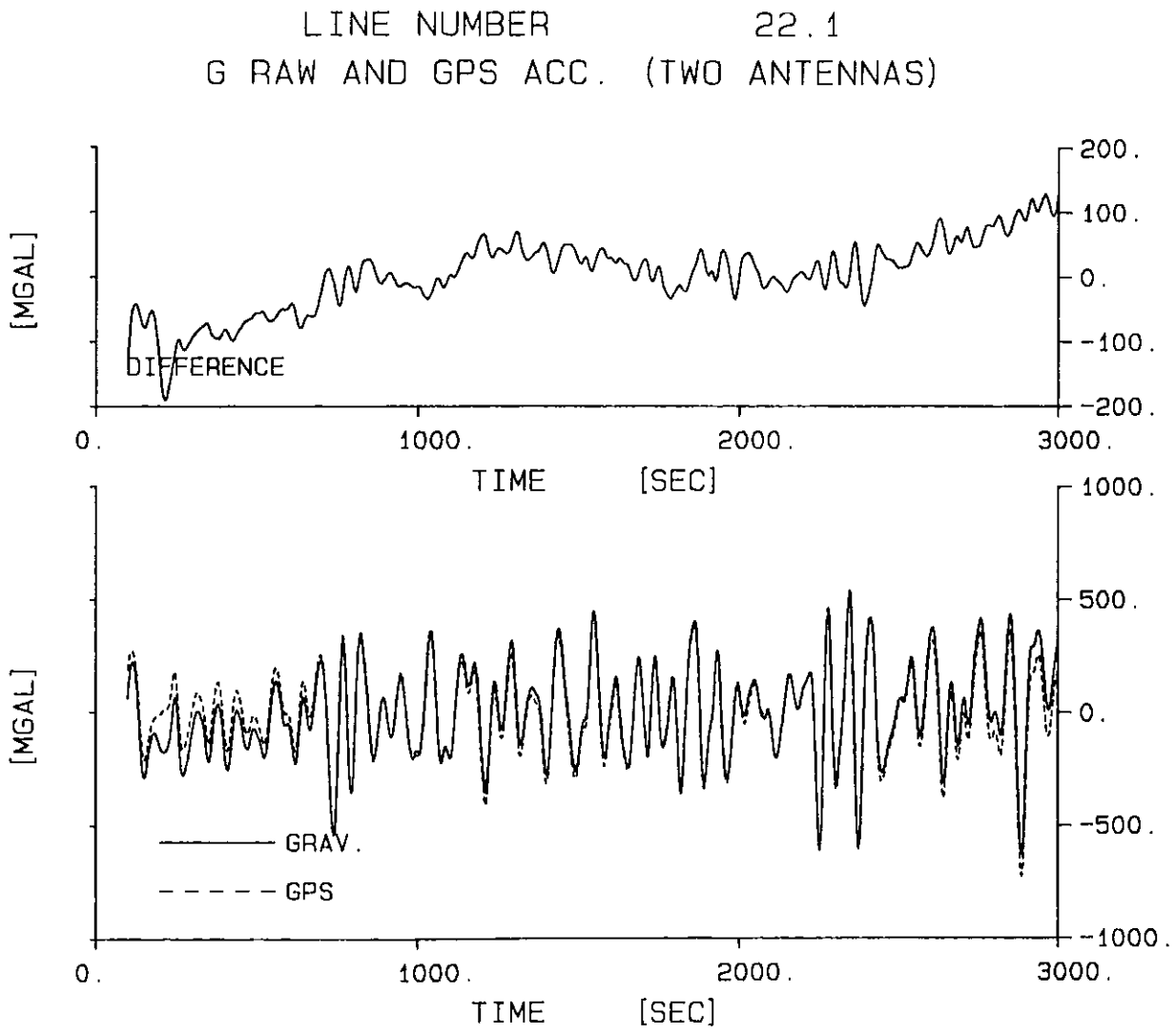

RB	RS	ALT	VV	VA
0	0	0	0	0
0	0	0	0	0
-3	-3	0	0	-3
10	10	0	0	10
0	0	0	0	0

GPS TIME SHIFT : 0 [SEC]
ISENS = 1

Figure 9.13: Lower diagram : Vertical accelerations deduced from gravimeter data (dotted line) and two-antenna GPS data (continuous line) computed with a RC-filter time-constant of 10 seconds along line 22.1
Upper diagram : differences of the two sets of accelerations.

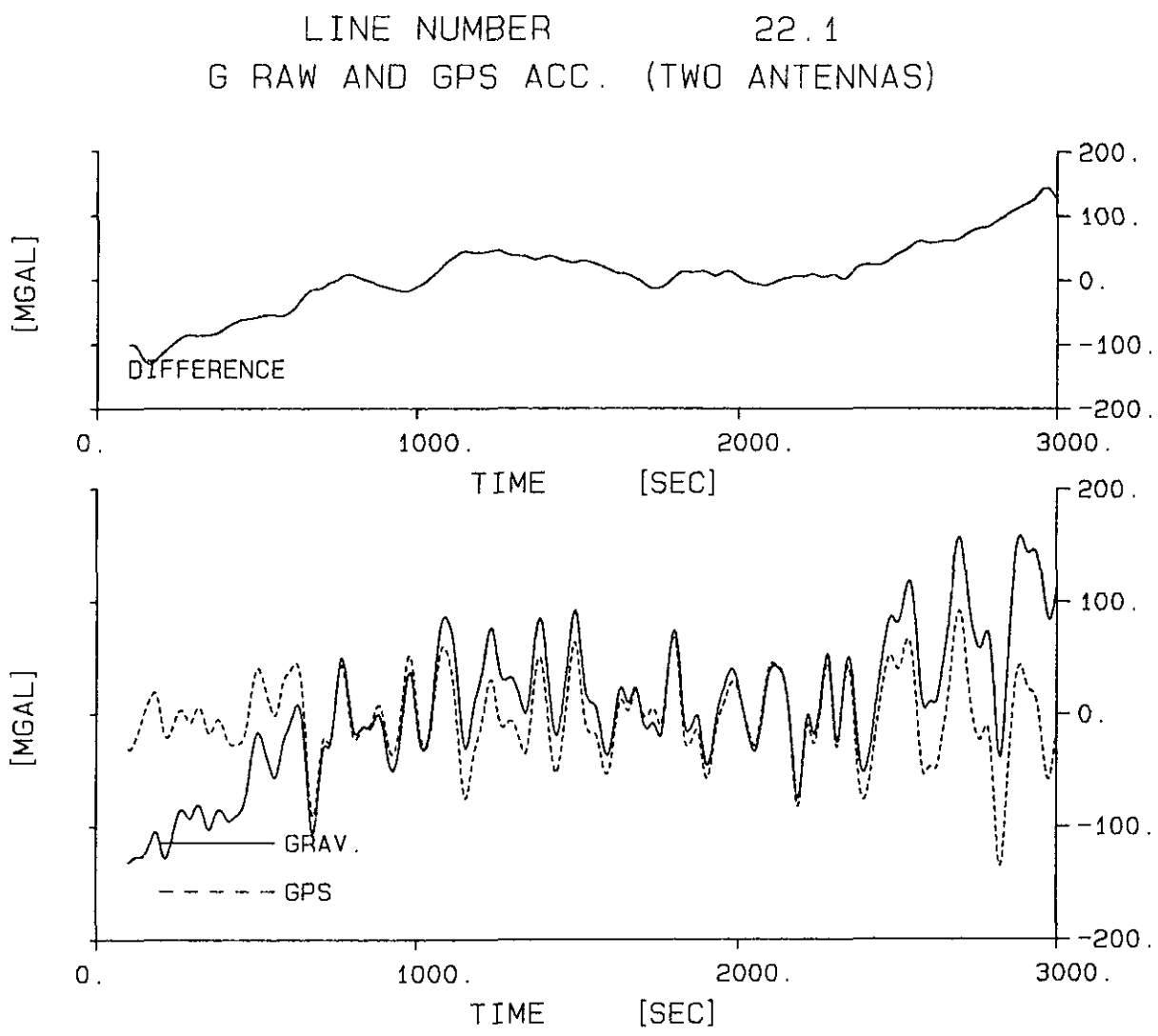

RB	RS	ALT	VV	VA
0	0	0	0	0
0	0	0	0	0
-3	-3	0	0	-3
20	20	0	0	20
0	0	0	0	0

GPS TIME SHIFT : 0 [SEC]
ISENS = 1

Figure 9.14: Lower diagram : Vertical accelerations deduced from gravimeter data (dotted line) and two-antenna GPS data (continuous line) computed with a RC-filter time-constant of **20** seconds along line 22.1
Upper diagram : differences of the two sets of accelerations.

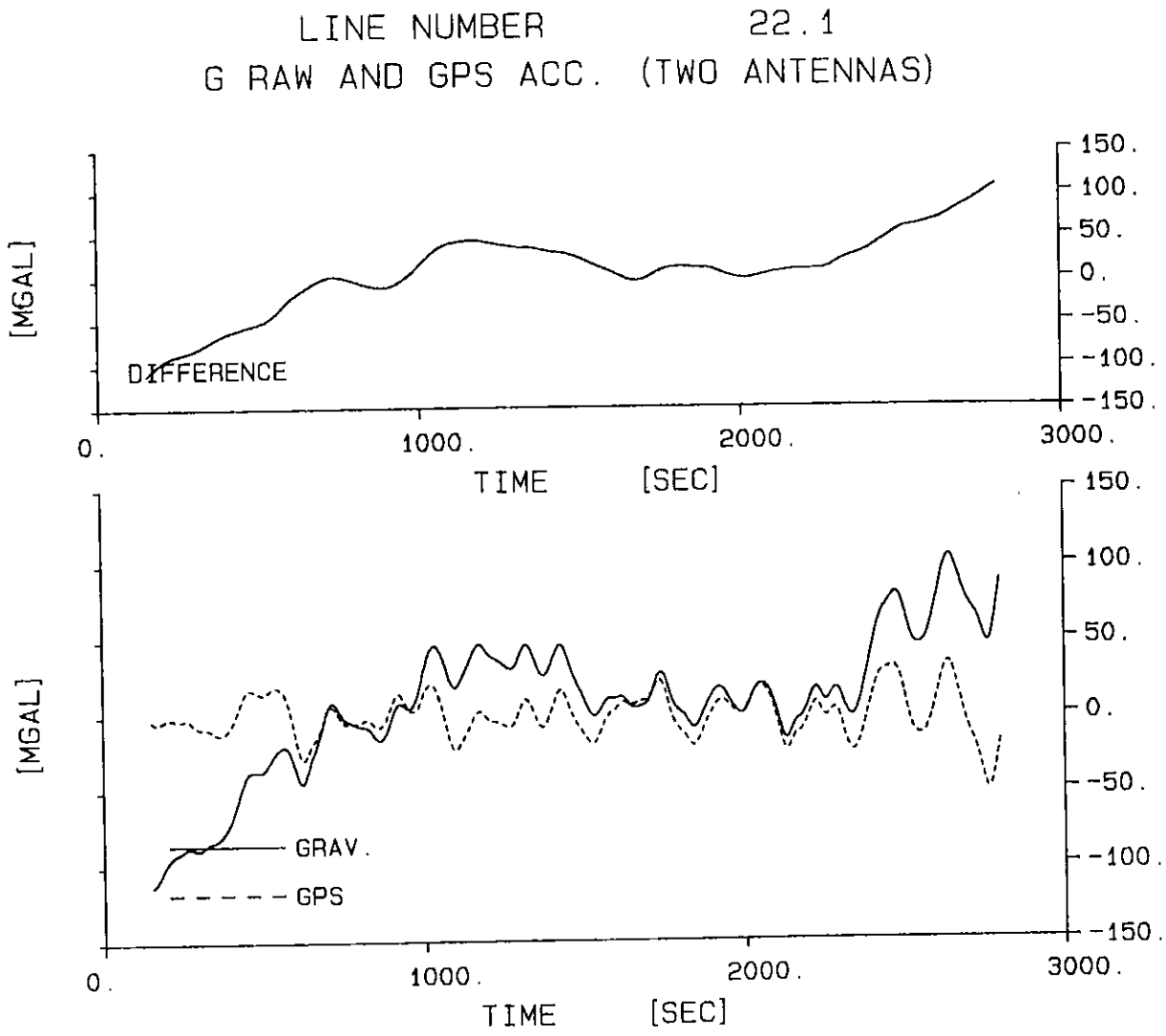

RB	RS	ALT	VV	VA
0	0	0	0	0
0	0	0	0	0
-3	-3	0	0	-3
30	30	0	0	30
0	0	0	0	0

GPS TIME SHIFT : 0 [SEC]
ISENS = 1

Figure 9.15: Lower diagram : Vertical accelerations deduced from gravimeter data (dotted line) and two-antenna GPS data (continuous line) computed with a RC-filter time-constant of 30 seconds along line 22.1
Upper diagram : differences of the two sets of accelerations.

9.7 The final computation of g and Free-Air anomaly

Once all these parameters have been determined, the GPS data (coordinates, flight azimuth, distance to the center of the Earth), raw beam and raw spring tension data and the cross coupling corrections were introduced into another processing stage. During this process the vertical accelerations of the aircraft as well as the filtered value of g were recomputed and the cross-coupling corrections applied. It also computed the Eötvös effects and subtracted them from the g values. Finally, the Free-Air anomaly was computed for every point by subtracting the theoretical value of g at the measurement point from the measured one.

In our particular case, the program performing these procedures created two different data files. One containing the sample number, the coordinates of the measurements, the corresponding g value and the Free-Air anomaly. The second containing only the sample number and the coordinates. In fact, this second file was created only once, at the beginning of the analysis.

9.8 The topographic corrections

Because the Free-Air anomalies are strongly influenced by the effects of the topographic masses, they have to be corrected, before they can be used for interpretation or compared with ground data. In this case, the anomalies are called full Bouguer anomalies.

The topographic effect was computed by numerical integration using different terrain models. The first model consists of altitude cells of 250 m by 250 m covering all of Switzerland and extending as far as 100 km into Austria, France, Germany and Italy. This model was used for the topographic corrections around the measurement point from zero to 15 km. The calculation was performed by the line-of-mass formula. In order to reduce the computing time, the original cells were combined to form larger cells of 1 km by 1 km. This size was determined after calculations were performed to find the largest possible mesh size of the topographic cells which give a reasonable accuracy. For these calculations we used a synthetic topography, formed by a cylinder with a 5 km radius, 5000 m thickness and a density of 2670 kg/m^3. This topography was approximated by vertical prisms with square cross-sections of different sizes. The computation was performed on two different locations of the computing point (CC1 and CC2 of Figure 9.16) and then compared with the true value.

For mesh sizes, varying from 250 m to 10 km, the differences extended from 0.02 mgal to 0.41 mgal (Figure 9.16). However, even though the computation, which was made with the largest mesh size, gave acceptable results, we decided to use a size of 1000 m which, in our opinion, is a good compromise between reasonable computing time and good definition of the real topography.

The second model is formed by altitude cells of 3' by 3', covering almost all of continental Europe. Here too the computation is done with the line-of-mass formula.

The topographic corrections were performed on the second data file because only these data are coordinate dependent. This method allows a single computation of the topographic corrections, even if further processing is necessary for the computation of the full Bouguer anomalies (e.g. different filtering). The last procedure consists of subtracting the topographic effects from the Free-Air anomaly; this gives the full Bouguer anomaly. It is worth noting that the Bouguer anomaly can also be filtered with the same filters as applied to GPS, gravimeter data and Free-Air anomalies.

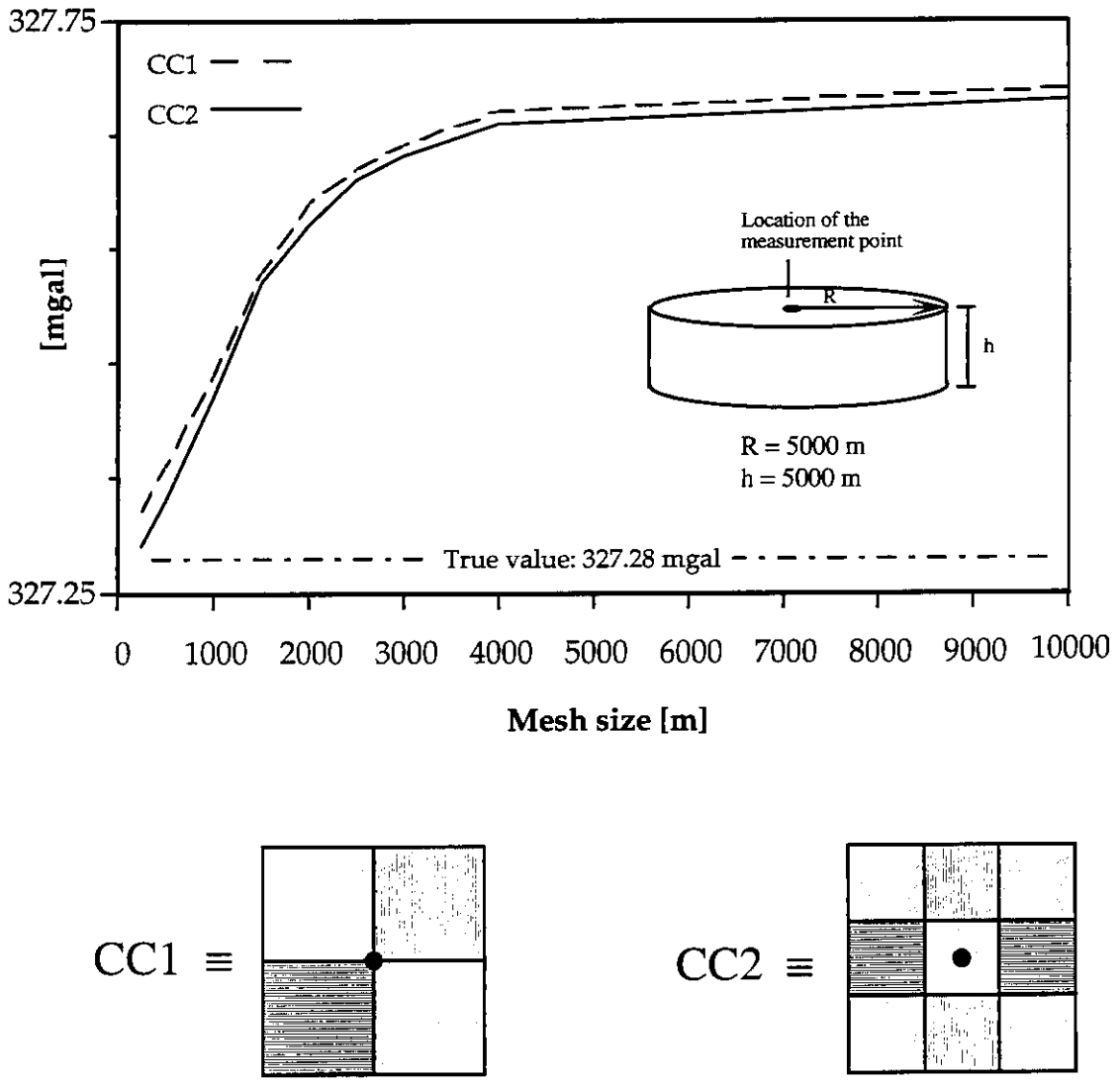

Figure 9.16: Diagram showing the results of the determination of the largest possible mesh size usable for topographic correction up to 15 km.

9.9 The reduction of the Bouguer anomaly to a constant altitude.

For navigation, the automatic pilot uses the altitude given by the barometric altimeter. During a single day of measurements or along a single line, the true altitude of the aircraft does not vary much; a few meters at most. This is unfortunately not the case for lines flown on different days, particularly if the atmospheric conditions are different. This was the case during the Swiss survey, especially because of frequent temperature inversions, inducing heavy fog.

In order to produce a gravity anomaly map computed at constant altitude, it was necessary to apply a correction to the data computed at flight altitude. In order to do this, the vertical gradient has to be known for each measurement point. In a region with very strong anomalies, like Switzerland, the real vertical gradient differs significantly from the normal gradient given by the WGS84 formula. For the evaluation of this real gradient we used the EGT gravity data for a first trial. These data were interpolated to produce a quadratic grid with a mesh size of 5000 meters.

From this grid two anomaly fields were computed for 5200 m and 4800m by means of a Fast Fourier Transform algorithm.

$$\Delta g(x, y, z) = \boldsymbol{F}^{-1}\left\{ e^{-fz}\boldsymbol{F}\{ g(x, y, 0)\} \right\}$$

where $\boldsymbol{F}$ and $\boldsymbol{F}^{-1}$ are the direct and inverse Fourier Transforms.

The mean vertical gradient was then approximated by :

$$\frac{dg}{dz} = \frac{\Delta g_{5200} - \Delta g_{4800}}{400}$$

The gradient obtained by these computations is presented in Figures 9.17, and an example of the field upward-continued at 5000 m in Figure 9.18. The results of the upward continuation are not satisfactory, when compared with the anomaly map computed at flight altitude (Figure 9.19). All the anomalies are situated at their right locations but their amplitudes are obviously to small (up to three times). Consequently the vertical gradient, computed with this method, is not realistic. This fact can be easily explained, as in the upward continuation operator, the exponent of the exponential acts as an attenuation factor proportional to the wave number of the anomaly ($1/\lambda$). The long and very long wave-lengths are almost not attenuated. If the zone considered, is too small to contain all the long wave-length components, the prolongation will not contain their contributions and their amplitudes will be strongly reduced or even eliminated.

In order to obtain a better picture of the two-dimensional vertical gradient at 5100 m, we first produced a Bouguer anomaly map at flight altitude following the procedure described in chapter 9.1 to 9.7 and calculated the difference with the ground values. The mean gradient was computed by dividing their difference by the altitude difference.

The results of this computation is shown in Figure 9.20.

From a theoretical point of view, this procedure is certainly disputable but practically, the error introduced can be estimated as small enough to be tolerated in the frame of such a survey.

Supposing that the largest altitude difference between the measurement lines and the nominal altitude is 100 m and we tolerate an inaccuracy on the upward-continued anomaly of say, some tenths of mgal, then the acceptable inaccuracy of the gradient becomes 0.001 mgal/m. Because the difference between ground and flight altitude is large (Δh = 5000 m), the difference between the anomaly on the irregular surface and the horizontal plane can be tolerated to be in the order of 5 mgal. This is certainly the case for the Swiss survey.

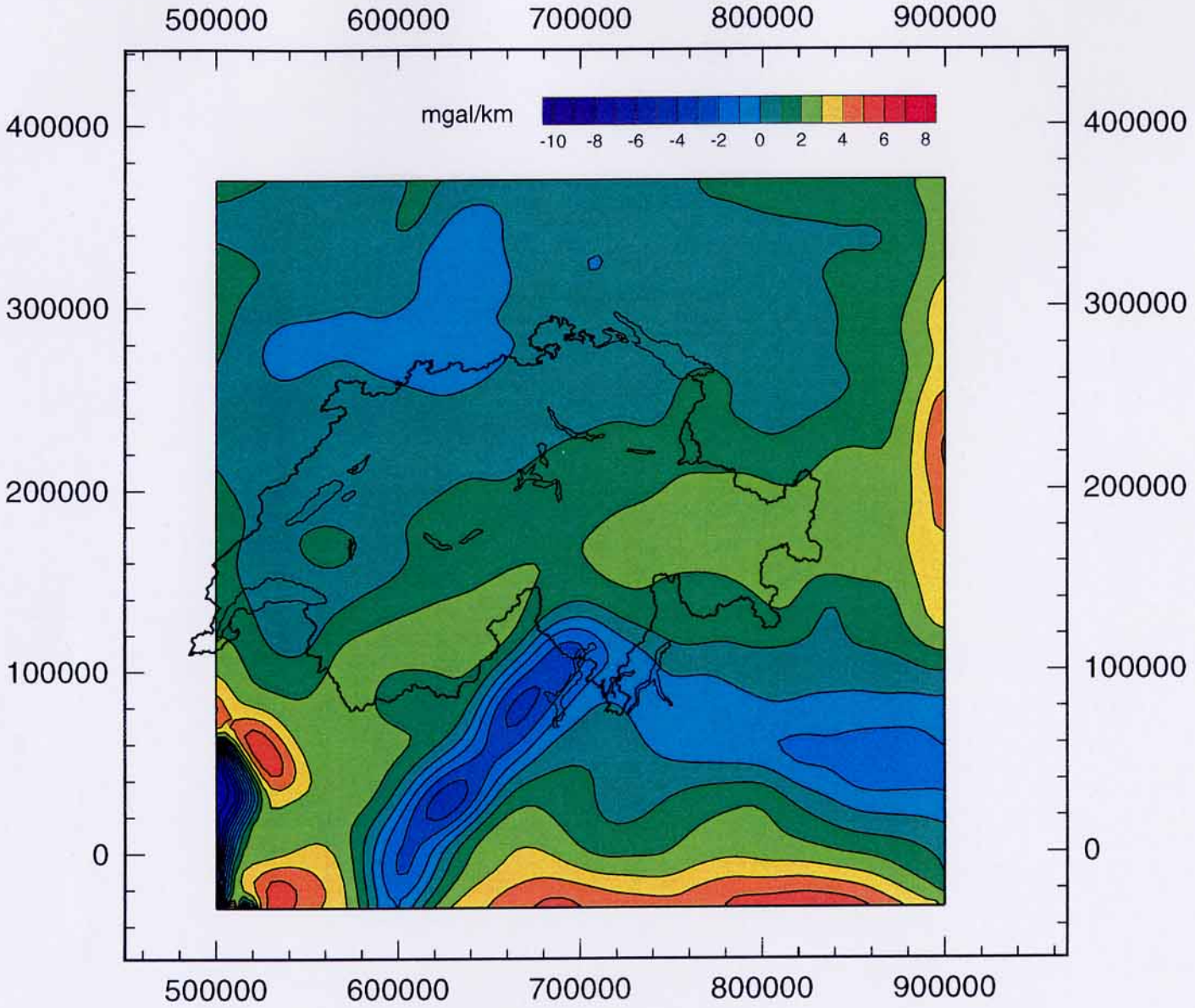

Figure 9.17: Vertical gradient at 5000 m over Switzerland and conterminous areas computed from EGT Bouguer anomalies upward-continued at 5200 m and 4800 m by means of a FFT algorithm.

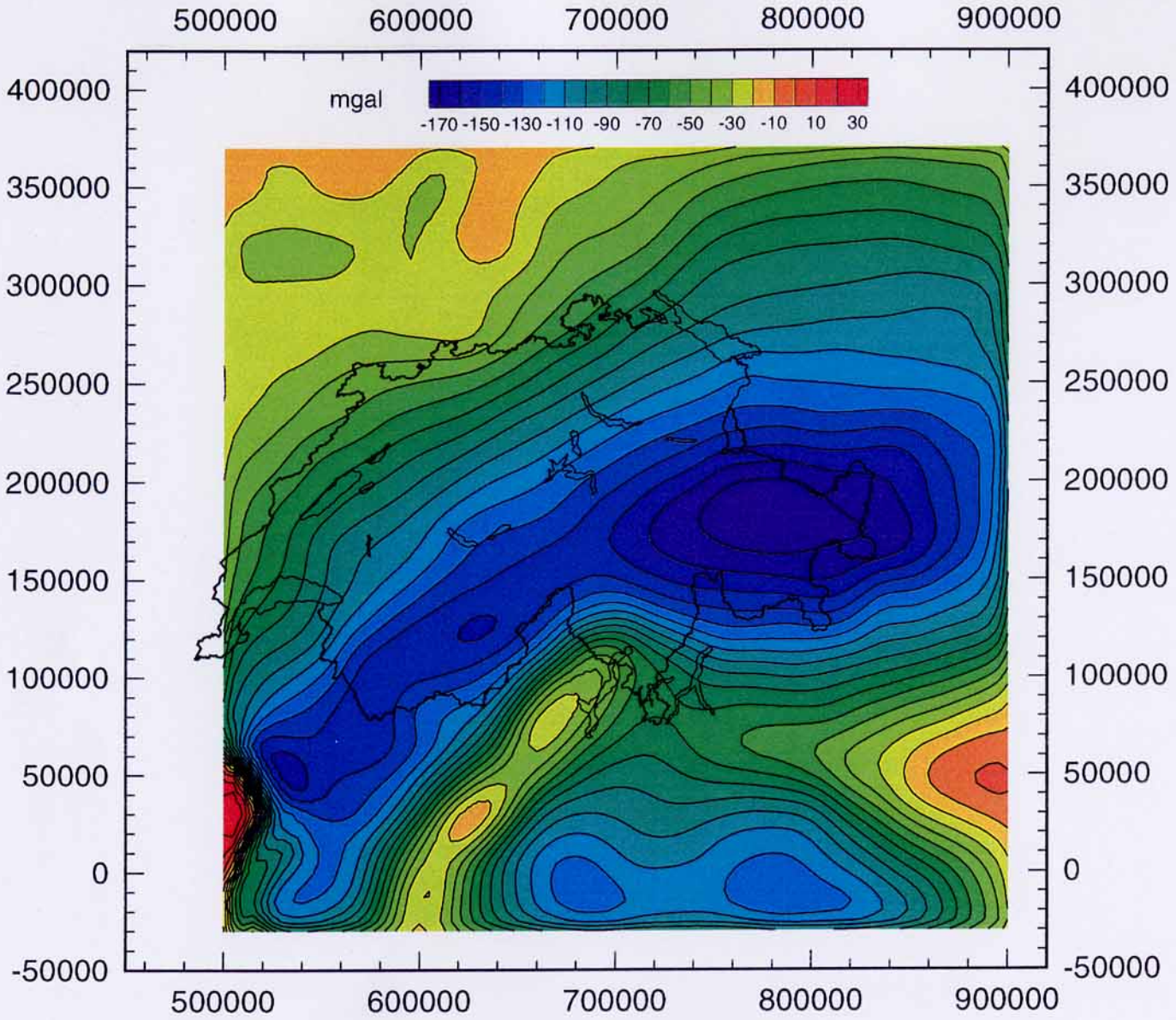

Figure 9.18: Bouguer anomaly at 5000 m over Switzerland and conterminous areas computed from EGT data upward-continued by means of a FFT algorithm.

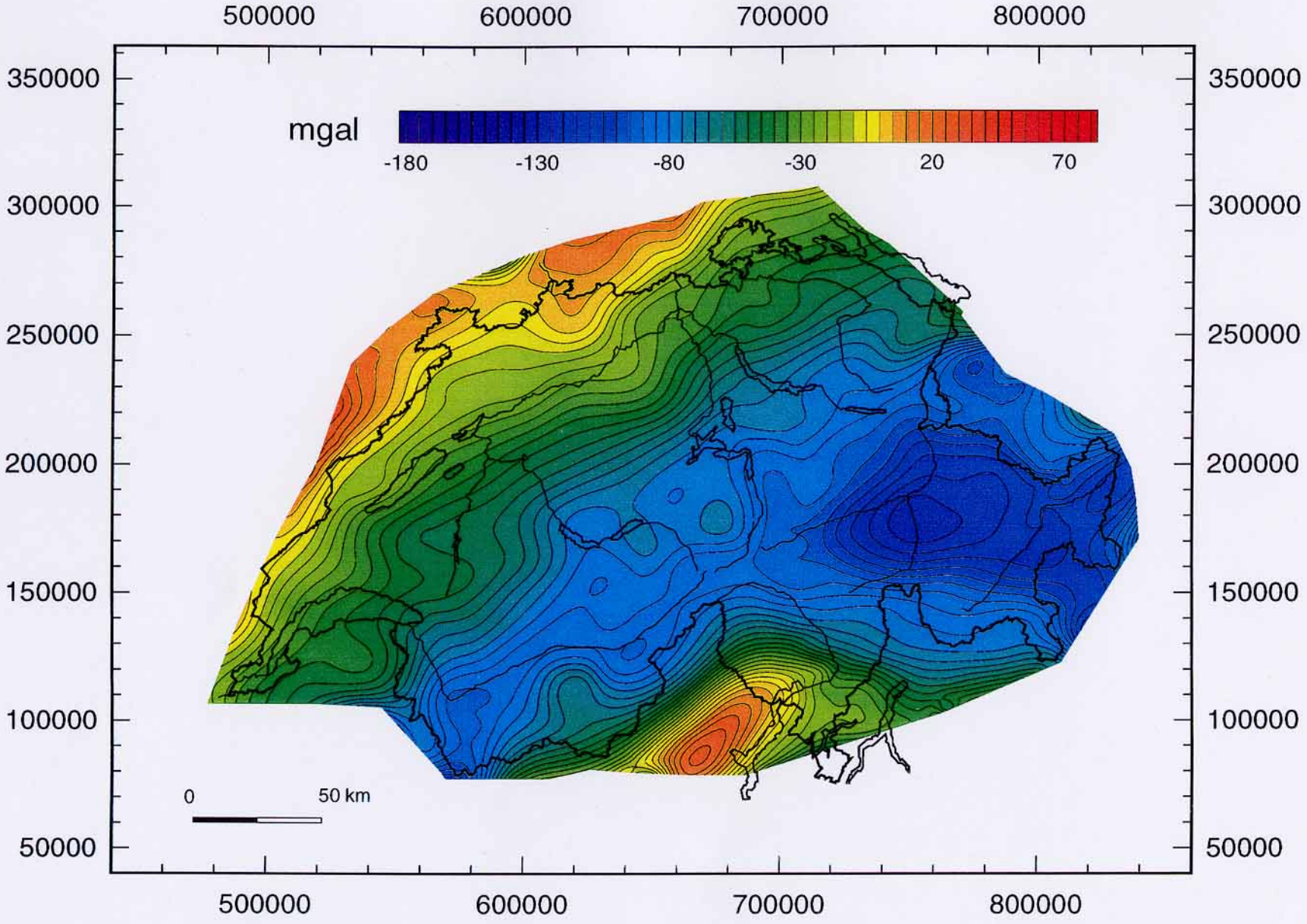

Figure 9.19: Airborne Bouguer anomaly map of Switzerland used for the computation of the vertical gravity gradient at 5000 m altitude. This map has been computed at flight altitude without reduction of first order shift and equalization.

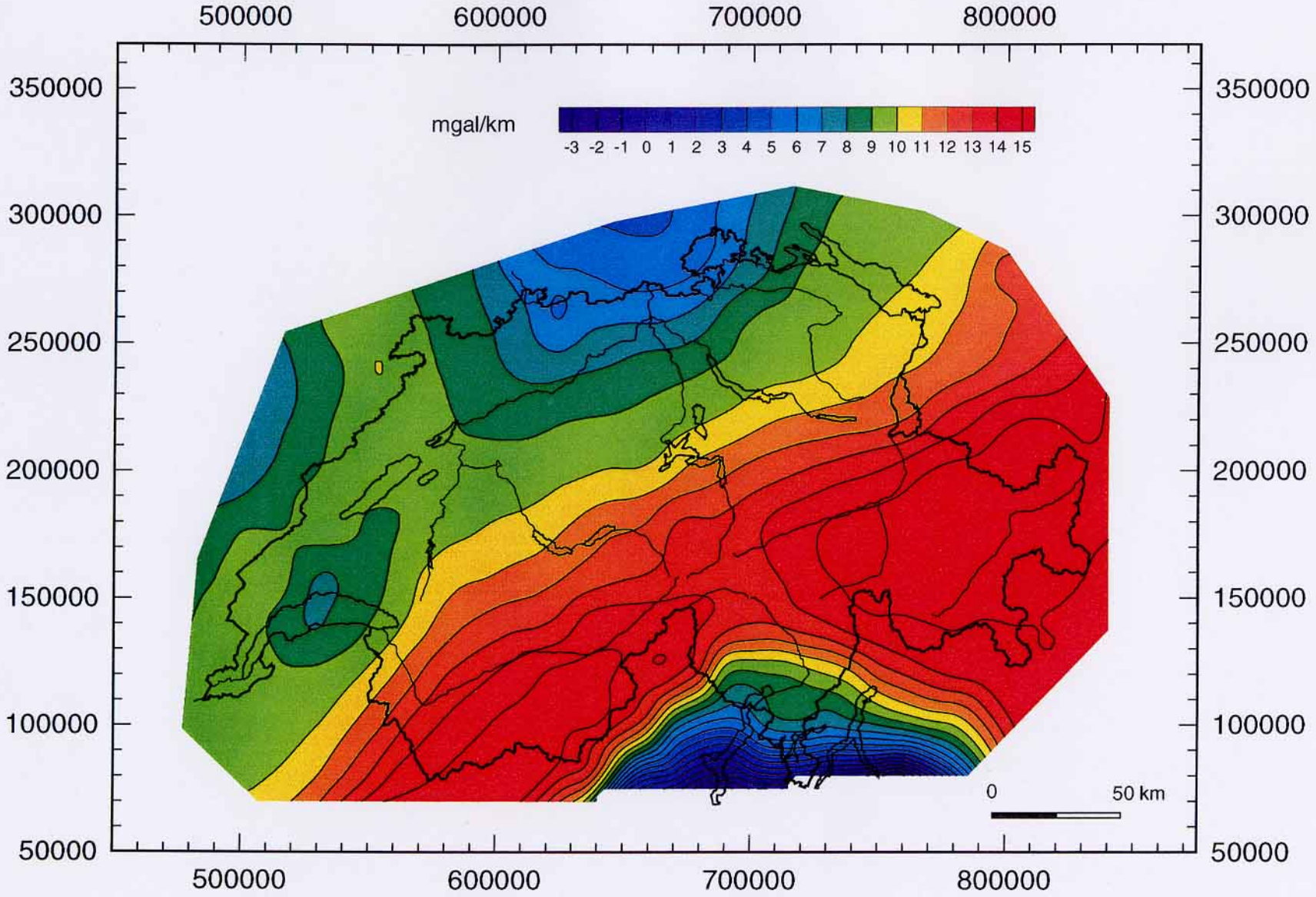

Figure 9.20: Vertical gradient at 5000 m computed with the anomaly of figure 9.19 and the ground Bouguer anomaly map of Switzerland (Klingele and Olivier, 1980).

9.10 The equalization

As in an airborne magnetic survey it is necessary to reduce the differences of the Bouguer anomalies at the crossing points between N-S and W-E lines. This can be done after these differences have been extracted from the full set of data.

The procedure developed in the framework of this project for searching the crossing points, is fully automatic and generates a data set containing the coordinates of the crossing points and the corresponding difference of measured *g*, Bouguer or Free-Air anomaly. A diagram is also produced which shows the values along the two lines some kilometers before and after the crossing point. This information is useful because it gives indications about the behavior of the anomaly around the measurement point: Two very smooth curves showing a large difference indicate that a constant shift is present in the measurement and could be attributed, for example, to a wrong reference value. One or both curves with a strong horizontal gradient indicate that the difference can be produced by the inaccuracy of the coordinates. A better analysis can be performed if the flight altitudes are also given in the same diagram. These differences give a good estimate of the quality of the survey. A detailed analysis of these data is given in chapter 12.2.

Figure 9.21 shows the raw differences of the Bouguer anomalies obtained at the crossing points. Some of the largest differences are not representative because the crossing points are situated too close to the beginning or the end of the line where the transient effect of the RC filter is still present. This is the case for the crossing points between lines 24.1 and 4.1; 24.1 and 10.1; 23.1 and 10.1; 23.1 and 17.2; 22.1 and 17.2.

Additionally because some lines do not have any crossing points, an equalization procedure would be without significance. We therefore decided to apply only some constant shifts (also called first order shifts in the literature) in order to reduce the amplitudes of the miss-ties. These shifts were simply the mean values of the differences along a N-S line. There are :

0	mgal for line 21.1
+7	mgal for line 22.1
+6	mgal for line 23.1
+5	mgal for line 24.1

The final values at the crossing points are presented in Figure 9.22.

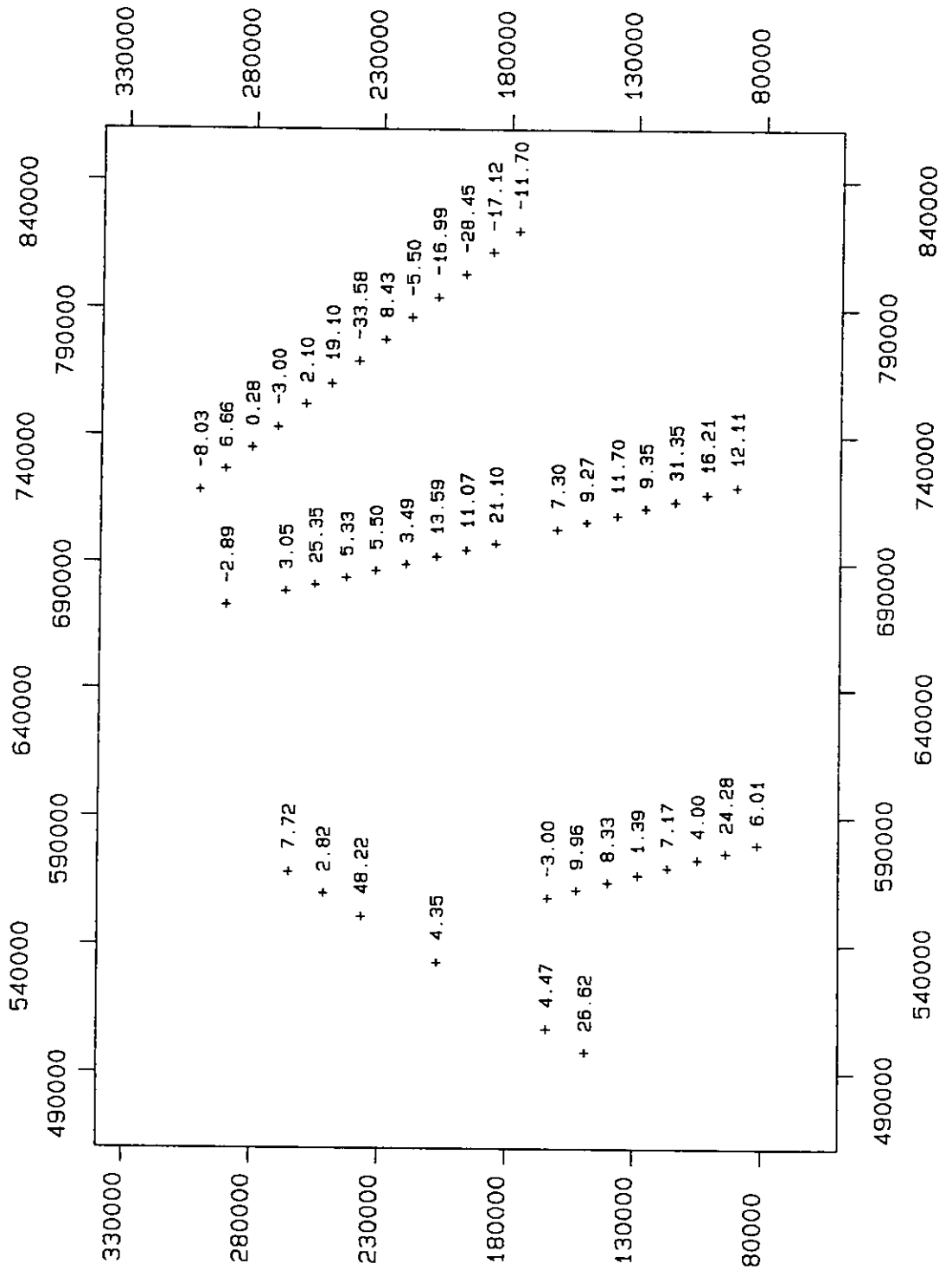

Figure 9.21 : Differences of the Bouguer anomaly obtained at the crossing points between W-W and N-S lines before first order shift removal.

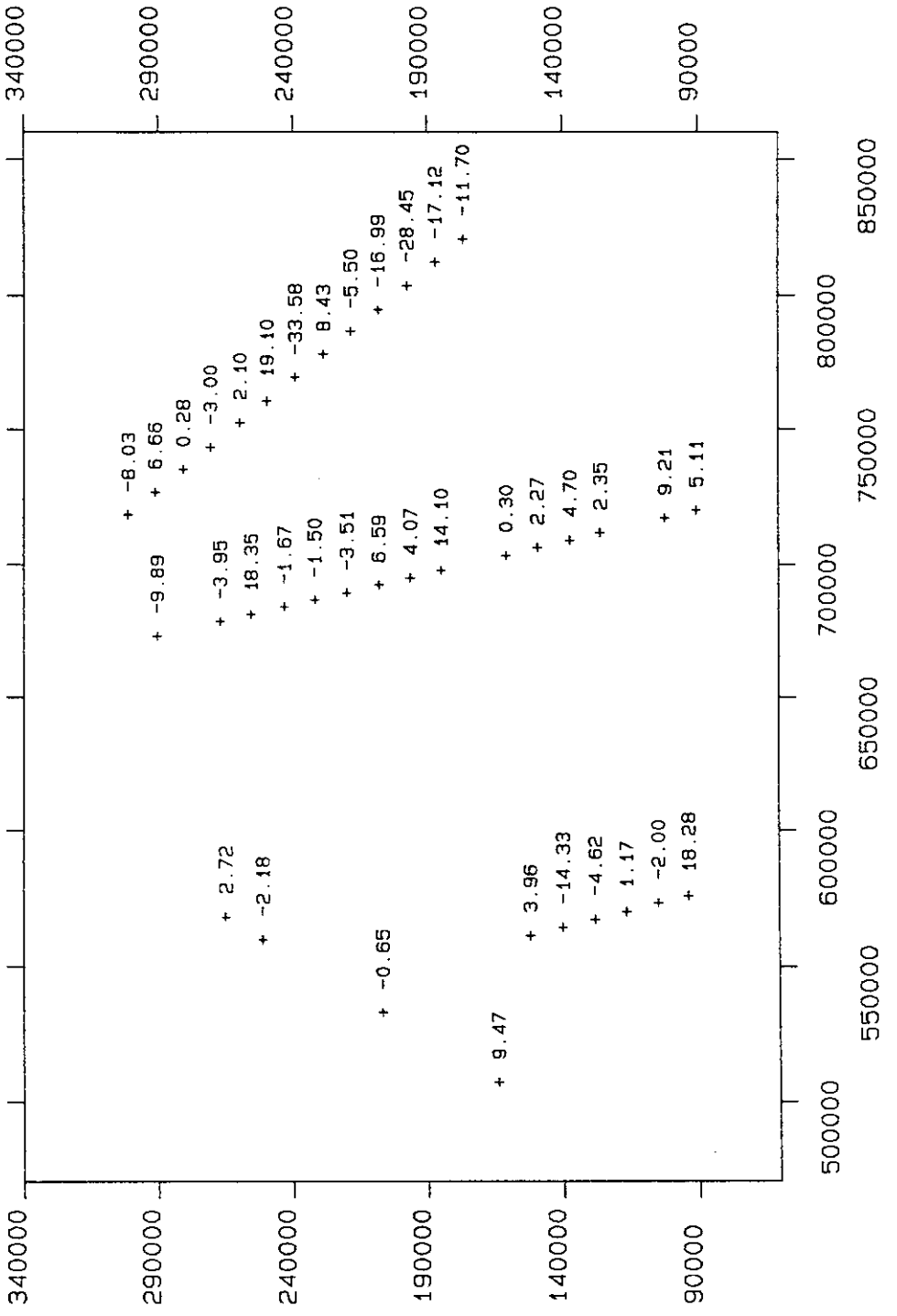

Figure 9.22 : Differences of the Bouguer anomaly obtained at the crossing points between W-W and N-S lines **after** first order shift removal.

10 The cartography

10.1 The preparation for the gridding

A curve approximated by segments of straight lines each three millimeters in length give a good visual effect of the curvature. Therefore a mesh size of 1 km times 1 km was adopted to produce a map of the full Bouguer anomaly at a scale of 1/500'000.

For the cartography, we choose a procedure made up of four steps: one step of pre-gridding, two steps of interpolation and the final step of mapping. Because the number of single values was very high, around 81'000, and the final grid had a mesh size of 1 km, it was necessary to reduce the number of points used for the interpolation. For this reduction we applied a moving-window of nine points with a decimation operator of nine. During the same procedure the parts of the lines number 01.1 to 11.1 which showed a horizontal gradient stronger than 4 mgal/km were removed. All these lines lie over the Jura mountains and the Molasse basin.

10.2 The gridding

The gridding was carried out in two stages. In the first one a coarse grid, with a square mesh with a side that is slightly smaller than half the distance between the profiles was calculated. To do this, a method similar to that described by La Porte (1962) was used: The experimental points inside a circle of radius R_0 centered on the point to be interpolated are approximated by a second-order polynomial of the type

$$F(x,y) = a_0 + a_1 x + a_2 y + a_3 x^2 + a_4 xy + a_5 y^2$$

in a least-squares fit procedure. Before performing this operation a weighting procedure is used, based on the term R^{-2} in order to reduce the effect of distant values. The weight attributed to a point P_j is (Figure 10.1)

$$W_i = \left(\frac{R_0^2 - d_i^2}{d_i^2 - \eta^2} \right)^2$$

where d_i is the distance between the center of the circle and the point P_i, η is a smoothing factor and R_0 the radius of the area around P_i where the experimental points are tacken into account. In our procedure the smoothing factor η is not given as an absolute value but as a function of the search radius R_0.

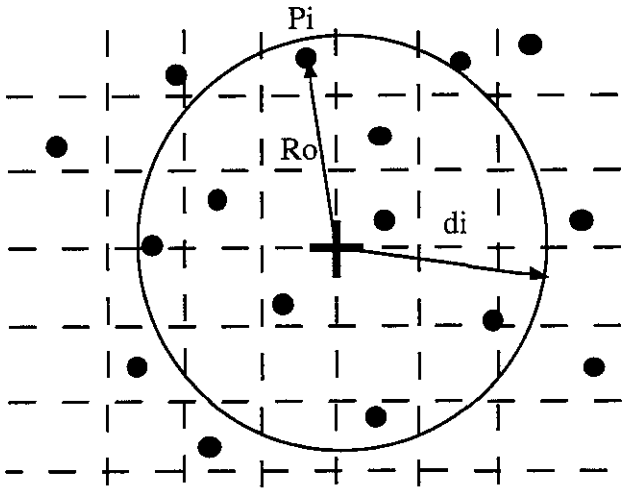

Figure 10.1: Data selection to compute the data grid.

The second stage allows the refining of the initial grid to obtain a much finer one, needed for good-quality tracing. To save computing time, the interpolation is done first line by line on the initial grid. One then obtains a rectangular grid with the smallest dimensions, equal to $1/K$ times the original grid size, coinciding with the horizontal axis. Secondly, one proceeds to an interpolation column by column on the previously obtained intermediate grid. This twofold uni-dimensional interpolation uses a spline under tension whose variations of the stress factor allows an interpolation ranging from a broken line to a classical bi-cubic spline (Cline 1974). The fine grid has a size of $M\ (K - 1)$ by $N\ (K - 1)$, where M and N are the dimensions of the large scale grid, and K is the refinement factor.

Finally this grid was used by the program ISOVAG (Klingelé 1980) to produce isolines which were chosen to give well-defined and clearly visible anomalies (Figure 10.2) and by the mapping package TECPLOT for producing color maps (Figure 10.3).

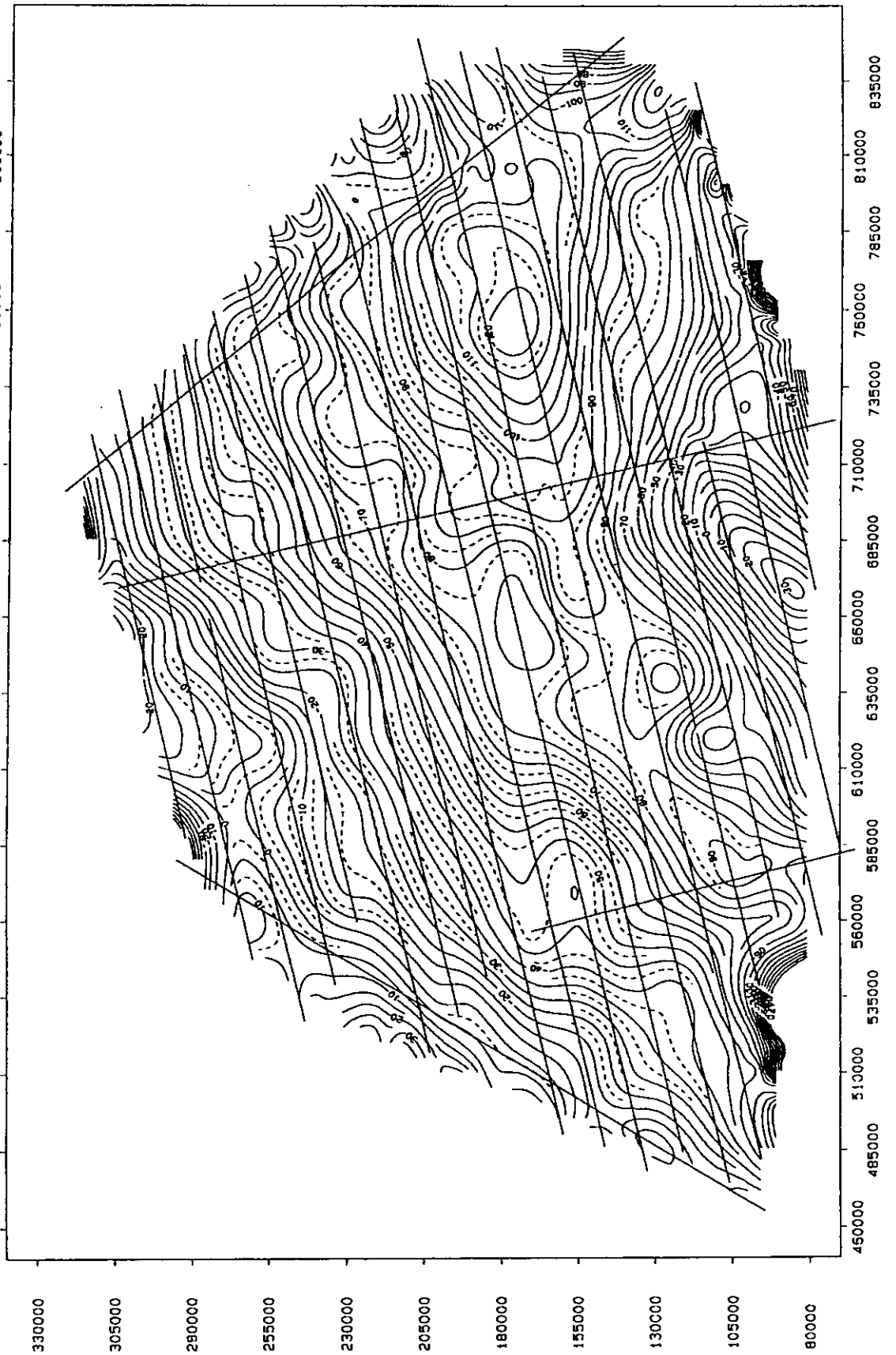

Figure 10.2 : Full airborne gravimetric map of Switzerland at altitude of 5100 m s.l.
Topographic corrections up to 167 km with density 2670 Kg.m^{-3}

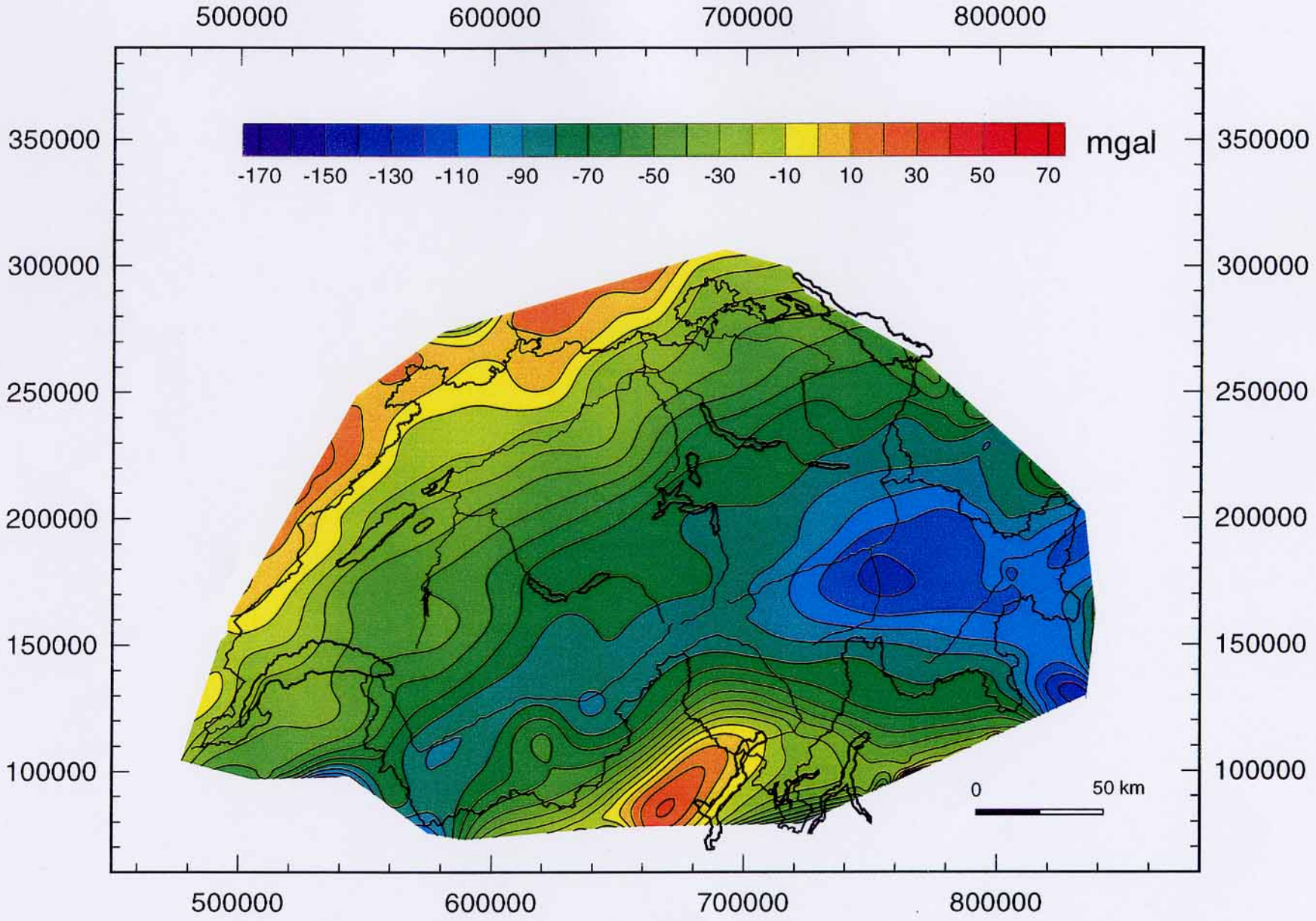

Figure 10.3: Color version of the map of figure 10.2 made with the software package TECPLOT.

11 Base station

The aircraft was stationed during the whole survey period at the aiport of Zurich-Kloten. Because the measured g value has to be refered to a ground value the entire parking place was surveyed and tied to the fundamental absolute gravity station of Switzerland. This station is located at the Geodetic Institute of the Swiss Federal Institute of Technology (ETH) in Zurich-Hoenggerberg. Its value is

$$9.80647967 \ ms^{-2}$$

The measurements at the airport were made at the nodes of a grid shown in figure 11.1 with a LaCoste and Romberg model G gravimeter and were reduced for drift and earth tide effects.

The mesured values refered to 980000 mgal, were the following :

A1 : 674.52	B1 : 674.51	C1 : 674.54	D1 : 674.54
A2 : 674.45	B2 : 674.45	C2 : 674.45	D2 : 674.47
A3 : 674.37	B3 : 674.36	C3 : 674.39	D3 : 674.37
A4 : 674.29	B4 : 674.29	C4 : 674.30	D4 : 674.35
A5 : 674.21	B5 : 674.21	C5 : 674.22	D5 : 674.24
A6 : 674.18	B6 : 674.21	C6 : 674.15	D6 : 674.18

Considering the fact that the aircraft was always parked inside a rectangle defined by the points A3 - A5 and C3 - C5, the value adopted for the base station was that of point B4 :

$$g_b = 9.80674\ 29 \ ms^{-2}$$

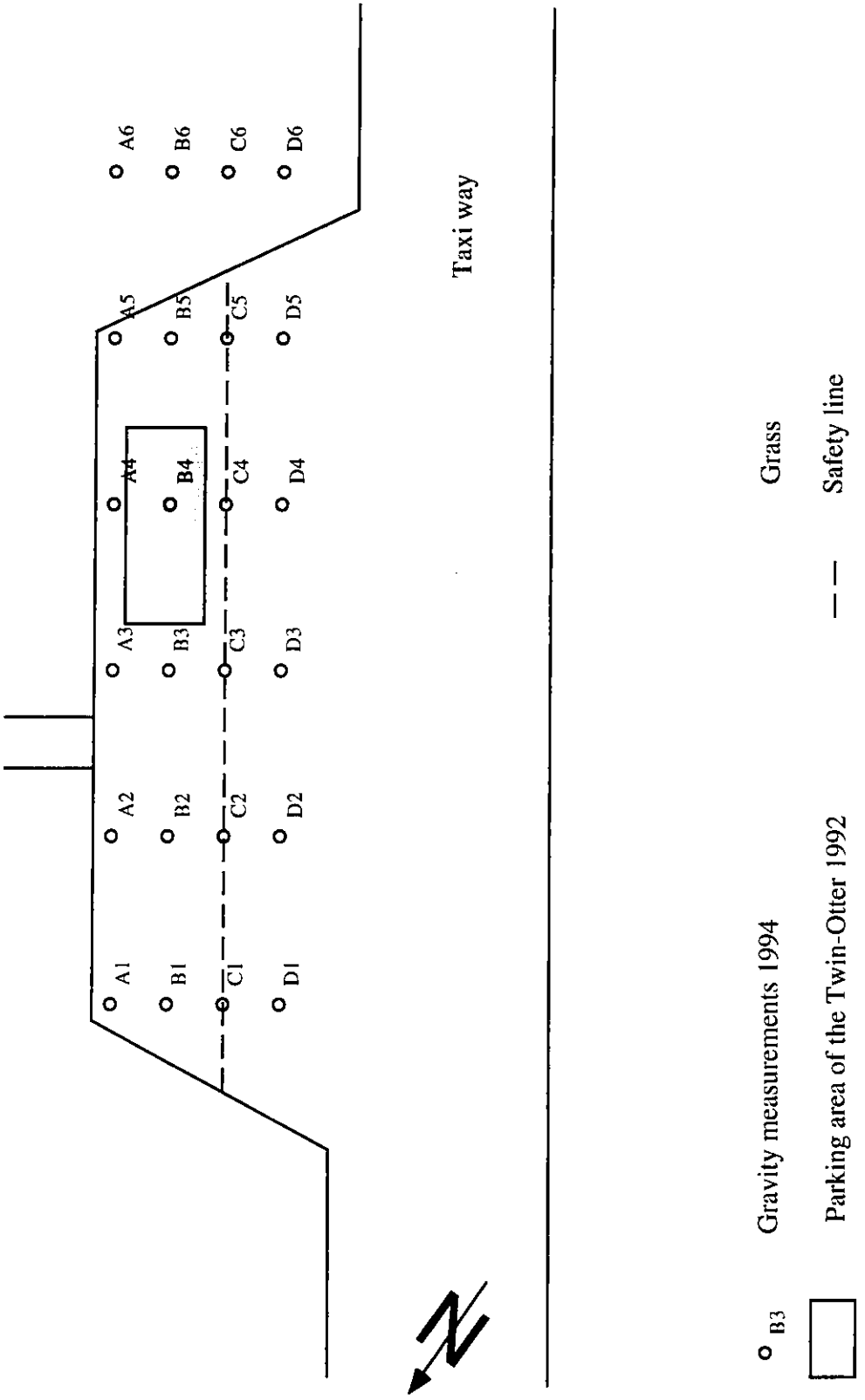

Figure 11.1: Map of the parking place of the aircraft during the Swiss survey. The points A1 to D6 correspond to the locations of the measurement stations for determining the homogeneity of the field.

12 Evaluation of the data quality

12.1 Introduction

An evaluation of the quality of the data is presented firstly in the form of an analysis of the differences at the crossing points between N-S and W-E lines, secondly through a comparison between ground data and airborne data along three N-S profiles, and finally by airborne and ground Bouguer anomaly maps.

12.2 Comparison at the crossing points

The results presented in this paragraph concern only five crossing points. These points were chosen because the lines cross each other at altitudes differing by less than 10 meters. Very small altitude differences allow for significant comparison between the anomalies at the crossing points, because the reduction to the same altitude, even when computed with an inaccurate vertical gradient, does not introduce large distortions. For the reduction at comparable altitude, we used the local value of the vertical gravity gradient determined by the method described in chapter 9.9.

The lines fulfilling the condition of comparable altitudes are line numbers : 3.2, 14.1, 21.1, 22.1 and 23.1.

The results obtained without first order shift removal are given in Table 12.1.

N-S	E-W	Δh (m)	Δg raw (mgal)	Vert. Grad (mgal/m)	Δg corr. (mgal)
21.1	3.2	7.40	6.66	0.0075	6.60
21.1	14.1	7.37	11.70	0.0155	11.59
22.1	14.1	3.27	2.27	0.0135	2.23
23.1	14.1	1.95	1.17	0.0135	1.14
24.1	2.1	7.62	2.62	0.0075	2.67

Table 12.1: Crossing points used for the evaluation of the quality of the data.
Column 1 : Number of the N-S lines.
Column 2 : Number of the W-E lines.
Column 3 : Differences of altitude at the crossing points.
Column 4 : Differences of Bouguer anomaly at the crossing points.
Column 5 : Local vertical gradient used for corrections.
Column 6 : Corrected differences of Bouguer anomaly at the crossing points.

Figures 12.1 to 12.5 show the measured g values along lines 21.1, 22.1 and 23.1 approximately three kilometers before and after the crossing points with lines 3.2, 14.1 and 2.1.

12.3 Comparison along flight lines

The comparison is only made along the N-S line numbers 21.1, 22.1 and 23.1 because they are approximately perpendicular to the elongation of the major anomaly. For this comparison, Bouguer data were extracted from the EGT data set and interpolated along profiles corresponding to the theoretical locations of line 21.1, 22.1 and 23.1.

These interpolated values were then upward continued by means of an integration algorithm :

$$\Delta g(x,z) = \frac{1}{2\pi} \int_{-\infty}^{+\infty} \frac{\Delta g(\bar{x},0)\, z}{\left[(\bar{x}-x)^2 + z^2\right]^{3/2}}\, d\bar{x}$$

The RMS of the differences between upward continued anomalies and airborne anomalies are the following :

13.3 mgal for line 21.1 based on 430 values
7.3 mgal for line 22.1 based on 397 values
3.1 mgal for line 23.1 based on 144 values
10.1 mgal for the three lines together

These comparisons are graphically depicted in figures 12.6 to 12.8.

12.4 Comparison between ground and airborne maps

For this comparison the EGT data were interpolated to form a grid coinciding with that of the airborne data and then upward continued to 5100 m by means of the same FFT algorithm as described in chapter 9.9. Taking into account the fact that the very long wave-lengths are not present in the upward continued field, a first order shift of 50 mgal which minimized the residual was applied to these data. The **RMS** value of the differences computed with 61438 grid points is **11.09** mgal, the **mean** value is **0.60** mgal and the **standard deviation** is **11.08** mgal.

A histogram of these differences is presented in figure 12.9 and a spatial representation (map) in figure 12.10.

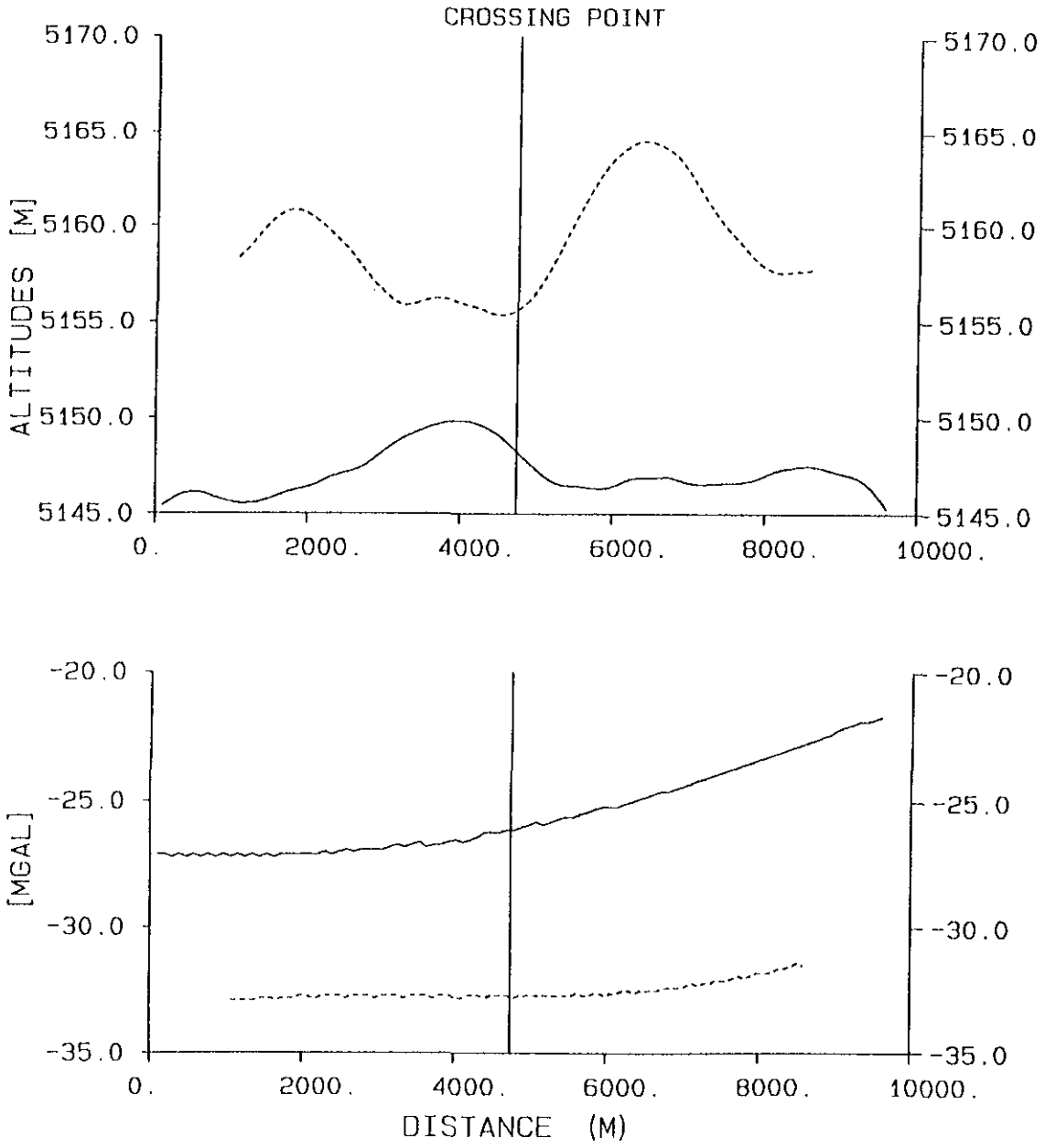

BOUGUER ANOMALY AND ALTITUDE

AT THE CROSSING POINT 726785 / 291088

BETWEEN LINES

3.2 AND 21.1

——— LINE 3.2

- - - - - LINE 21.1

DIFFERENCE OF G [MGAL] = 6.66

DIFFERENCE OF H [M] = 7.40

VERT. GRAD. = -0.90

Figure 12.1 Bouguer anomalies (lower diagram) and altitudes (upper diagram) three kilometers before and after the crossing point between lines 3.2 and 21.1

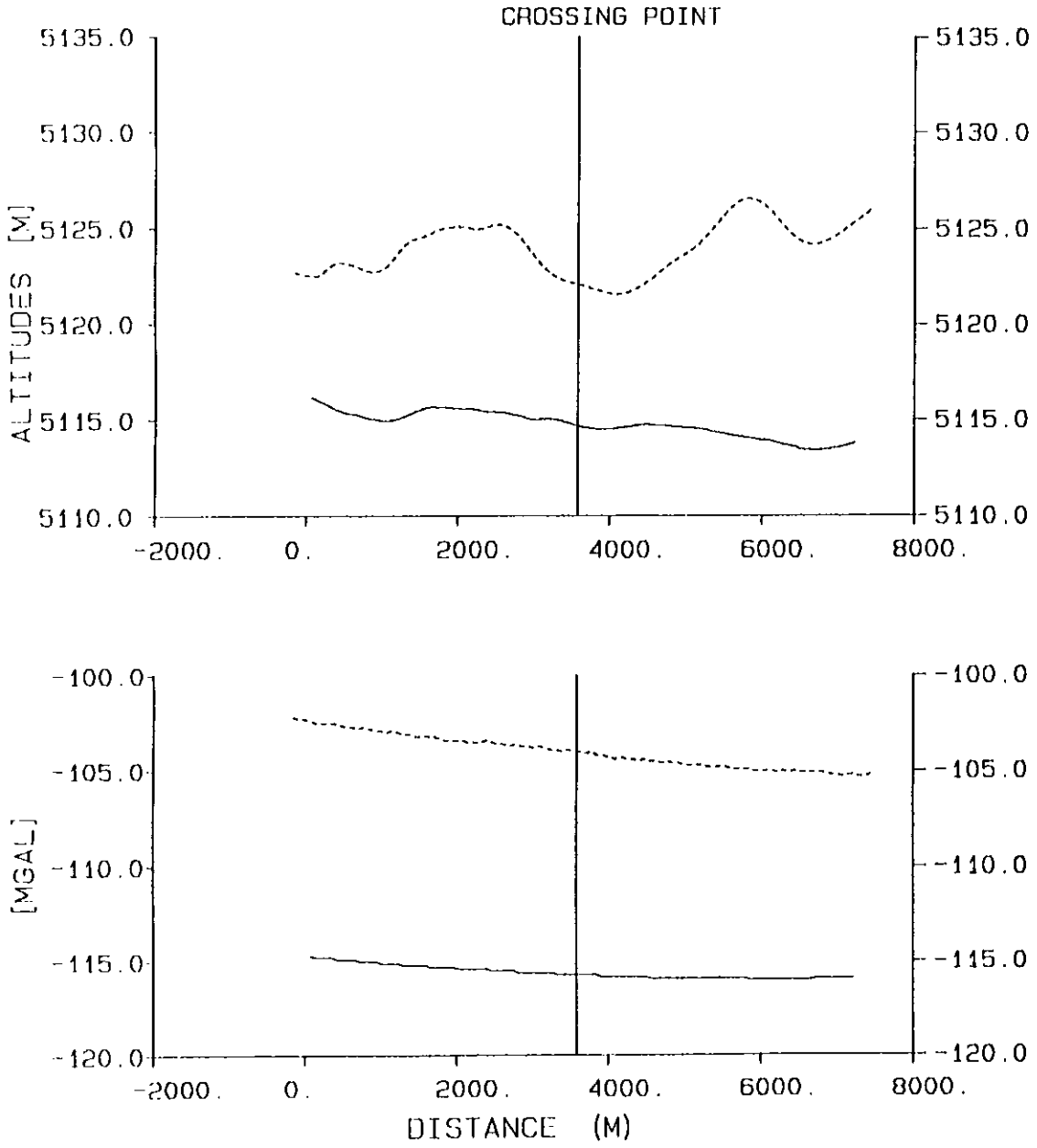

BOUGUER ANOMALY AND ALTITUDE

AT THE CROSSING POINT 820479 / 176708

BETWEEN LINES

14.1 AND 21.1

———— LINE 14.1

- - - - - LINE 21.1

DIFFERENCE OF G [MGAL] = 11.70

DIFFERENCE OF H [M] = 7.37

VERT. GRAD. = 1.59

Figure 12.2 Bouguer anomalies (lower diagram) and altitudes (upper diagram) kilometers before and after the crossing point between lines 14.1 and 21.1

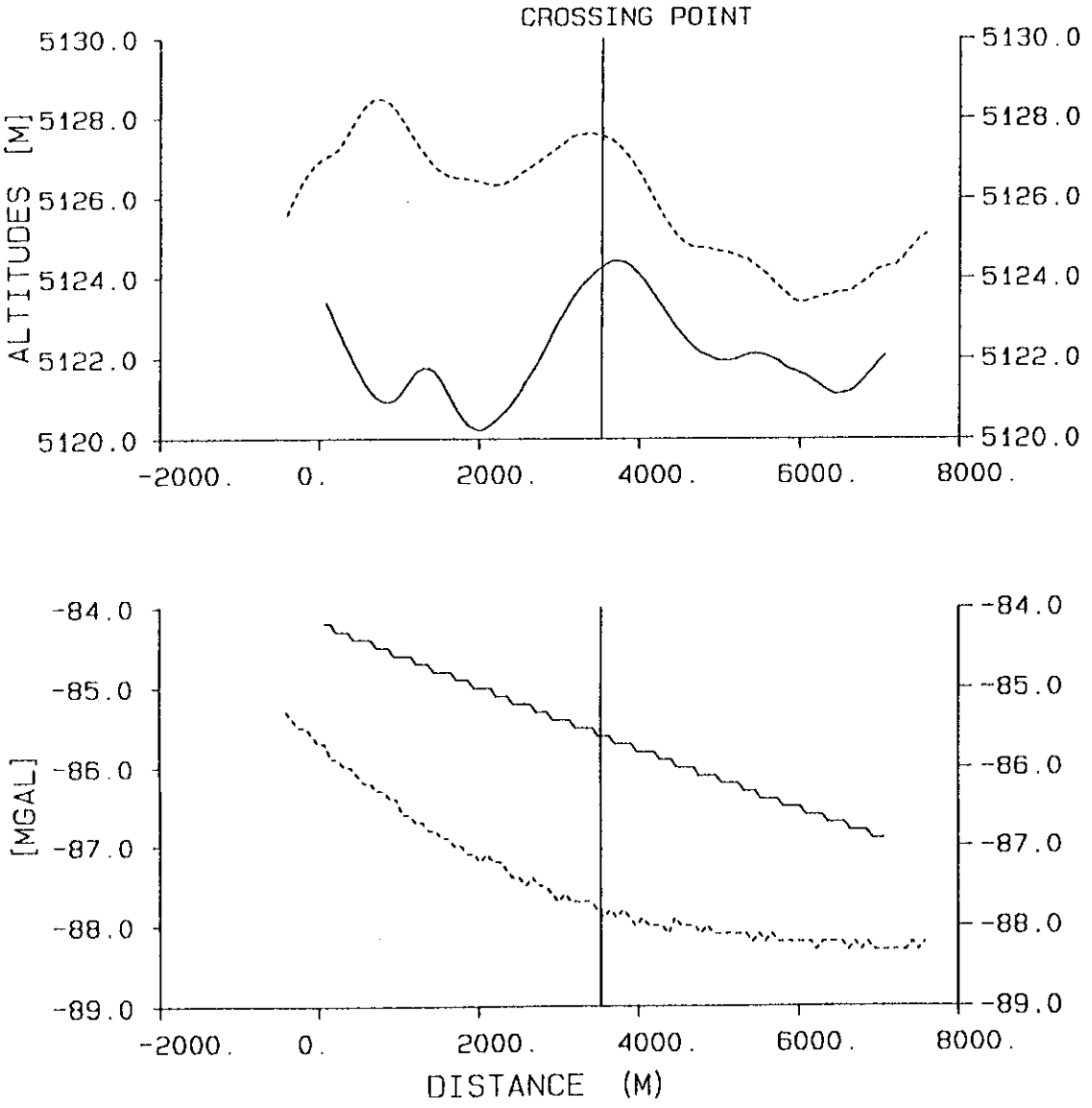

BOUGUER ANOMALY AND ALTITUDE

AT THE CROSSING POINT 706174 / 149317

BETWEEN LINES

14.1 AND 22.1

———— LINE 14.1

- - - - - LINE 22.1

DIFFERENCE OF G [MGAL] = 2.27

DIFFERENCE OF H [M] = 3.27

VERT. GRAD. = -0.69

Figure 12.3 Bouguer anomalies (lower diagram) and altitudes (upper diagram) three kilometers before and after the crossing point between lines 14.1 and 22.1

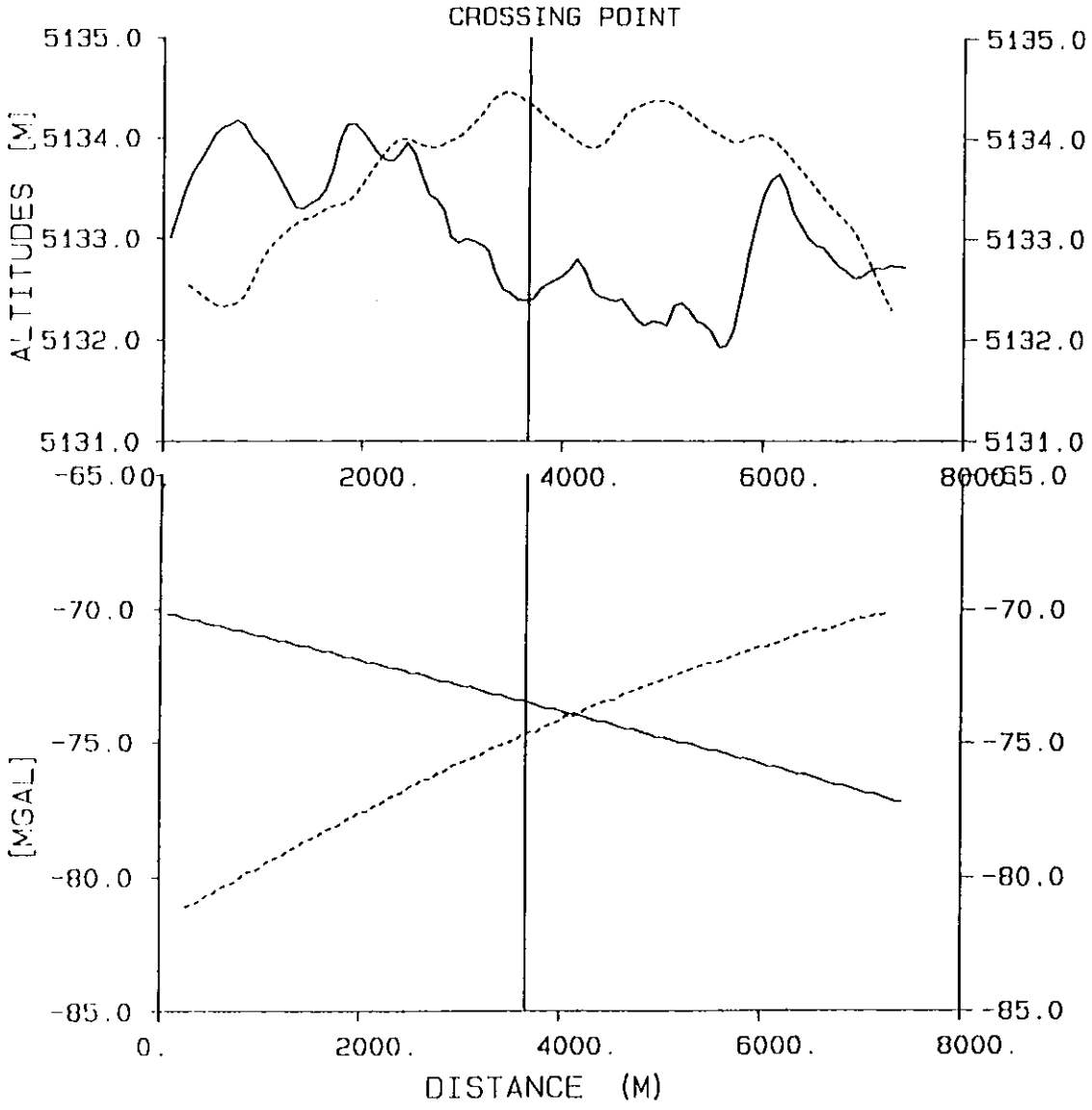

BOUGUER ANOMALY AND ALTITUDE

AT THE CROSSING POINT 570162 / 116757

BETWEEN LINES

14.1 AND 23.1

——— LINE 14.1

- - - - - LINE 23.1

DIFFERENCE OF G [MGAL] = 1.17

DIFFERENCE OF H [M] = 1.95

VERT. GRAD. = -0.62

Figure 12.4 Bouguer anomalies (lower diagram) and altitudes (upper diagram) three kilometers before and after the crossing point between lines 14.1 and 23.1

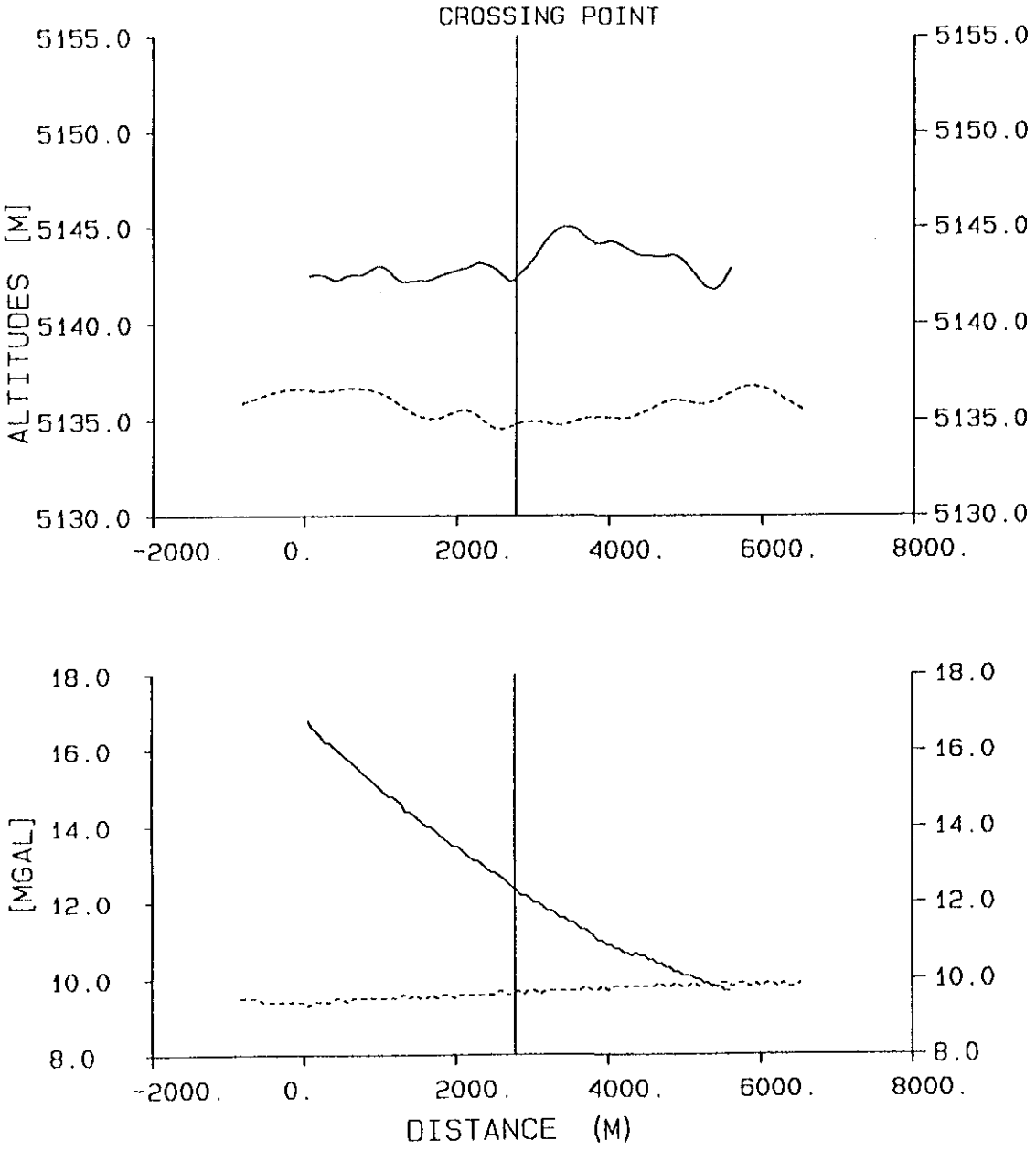

BOUGUER ANOMALY AND ALTITUDE

AT THE CROSSING POINT 568304 / 265001

BETWEEN LINES

2.1 AND 24.1

——— LINE 2.1

- - - - - LINE 24.1

DIFFERENCE OF G [MGAL] = 2.72

DIFFERENCE OF H [M] = 7.62

VERT. GRAD. = 0.35

Figure 12.5 Bouguer anomalies (lower diagram) and altitudes (upper diagram) three kilometers before and after the crossing point between lines 2.1 and 24.1

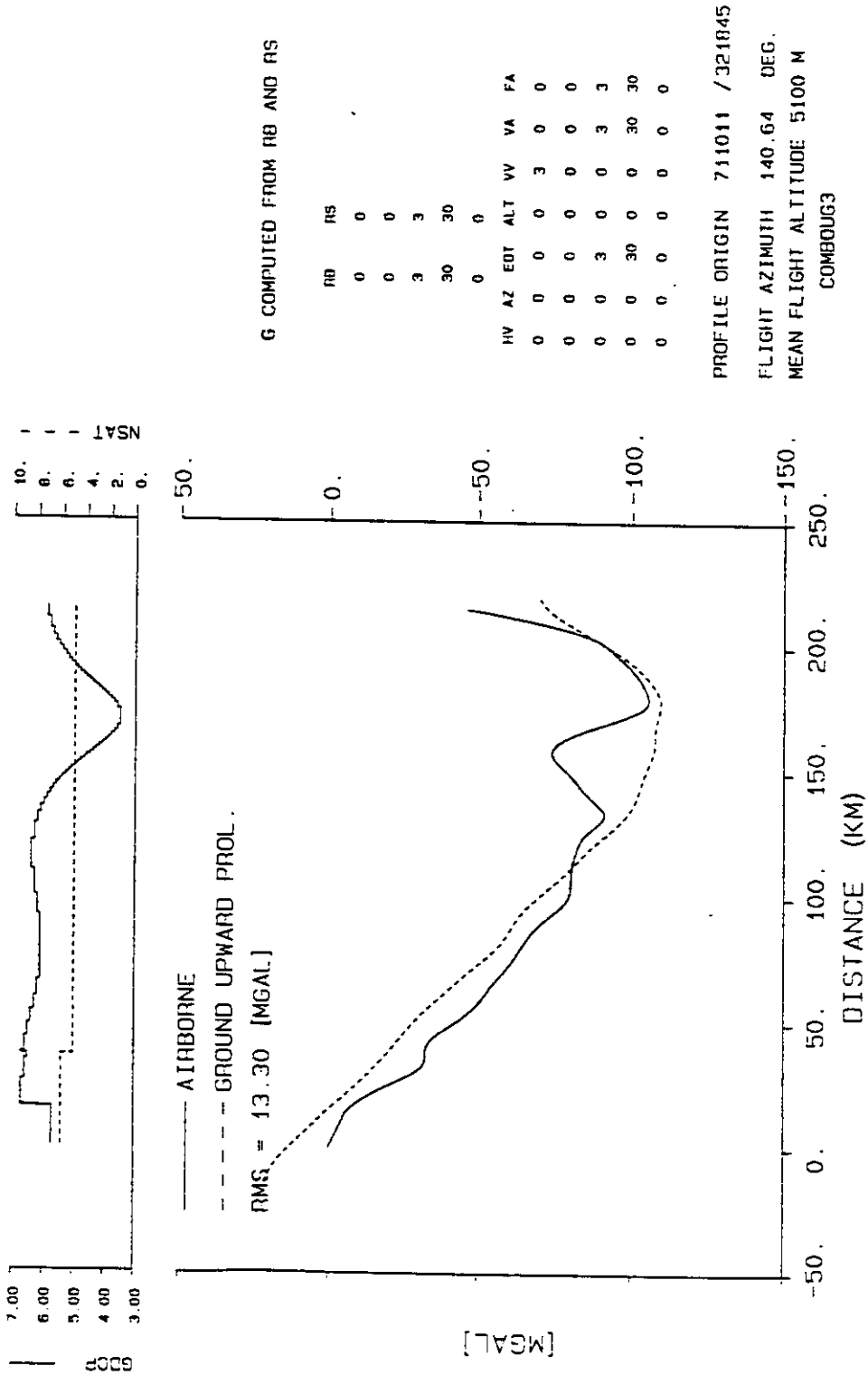

Figure 12.6 : Comparison between airborne and ground upward-continued Bouguer anomalies along line 21.1 . The upper diagram shows the number of available GPS satellites and the value of the GDOP during the measurements.

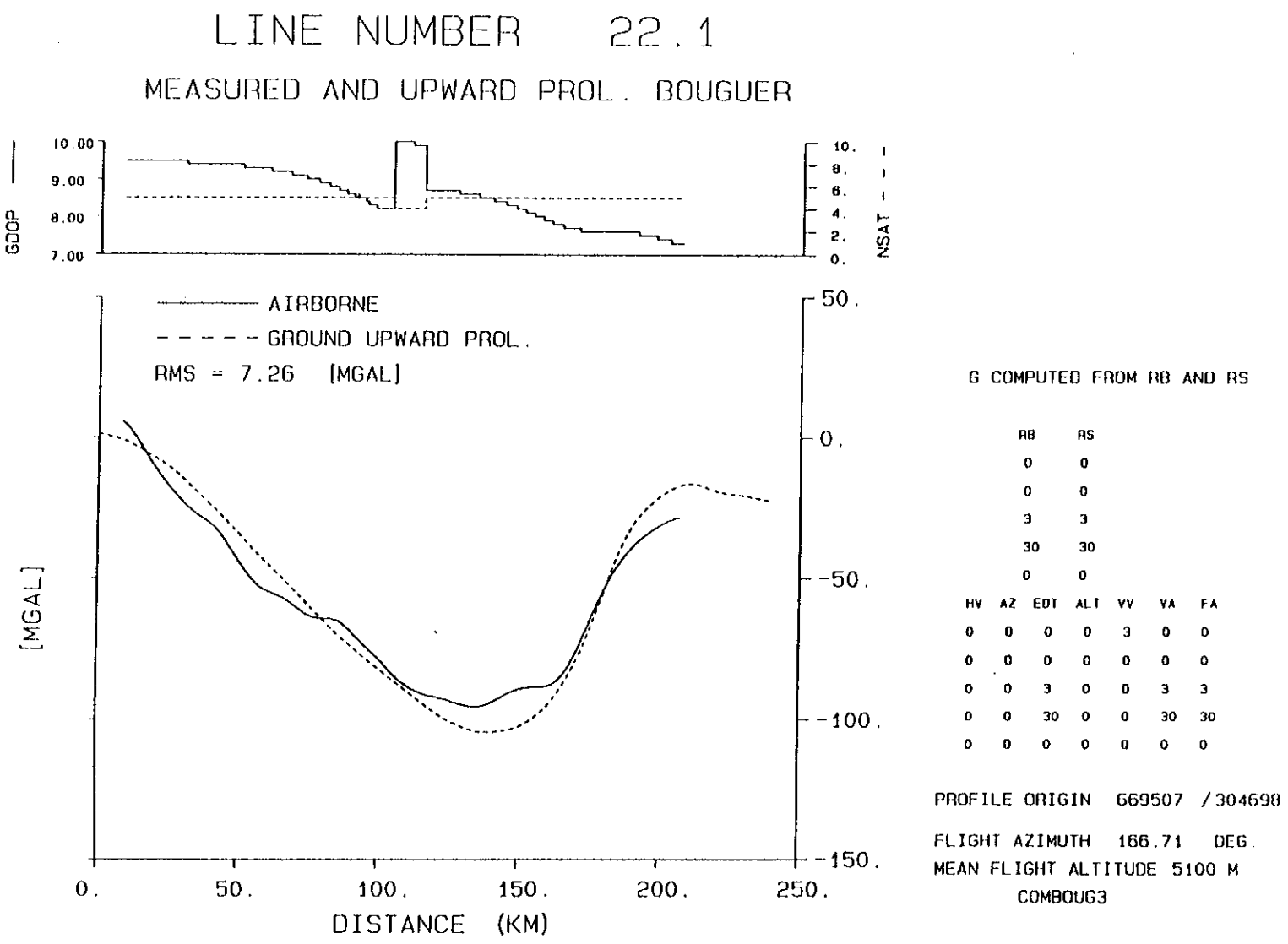

Figure 12.7 : Comparison between airborne and ground upward-continued Bouguer anomalies along line 22.1 The upper diagram shows the number of available GPS satellites and the value of the GDOP during the measurements.

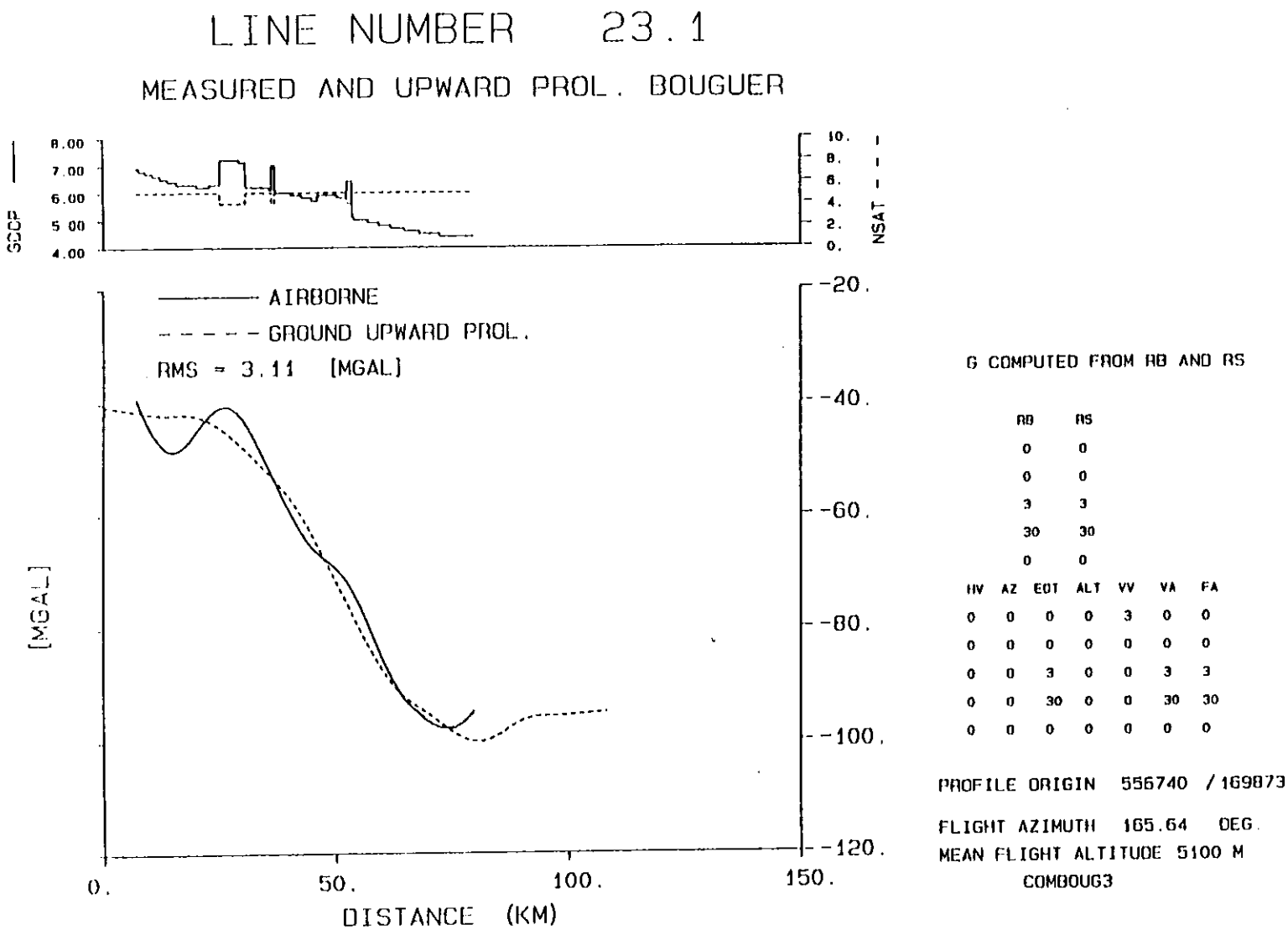

Figure 12.8 : Comparison between airborne and ground upward-continued Bouguer anomalies along line 23.1 The upper diagram shows the number of available GPS satellites and the value of the GDOP during the measurements.

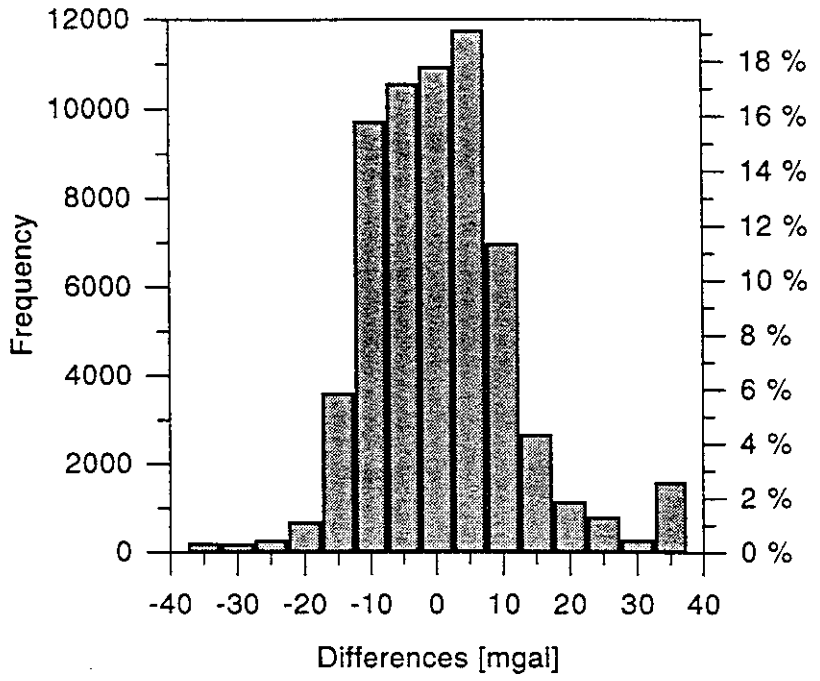

Figure 12.9 : Histogram of the differences between airborne and ground upward-continued Bouguer anomaly computed with 61438 grid points. (RMS = 11.09 mgal ; Mean = 0.60 mgal ; Standard deviation = 11.08 mgal.)

12.5 Remarks about the comparisons

Some important remarks about the comparisons with ground data have to be made in order that no erroneous conclusions be formulated.

- The distribution of the measurement points is absolutely not comparable. The airborne data are densely distributed along straight lines with 12 km spacing whereas the ground data are more or less regularly distributed over the surface, but with a much smaller density.

- As pointed out in chapter 9.9, the upward-continuation procedure is not of great accuracy because the very long wave-length component cannot be calculated or even estimated for such a large area.

- One has to remember that the Bouguer anomaly is over a surface; a so called support surface, defined by the measurement points. In the Alps this surface is a far away from being horizontal and a 2-D FFT upward continuation procedure is inaccurate per nature.

- Because of boundary effects the comparison between upward continued ground data and airborne data is representative only in an area limited by a line located 20 km inside the airborne survey and running parall to its limits.

- Because the airborne measurements are all above the topography and the disturbing sources, the influences of an inaccurate choice of the density used for reductions greatly influence the amplitudes and the shapes of the anomalies. In order to illustrate this remark we can take the following example.

Supposing a spherical disturbing body is situated inside a mountain and the measurement points are all around this mountain at exactly the altitude of the centre of the disturbing body, the Bouguer anomaly calculated with these measurements will not show any anomaly produced by this structure. An airborne survey flown above the mountain will, however show clearly the presence of this body. We can extend this example to the topography itself, if we consider that the disturbing body is formed by the volume of the rocks which have a density different of that chosen for the reduction. In the case of ground measurements, only the parts which are not symmetric, with regard to the horizontal plane passing through the station, will produce an anomaly. This is of course not the case for airborne measurements in which the whole volume will act.

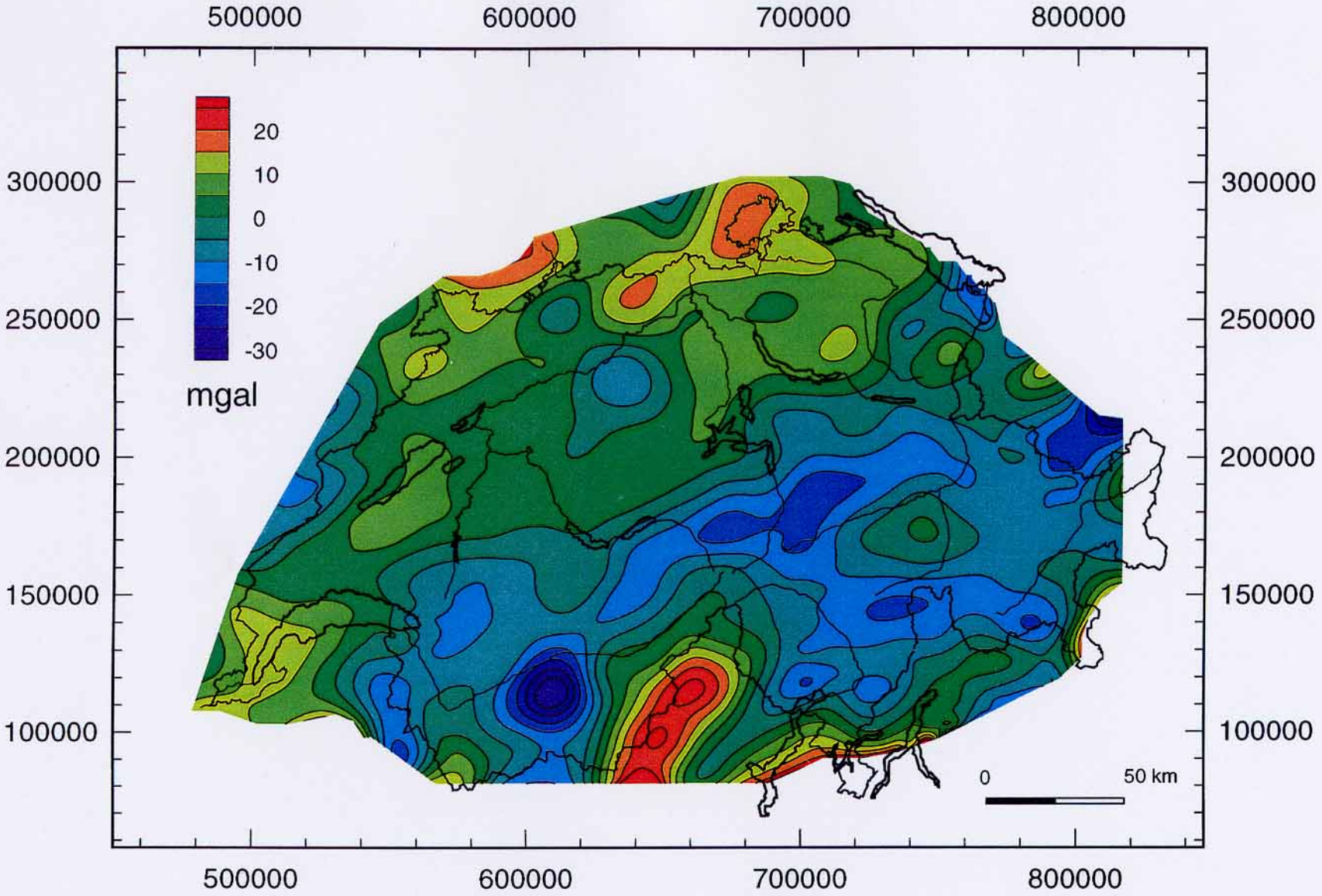

Figure 12.10: Map of the differences between airborne and ground upward-continued Bouguer anomaly. The ground data were extracted from the EGT data set and completed in the western part of the area with data of the Swiss Geophysical Commission.

13 Conclusions and recommendations

The results obtained show clearly that airborne gravimetry is a very promising method, especially for large scale and low sensitivity survey. The method has the advantage of integrating distant and deep seated disturbing bodies better and not being influenced by local density contrasts. It is certainly the best adapted method for surveying large inaccessible areas like the Amazon, Antarctica or even the Himalayas.

The results of the airborne survey of Switzerland are comparable to those of 1/500'000 scale ground data for the same area. They have almost the same resolution , i.e. 2 to 5 milligals in amplitude and ten to fifteen kilometers in wave-length, but they have the advantage of being located on a horizontal surface situated outside the disturbing sources.

The survey suffered particularly bad atmospheric conditions (measurements in November and December) and poor GPS satellite geometry (GDOP between 5 and 20).

Apart from the fact that the number of flight hours was limited, which did not allow for re-flying the lines of bad quality, the two preceding facts strongly affected the quality of the results. In our opinion, the same survey performed with calm atmospheric conditions and better satellite configuration would improve the spatial resolution.

Because of strong temperature inversions some lines were flown at altitudes of more than 5100 m and others below 5000 m. For the reduction the data at a same altitude, it was necessary to use an experimental local vertical gradient. This gradient, computed iteratively from ground and airborne data, was not of great accuracy and probably introduced distortions in the results, which are difficult to estimate.

For economical reasons it was not possible to fly closer N-S lines. This reduced the possibilities of estimating the values at the crossing points better and made the equalization impossible.

Finally, we would like to formulate some recommendations, based on our own experience. These recommendations could serve for further experiments and if taken into account, will certainly lead to better results and fewer computation difficulties.

- In order to avoid the problem of reducing the data to the same altitude, which must be kept the same for all the lines, it is better to use the information from a differential GPS rather than a barometric altimeter.

- Lines which have to be interrupted for some reason have to be re-flown entirely. The loss of quality of the data, by re-flying only the missing part of the line, is not compensated by the financial gain.

- The control lines (N-S line in our case) should be much closer than those we had to choose for economical reasons. We recommend that the distance between the control-lines be only twice that of the measurement lines.

- We think that the vertical accelerations induced by the phugoidal movements of the aircraft could be removed by using either a physical modeling of the aircraft, or by a Fourier series development. This last approach has been applied as a test to some lines and seems to be a promising one.

- Other kinds of recursive or transverse filters could be applied. In this case the lines have to be longer in order to keep the usable area the same.

14 Software packages

14.1 Introduction

The following is a short overview of the software, which was developed at the GGL, ETH-Zurich, for processing kinematic GPS and airborne gravimetric data.

Parts which are not relevant for the processing of airborne gravimetry have been omitted.

14.2 GPS

The whole package consist of ten programs containing together around 7700 lines of source code. All the programs are written in Turbo Pascal 7 and run on DOS and DOS compatible PCs.

Simplified flow-charts of the data preparation and calculation of coordinates are shown in Figure 14.1 and 14.2 respectively.

14.3 Gravimetry

The whole package consists of 15 main programs containing all together around 14700 lines of source code. All the programs are written in standard FORTRAN 77 language with on-line graphic facilities for some of them. The graphic routines are written in a CALCOMP like language, containing only the following five routines : PLOT, FACTOR, NEWPEN, SYMBOL and NUMBER.

None of the programs is machine dependent and they are therefore fully portable.

Simplified flow-charts of the software are shown in Figures 14.3 and 14.4.

GPS : Data Preparation

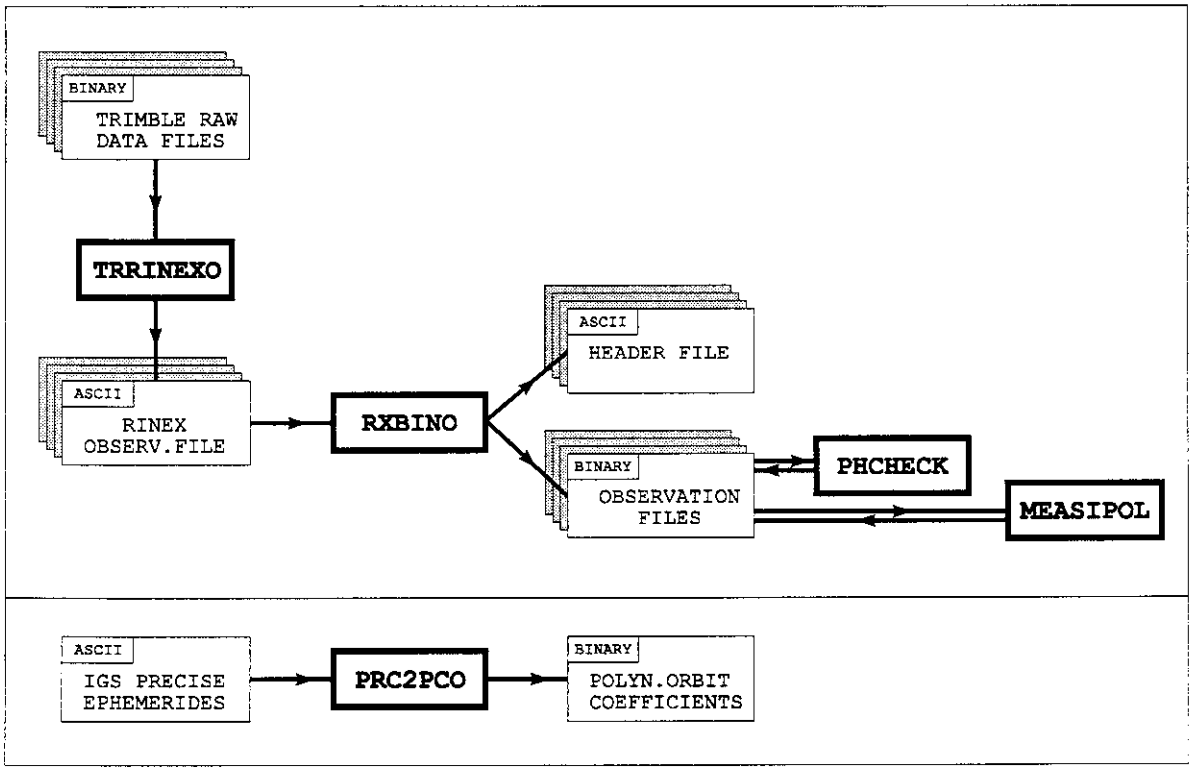

Figure 14.1: Flow-chart of the preparation part for processing kinematic GPS data.

TRRINEXO Conversion of binary raw data to RINEX (Receiver INdependent EXchange Format). Program from the Astronomical Institute of the University of Berne. Author : Dr. Werner Gurtner. (1 file per day and receiver).

RXBINO Conversion of the RINEX data to an ASCII header file and a binary observation file. (1 file per day and receiver).

PHCHECK Screening of raw phase measurements for cycle slips. Cycle slips are repaired and the observation files updated.

MEASIPOL Used for interpolation of raw measurements at the ground stations.

PRC2PCO IGS ephemerides are given as ITRF coordinates of all satellites with a time spacing of 15 minutes. The program converts the ITRF coordinates into a more convenient polynomial representation of the satellite orbit and satellite clock. (1 file per day).

GPS : Calculation of Coordinates

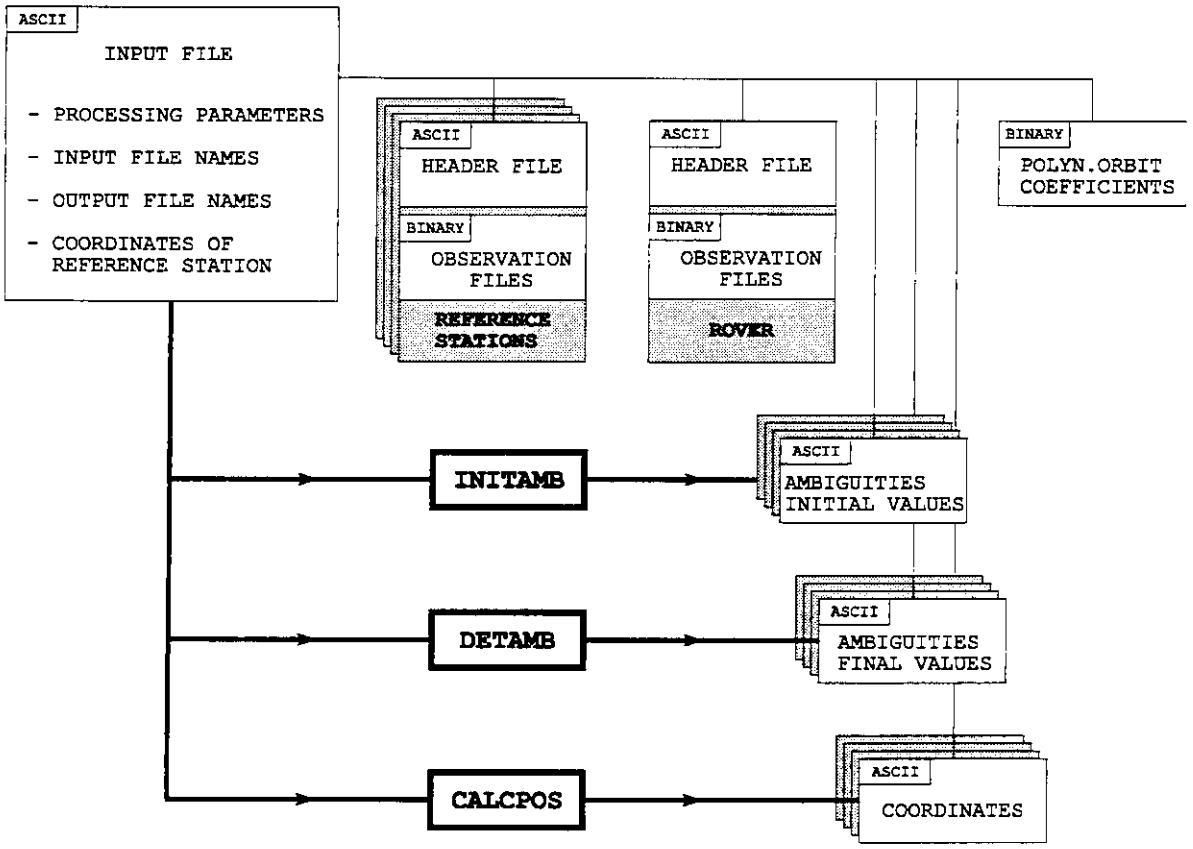

Figure 14.2: Float chart of coordinate calculation while processing kinematic GPS data.

INITAMB Initialization of the initial phase ambiguities, using single difference code measurements. The ambiguity output file is input file for DETAMB. (1 file per day, receiver pair and solution type / for example ZIMMERWALD - REAR L1).

DETAMB Determination of the ambiguities (floating point solution). The ambiguity output file is input file for CALCPOS. (1 file per day, receiver pair and solution type).

CALCPOS Calculation of the coordinates, stored in an ASCII file. (1 file per day, receiver pair and solution type).

All 3 programs use the same input file containing all necessary processing options and file names.

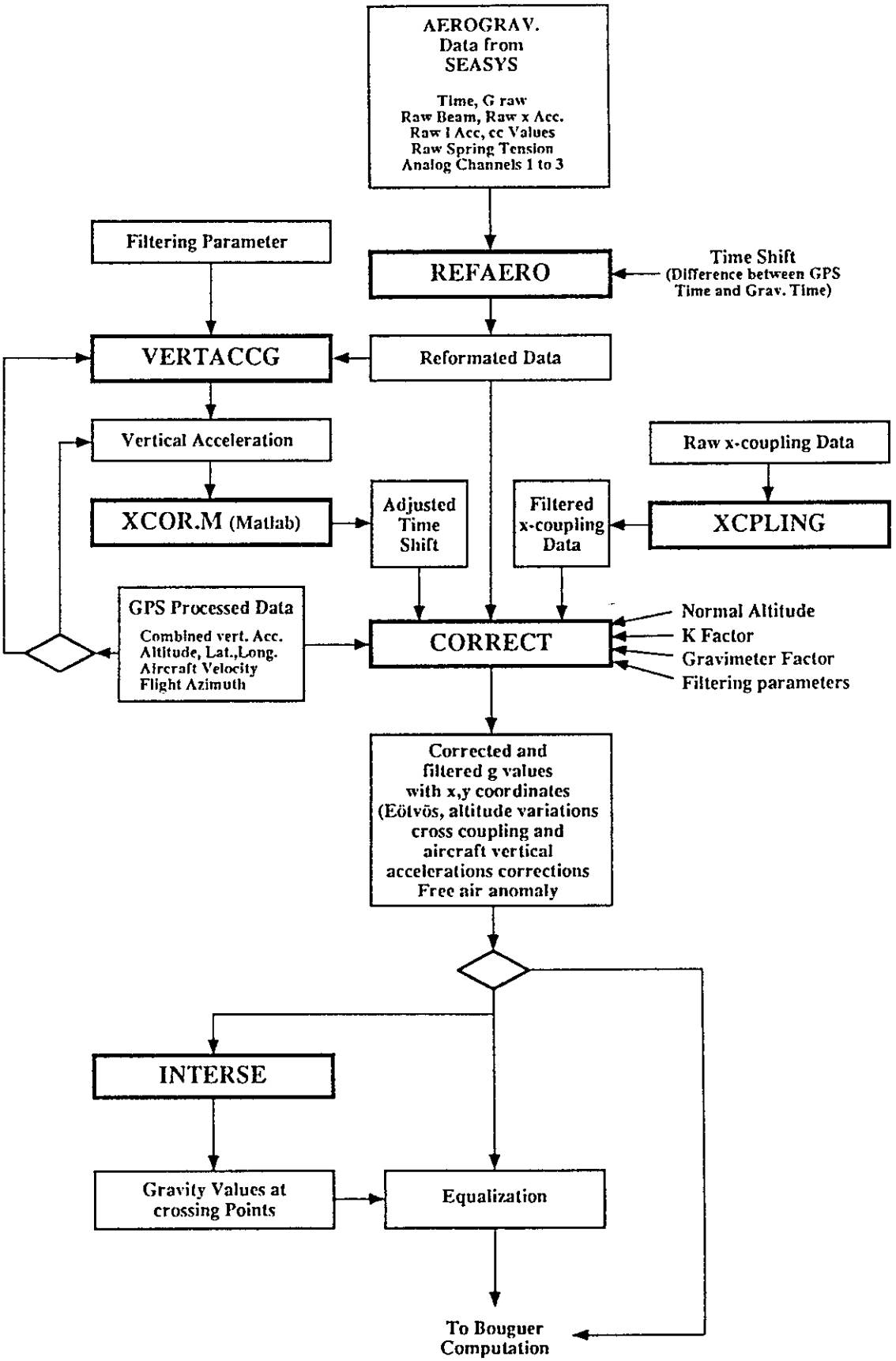

Figure 14.3: Flow-chart of gravimetric processing from raw gravimeter data to Free-Air anomalies.

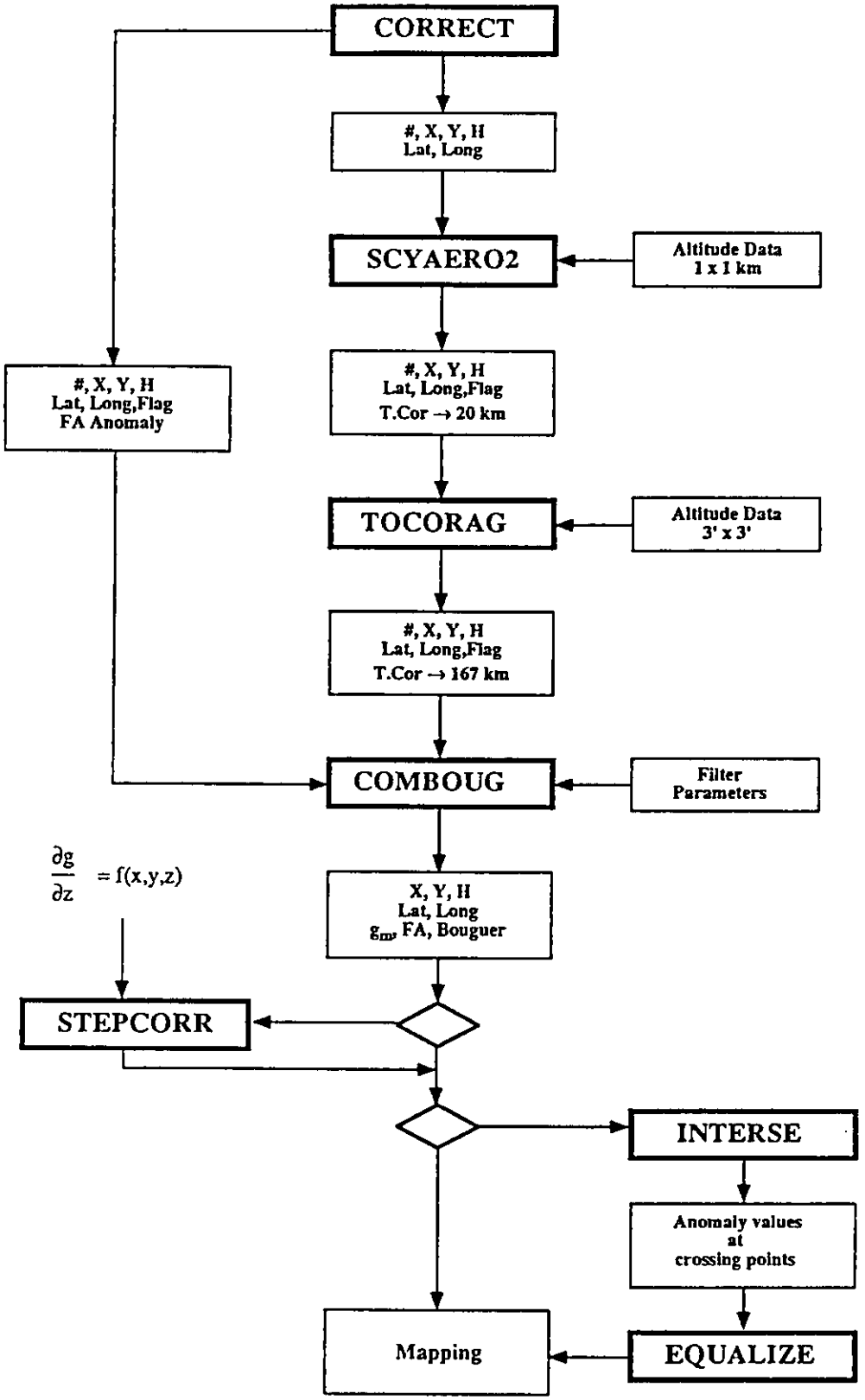

Figure 14.4 : Flow-chart of gravimetric processing from Free-Air anomalies to full Bouguer anomalies' mapping.

Programs of gravimetric processing

REFAERO Reformatization of gravimeter data and elimination of bad records.

VERTACC Computation of gravimeter vertical accelerations for determination of the filter's parameters (On-line graphic facilities).

AIRCRAFT Computation of vertical accelerations for each GPS antenna. Integration of attitude gyroscope data (On-line graphic facilities).

XCPLING Resampling and interpolation of cross-coupling data (On-line graphic facilities).

XCOR.M Cross-correlation of GPS and gravimeter data for determination of the residual time shift (MathLab language).

CORRECT Computation of *g* from raw beam and raw spring tension data.
Correction for residual time shift.
Corrections for EOTVOS accelerations and cross-coupling effects.
Computation of Free-Air anomaly.
(On-line graphic facilities).

INTERSE Search for crossing points and preparation for equalization (On-line graphic facilities).

SCYAERO Computation of the topographic correction form 0 to 20 km, based on digital topography of 1 by 1 km mesh.

TOCORAG Computation of the topographic correction from 20 to 167 km, based on digital topography of 3' by 3' mesh

COMBOUG Computation of full Bouguer anomaly (On-line graphic facilities).

STEPCOR Corrections for altitude differences, based on local vertical gradient. First order shift removal.

EQUALIZE Equalization.

GRIDPREP Preparation for gridding with removal of data with too strong horizontal gradients.

GRIDAEG Coarse interpolation.

FINGRID Fine gridding with file preparation for mapping.

ISOVAG Mapping.

APPENDIX A

Computation of the true vertical position of the gravimeter sensor

For the computation of the vertical movements of the aircraft, it was assumed that the pitch rotation always occurred around the axes of the wings, and the roll around the longitudinal axes of the aircraft.

The positions of the platform and of the two antennae are depicted in Figure A.1.

If we consider a right-handed Cartesian coordinate system with its origin at the crossing point of the wings and the longitudinal axes of the aircraft, we can compute the true altitude of the gravimeter, by combining the altitude of the front antenna and the values of the pitch and roll angles (α_p , α_r). The information of the rear antenna was used to check the value of the pitch angle.

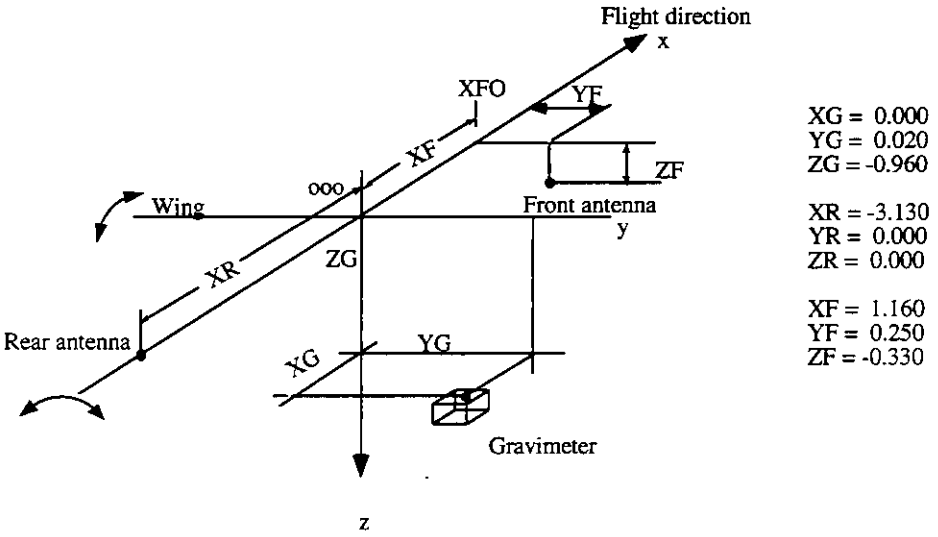

Figure A.1: Coordinates system used for the computation of the true altitude of the gravimeter. The origin of the system is at the crossing point of the wings and roof axes.

It is first necessary to compute the effect of the eccentricity of the front antenna when the aircraft exhibits pure roll movement. For this it is necessary to compute the altitude of the point XFO by means of the following geometrical relationship (Figure A.2):

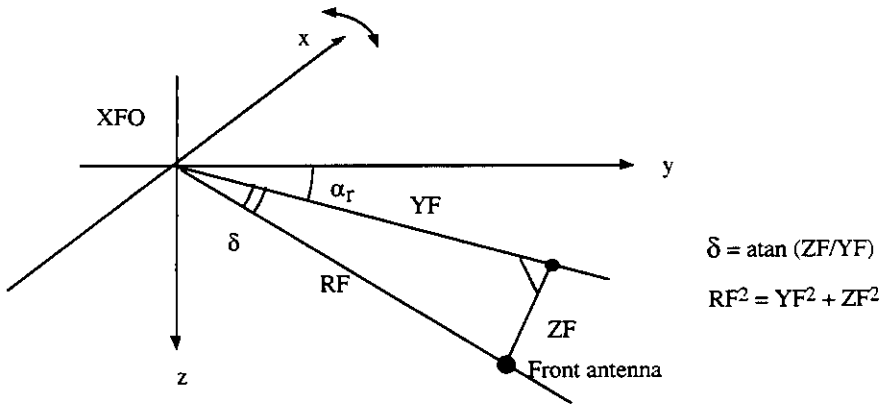

$$H(XFO) = HF + RF \cdot \sin(\delta + \alpha_r)$$

Figure A.2: Geometrical relationship between the position of the front antenna and the point XFO.

Second, the true altitude of the point ooo has to be calculated for pure pitch movement, by using the geometry depicted in Figure A.3. The pitch angle α_p is given by the attitude gyroscope.

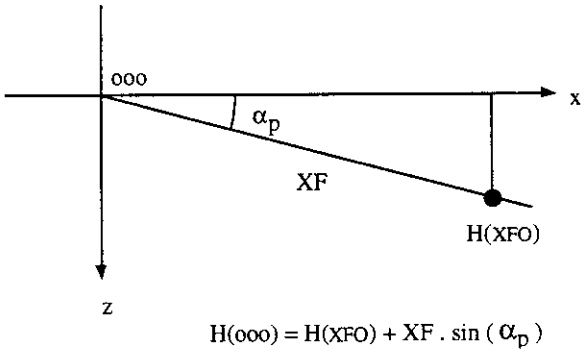

Figure A.3: Geometry used for computing the true altitude of point (ooo) during pure pitch movements.

The value of the pitch angle α_p given by the attitude gyroscope can be checked by using the altitude of the rear antenna as follow (Figure A.4) :

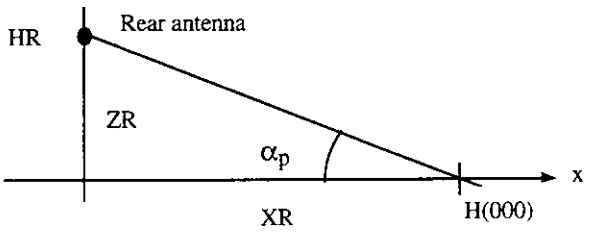

Figure A.4: Relationship between the pitch angle a_p and the position of the rear antenna.

Finally it is possible to compute the effect of roll and pitch on the gravimeter itself by means of the geometrical relationships depicted in Figures A.5 (Roll) and A.6a and A.6b (Pitch).

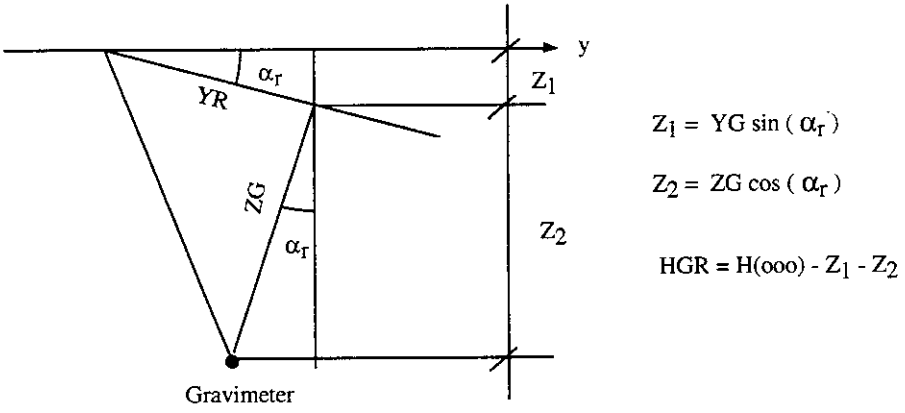

Figure A.5: Geometrical relationship between the position of the gravimeter, the rotations point (ooo) and the roll angle α_r.

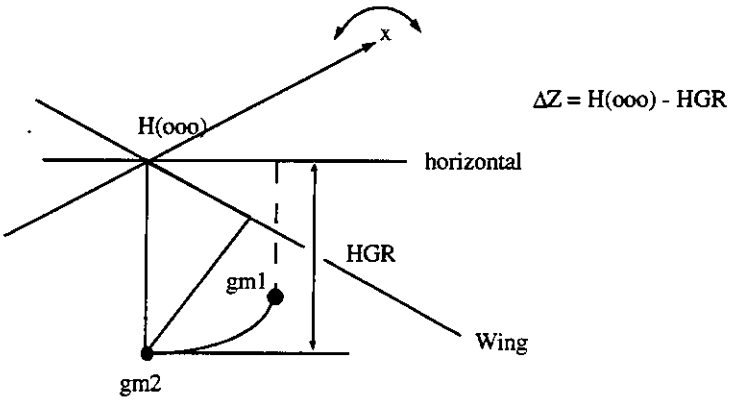

Figure A.6a: Sketch showing the position of the gravimeter with regard to the horizontal position of the wing when the aircraft exhibits a roll to the right. gm1 and gm2 are the positions of the gravimeter when the aircraft flies with and without roll.

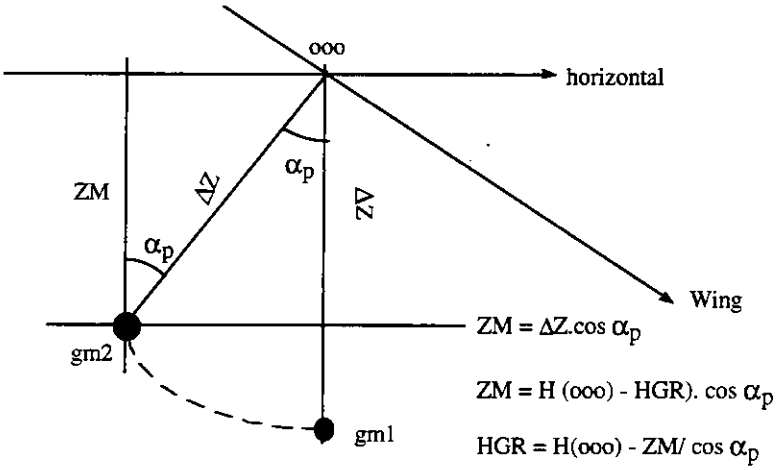

Figure A.6b: Sketch showing the position of the gravimeter with regard to the horizontal position of the aircraft when it exhibits a down pitch ($\alpha_p > 0$). gm1 is the position of the gravimeter when the aircraft is horizontal, gm2 is the position of the gravimeter when the aircraft has a pitch of α_p.

References

Bauersima I. (1983) : NAVSTAR/Global Positioning System (GPS) Band II: Radiointerferometrische Satellitenbeobachtungen. *Mitteilungen der Satelliten-Beobachtungsstation Zimmerwald Nr 10.*

Bell, R.E., Coackley, B.J., Stemp, R.W., 1991 : Airborne Gravimetry from a Small Twin Engine Aicraft over the Long Island Sound, *Geophysics, Vol. 6, Nr. 9, 1486-1493.*

Bell, R.E., Coackley, B.J., Blankenship, D.D., Hodge, S.M., Bozena, J.M. and J.J. Jarvis, 1992 : Airborne Gravity from a light Aircraft. *In Recent Progress in Antarctic Earth Sciences, p 571-577, Y. Yosidha, Editor. Tokyo.*

Beutler, G., I. Bauersima, W. Gurtner, M. Rothacher, M. Schildknecht, A. Geiger (1987) : Atmospheric refraction and other important biases in GPS carrier phase observations. *Paper presented at the 19th IUGG General Assembly, Vancouver 1987.*

Brozena, J.M., Peters, M.F., 1988 : An Airborne Gravity Study of eastern North Carolina, *Geophysics, Vol. 53, Nr. 2, 245-253.*

Brozena, J.M., 1984 : A Preliminary Analysis of the NRL Airborne Gravimetry System 1984, *Geophysics, Vol. 49, Nr. 7, 1060-1069.*

Brozena, J.M. and M. Peters, 1995 : State-of-the-art in airborne gravimetry. *Proceedings of the Joint Symposium of the International Gravity Commission and the International Geoid Commission, Graz, Austria, September 11-17, 1994.*

Cline, A.K., 1974 : Scalar and Planar Curve Fitting using Spline under Tension. *Comm. of ACM, 17, 4, 218-223.*

Cocard M. (1994) : High Precision Processing in Kinematic Mode. *Dissertation ETH No. 10874.*

Department of Defense Technical Report: World Geodetic System 1984. Its Definition and Relationships with Local Geodetic Systems, *DMA TR 8350.2, Headquarters, Defense Mapping Agency; Washington DC, September 1987.*

Forsberg, R. and S. Kenyon, 1994 : Evaluation and downward continuation of airborne gravity data - the Greenland example. *Proceedings of the International Symposium on Kinematic Systems in Geodesy and Navigation, Banff, Canada, August 30 - September 2, 1994.*

Geiger A. (1987) : Einfluss richtungsabhängiger Fehler bei Satellitenmessungen. *IGP-Bericht Nr 130, ETH-Zürich.*

Harlan, R.B., 1968 : "Eötvös Corrections for Airborne Gravimetry", *JGR, vol. 73 Nr. 14, pp. 4675-4679.*

Hehl, K., 1992 : Bestimmung von Beschleunigungen auf einem bewegten Träger durch GPS und Digitale Filterung, *Schriftenreihe des Studiengangs Vermessungswesen der Universitat der Bundeswehr Munchen,, ISSN 01731009, Neubiberg, Germany.*

Heiskanen, W.A., Moritz, H., 1987 : Physical Geodesy, *Institute of Physical Geodesy, Technical University Graz, Austria.*

Klingelé, E.E., Olivier, R., 1980 : La Nouvelle Carte Gravimetrique de la Suisse. Materiaux pour la Géologie de la Suisse, *Série Géophysique, 96 Pages, 9 Figures, 4 Tables, 1 Carte.*

Klingelé, E.E., Halliday, M., Bagnaschi, L., Cocard, m. and H-G, Kahle, 1993 : The Airborne gravimetric Survey of Switzerland. *Institute of Geodesy and Photogrammetry, IGP-Publication No. 226, ISBN 3-906513-59-9, ETH Zurich, Switzerland, June 1993.*

LaCoste, L.J.B.,1967 : Measurement of Gravity at Sea and in the Air, *Reviews of Geophysics, Vol. 5, No. 4, pp. 477-526.*

LaCoste, L.J.B., Ford, J., Bowless, R., and K. Archer, 1982 : Gravity Measurements in an Airplane Using State-of the-Art Navigation and Altimetry, *Geophysics, vol 47, Nr 5, 832-838.*

LaPorte, M., 1962 : Elaboration rapide des cartes gravimétriques déduites de l'anomalie de Bouguer à l'aide de la calculatrice électronique. *Geophys. Prosp., 10, 238-257.*

Mueller M.V. (1995) : Satellite Geodesy and Geodynamics : Current deformation along the West Hellenic Arc. *Dissertation ETH No. 11358.*

Rothacher M. G. Beutler, W. Gurtner, E. Brockmann, L. Mervart (1993) : Bernese Software Version 3.4, *Documentation published by the Astronomical Institute of the University of Berne.*

Saastamoinen J. (1973) : Contributions to the Theory of Atmospheric Refraction / Introduction to Practical Computation of Astronomical Refraction. *Bulletin géodésique Nrs 105, 106, 107, pp 50.*

Straub, C., H.-G. Kahle (1994) : GPS estimates of crustal deformation in the Marmara Sea Region, NW Anatolia. *In Earth and Planetary Science Letters, 121, pp 495-502.*

Valliant, H.D., 1991 : The LaCoste and Romberg Air/Sea Gravity Meter: An Overview, Geophysical Exploration at Sea, *2nd Edition, Vol. 1, pp. 141176, ISBN 0-8493-4252-X.*

Beiträge zur Geologie der Schweiz
Matériaux pour la Géologie de la Suisse
Contributions to the Geology of Switzerland
Contributi alla Geologia Svizzera

Geophysik - Géophysique - Geophysics - Geofisica

No.		Fr.
1	**H. Röthlisberger.** Zur seismischen und petrographischen Charakterisierung einiger Molassegesteine, einschliesslich der Beschreibung von Methoden der Korngrössenbestimmung in Festmaterial, 91 Seiten, 31 Figuren. 1957.	20.-
2	**O. Friedenreich.** Eine grossräumige Widerstandskartierung nordwestlich von Zürich und ihre geologische Deutung. 47 Seiten, 22 Textfiguren, 9 Karten. 1959.	24.-
3	**F. Gassmann.** Schweremessungen in der Umgebung von Zürich. 70 Seiten, 24 Textfiguren, 2 Tafeln. 1962.	30.-
4	**E. Poldini.** Les Anomalies gravifiques du canton de Genève. Avec 63 pages, 25 Figures et 3 planches. 1963.	30.-
5	**L. Rybach.** Refraktionsseismische Untersuchungen im Raum Aare-, Limmat- und Surbtal. 49 Seiten, 42 Figuren. 1962.	20.-
6	**O. Gonet.** Etude gravimétrique de la plaine du Rhône. Région Saint-Maurice - Lac Léman. 50 pages, 30 figures, 2 planches. 1965	20.-
7	**C. Meyer de Stadelhofen.** Carte des résistivités de la plaine du Rhône. 8 pages, 2 figures, 2 planches. 1966.	10.-
8	**O. Gonet.** Etude gravimétrique du lac Léman à bord du mésoscaphe *August Picard.* 50 pages, 8 figures, 1 planche. 1969.	10.-
9	**J. -J. Wagner.** Elaboration d'une carte d'anomalie de Bouguer. Etude de la vallée du Rhône de Saint-Maurice à Saxon (Suisse). 91 pages, 32 figures, 2 planches. 1970.	27.-
10	**H. Lazreg.** Etude géophysique, géologique et hydrogéologique de la région de Concise à Pompaples (pied du Jura vaudois). 51 pages, 16 figures, 2 planches. 1971.	27.-
11	**M. Petch.** Contribution à l'étude hydrogéologique de la plaine de l'Orbe. 95 pages, 23 figures, 15 planches. 1970.	27.-
12	**P.-A. Gilliand.** Etude géoélectrique du Klettgau (Suisse), canton de Schaffhouse. 85 pages, 47 figures, 10 annexes, 5 planches.1970.	27.-
13	**P. Corniche.** Application des méthodes géophysiques à la recherche hydrogéologique. 65 pages, 25 figures. 1973.	27.-
14	**F. Heller.** Magnetische und petrographische Eigenschaften der granitischen Gesteine des Albignagebietes (Nördliches Bergeller Massiv). 66 Seiten, 24 Textfiguren. 1972.	27.-
15	**E. Klingelé.** Contribution à l'étude gravimétrique de la Suisse romande et des régions avoisinantes. 94 pages, 6 figures, 35 planches. 1972.	27.-
16	**W. Sigrist.** Contribution à l'étude géophysique des fonds du lac Léman. 56 pages, 28 figures, 1 planche. 1974.	27.-
17	**R. Olivier.** Elaboration d'un système de traitement gravimétrique géré par l'ordinateur. Etude gravimétrique du plateau romand de Versoix (GE) à Concise (VD). 56 pages, 21 figures, 10 planches. 1974.	27.-
18	**H. Buchli, R. Paquin, A. Donzé.** Etude géoélectrique et gravimétrique du Chablais entre Asnières et Evian. 170 pages, 81 figures, 4 planches. 1976.	38.-
19	**G. Fischer, P.-A. Schnegg, J. Sesiano.** A new geomagnetic survey of Switzerland. 44 pages, 15 figures, 8 tables, 10 cartes. 1979.	34.-
20	**E. Klingelé, R. Olivier.** La nouvelle carte gravimétrique de la Suisse (Anomalies de Bouguer). 96 pages, 9 figures, 4 tables, 1 carte. 1980.	34.-
21	**J.-J. Wagner, St. Müller.** Geomagnetic and gravimetric studies of the Ivrea zone. 64 pages, 44 figures. 1984.	32.-
22	**Ph. Bodmer, L. Rybach.** Geothermal map of Switzerland (Heat flow density). 48 pages, 21 figures, 6 tables. 1984.	42.-
23	**G. Schwarz.** Methodische Entwicklungen zur Aerogammaspektrometrie. 160 Seiten, 56 figuren. 1991.	42.-
24	**U. Schärli, L. Rybach.** Geothermische Detailkartierung der zentralen Nordschweiz (1:100'000). 59 Seiten, 13 Figuren, 2 Karten. 1991.	48.-
25	**G. Schwarz, E. Klingelé, L. Rybach.** Airborne radiometric mapping in Switzerland. 74 pages, 12 figures, 17 tables, 14 maps, 1992.	48.-
26	**K. Risnes, B. Dumont, R. Olivier & J.-J. Wagner.** Etude des anomalies magnétique et gravimétrique de la région du Chasseral. 42 pages, 14 figures et 3 tables. 1993.	26.-
27	**G. Fischer, P.-A. Schnegg.** Updating the geomagnetic survey of Switzerland. 8 pages, 5 figures, 3 tables, 6 maps. 1994.	30.-
28	**S. Sellami.** Propriétés de roches des Alpes suisses et leur utilisation à l' analyse de la réflectivité de la croûte alpine. 160 pages, 59 figures, 16 tables. 1994.	45.-
29	**E. Rüttener.** Earthquake hazard evaluation for Switzerland. 150 pages, 88 figures, 12 tables, 1995.	45.-
30	**F. Medici, L. Rybach** : Geothermal map of Switzerland 1995 (Heat flow density). 36 pages, 11 figures, 1 table, 1 carte	55.-

<$$ DRUCKEREI $$>
1996